An estimation of the concentration of atmospheric nitrous oxide containing complexes

A thesis

submitted in partial fulfilment

of the requirements for the degree

of

Master of Science in Chemistry

at

The University of Waikato

by

Steven Ray Salmon

THE UNIVERSITY OF
WAIKATO
Te Whare Wānanga o Waikato

University of Waikato

2015

Abstract

Nitrous oxide (N_2O) is one of the major greenhouse gases responsible for climate change. It also has impacts on the removal of ozone (O_3) from the atmosphere and is now the single most important ozone depleting substance. Atmospheric N_2O primarily comes from bacterial denitrification processes in soils, a process which is augmented by many agricultural practices. As a result of the large amount of agricultural land in New Zealand, emissions of N_2O are disproportionately high for our population.

Nitrous oxide is primarily removed from the atmosphere via a photodissociation process, involving photons between 180 - 230 nm. The process of photodisociation involves the bending of the linear structure of the N_2O molecule, which allows for photodisociation to proceed. The presence of other gas molecules, such as those that we are investigating in our complexes, peturbs the bending mode of N_2O, which is throught to alter the photodisociation rate.

In this work we investigate the weakly bound complexes of N_2O with the major atmospheric molecules, namely N_2, O_2, Ar and H_2O. We use explicitly correlated coupled cluster theory to determine interaction energy, vibrational frequencies and rotational constants of the four complexes. This data is then used in combination with the standard statistical mechanics equations to determine the equilibrium constant of formation for each complex as a function of altitude. Finally the abundance profile of each complex is determined using the atmospheric concentrations of the constituent monomers.

Acknowlegements

Many thanks must firstly be given to my supervisor at the University of Waikato, Dr Jo Lane. For the time you have made to help me obtain this project, and the patience you have had during the course of this work.

To the Marsden Foundation, for the initial funding of this project, and for allowing students the opportunity to conduct research.

To Pieter Le Roux, for providing support with the University's High Performance Computational Facility, Symphony, which was used for all the simulations in this thesis.

At the University of Waikato there are a lot of people to thank, who I have hopefully thanked throughout the years for all of the support they have given. In no particular order, thanks have to be given to Chris Lockley, Megan, Alicia, Cass, Marcus, Chloe, Chris Batterton, Dan, Bill, Merilyn, Wendy, Pat, Jenny, Michael, Michelle and Graham.

The last and likely largest thanks has to be for my family. To my parents who have supported my work these past years, and to Mike and Laura, and Nana ad Pop, for the words of encouragement and support. A big thank you has to also be given to my Aunt Karen and Uncle Wayne (and Brianna), for giving me a place to stay in between flats and when needed.

Table of Contents

List of Figures

List of Tables

Appendicies

List of Abbreviations

au	Atomic units
BSSE	Basis set superposition error
CABS	Complementary auxiliary basis set
CBS	Complete basis set
CCSD	Coupled cluster singles doubles
CCSD(T)	Coupled cluster singles doubles and perturbative triples
CFC	Chlorofluorocarbon
CP	Counterpoise
GWP	Global warming potential
HF	Hartree Fock
IR	Infrared
MP2	Second order Moller Plesset function
ODP	Ozone depleting potential
UV	Ultraviolet
VPT2	Second order vibrational perturbation

1 – Introduction

1.1 - Atmospheric nitrous oxide

The concentration of nitrous oxide (N_2O) in Earth's atmosphere has been steadily increasing since the beginning of the industrial revolution, (Figure 1.1). Presently, the concentration of N_2O is 20% higher than pre-industrial conditions and is increasing at a rate of 0.2-0.3% per year.[1–3] Preindustrial sinks and sources of N_2O are believed to have had an equilibrium due to a relatively constant concentration between 150 and 3000 years ago.[1,4]

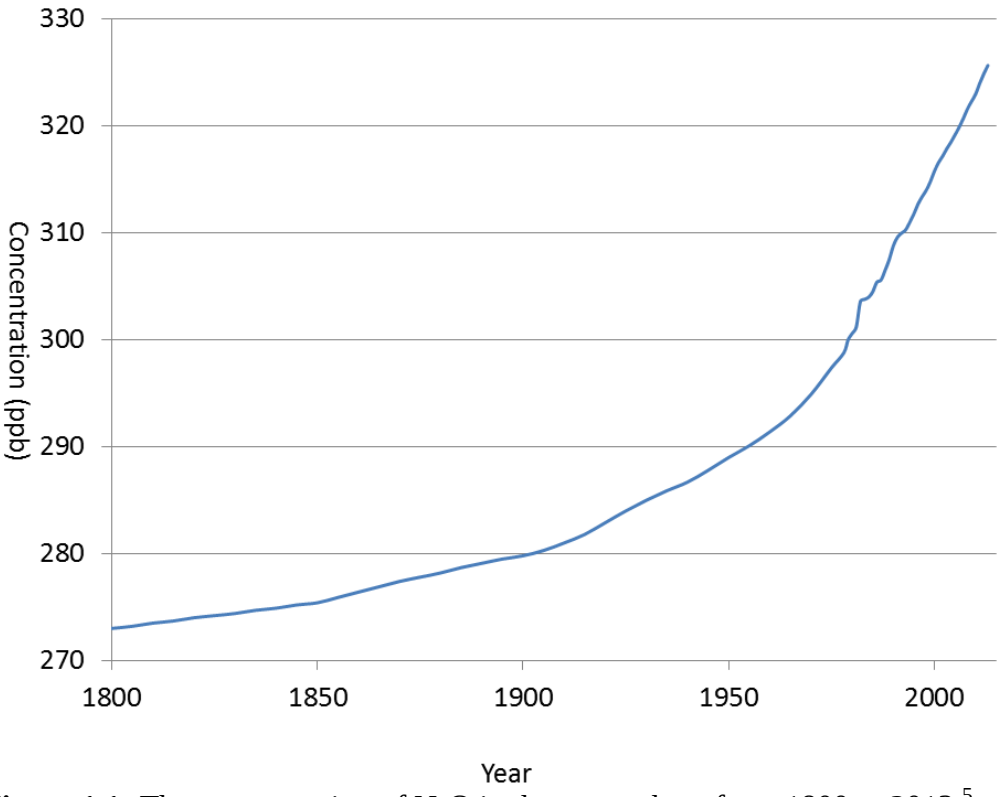

Figure 1.1: The concentration of N_2O in the atmosphere from 1800 to 2013.[5]

As shown in Figure 1.2, soil sources account for approximately 6.6 Tg of N_2O emissions annually. The majority of this emission comes from tropical soils. On top of this, oceans account for a further 3.8 Tg.[6] These two natural sources account for 70%[6,7] of N_2O emissions, with the other 30% coming from

anthropogenic activities, which equates to almost 6.7 Tg.[6,7] The largest human related source is from agricultural practices and activities, particularly the use of both synthetic and organic fertilizers, production of nitrogen fixing crops and the application of manure to croplands and pastures.[7] This leads to an increase in the level of nitrogen in soils and waterways, causing N_2O emissions of approximately 4.5 Tg per year, and thereby representing the majority of anthropogenic sources.[6] Fossil fuel combustion is also known to lead to N_2O emissions, but to a much lesser extent and is dependent on many factors such as the fuel type and technology, including catalytic converters which can produce N_2O.[7]

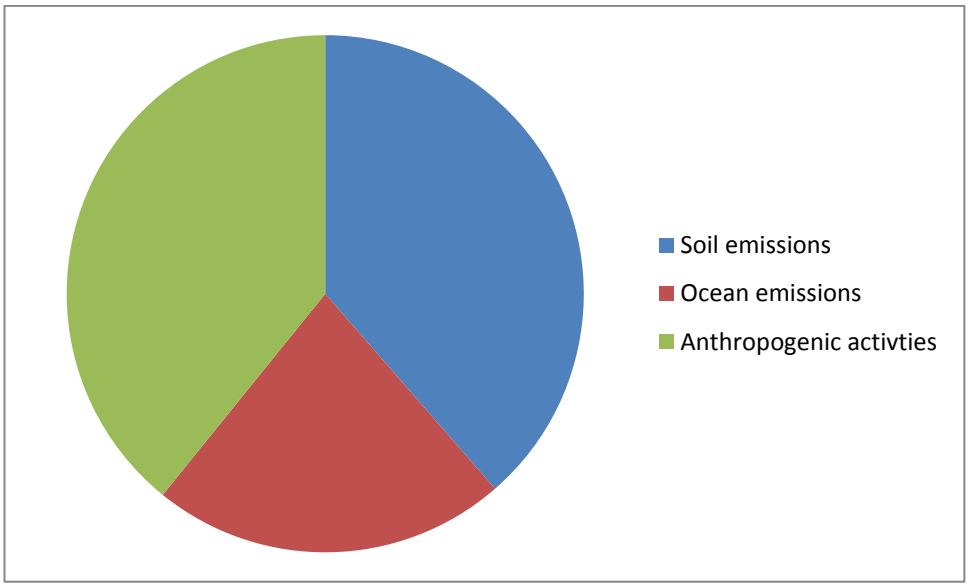

Figure 1.2: Atmospheric emissions of N_2O from all sources

Nitrous oxide is relatively inert in the lower atmosphere and as a consequence there is no significant concentration gradient between the hemispheres.[8] This is despite the fact that the Northern Hemisphere has a greater land area than the Southern Hemisphere.

Nitrogen exists as nitrate, NO_3^-, in aerobic conditions and as ammonium, NH_4^+, or ammonia, NH_3, in anaerobic conditions. The major sources of N_2O to the atmosphere involve denitrification, a reduction process, or nitrification, an oxidation process, in soils and aquatic systems. Of these two processes denitrification dominates.[9–16]

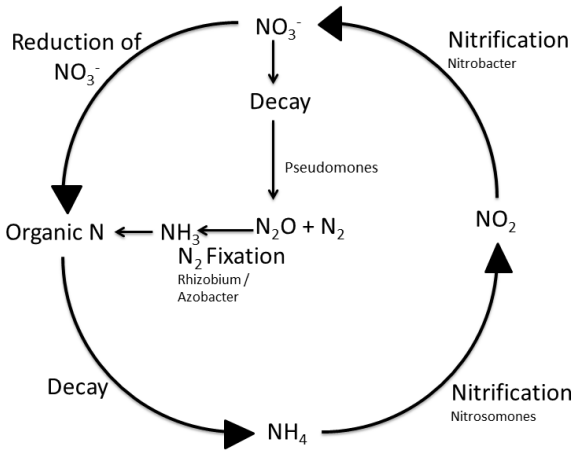

Figure 1.3: The nitrogen cycle[17]

Figure 1.3 shows the cycling of nitrogen in the biosphere. It indicates that organic nitrogen sources are decayed to ultimately yield N_2O, and shows that different species of bacteria utilise different nitrogen species in this cycle. The emissions of N_2O from soils are strongly influenced by land use and management. The emissions of N_2O have been determined to be highest in dairy grazed pastures (10-12 kg N_2O-N ha^{-1} $year^{-1}$), intermediate in sheep grazed pastures (4-6 kg N_2O-N ha^{-1} $year^{-1}$) and lowest in forest and ungrazed pasture soils (1-2 kg N_2O-N ha^{-1} $year^{-1}$).[18] N_2O emissions in New Zealand have increased by a total of approximately 25% between 1990 and 2004,[18] mainly due to increased fertiliser use and the associated excreted nitrogen input from intensified agriculture. Fertilisation of soils is known to increase N_2O emissions where the water content at the time of fertilisation seems to have the greatest effect on determining the emission level.[16] Large temporary N_2O emissions occur after each grazing and rainfall event, followed by a decline. Emissions are more variable during winter and spring due to wetter soils than in autumn. Denitrification is the primary source of New Zealand N_2O emissions.[18,19]

Soil type and drainage control the levels of organic matter and nitrogen mineralisation,[20,21] which is important for the control of nitrification.[20] Nitrous oxide emissions are observed to be approximately 20% higher in poorly drained silty soils as compared to well drained fine sandy soils. Normal agricultural practices are to drain and aerate soils, particularly when applying fertilizers.[22] There are several options to reduce N_2O emissions, aimed at increasing the

efficiency of nitrogen containing fertilisers, and reducing the amount of nitrogen cycling through the agricultural system. The main consideration is to match the mineral nitrogen supply, from all sources including fertilizers, manure and legume nitrogen fixation, to the needs of the pasture plants. Lower nitrogen content on pastures reduces the nitrogen excretion by animals and therefore reduces the gaseous emissions. Nitrification inhibitors have been proposed to reduce NO_3^- leaching and denitrification, including EcoN and N-core, which are used to reduce the leaching process. These inhibitors are thought to slow the oxidation of nitrogen to nitrate, retaining the ammonium form of nitrogen. The nitrification inhibitors don't inhibit nitrification indefinitely, allowing cycling to continue.[18] Nitrification inhibitors have been shown to reduce N_2O emissions from grazed pastures, however the efficiency in farm management has yet to be tested.

The ocean is also a significant source of N_2O.[23] There is a slight super saturation of N_2O present in most oceanic waters and the concentration usually increases with depth.[20,24,25] Sediments near shores often contain very high N_2O levels, up to 50 times that of air saturated concentrations.[20,26,27] A negative relationship exists between O_2 and N_2O, with a positive relationship between NO_3^- and N_2O, which suggests that nitrification, rather than denitrification, is the primary N_2O source in the oceans.[20]

1.2 – Climate change

Nitrous oxide is an important greenhouse gas that strongly absorbs infrared radiation. The sun emits a broad range of radiation with wavelengths spanning from the ultra-violet to the near-infrared. Earth's atmosphere is largely transparent to solar radiation in the visible region and this passes through to the surface where it is absorbed. Once absorbed, the Earth re-emits some of this energy but at longer wavelength in the infrared region. Earth's atmosphere contains a variety of small molecules known as greenhouse gases that are able to absorb this infrared radiation, which effectively retards some heat from being re-radiated to space. The net effect of these processes is an increase in the temperature of the Earth, which is commonly called the "greenhouse effect".

In Table 1.1 some of the properties of the major greenhouse gases are presented. The amount of energy absorbed by a given molecule depends on its concentration and lifetime in the atmosphere as well as its global warming potential (GWP). The GWP accounts for how strongly a molecule absorbs infrared radiation and in what spectral regions. Molecules with large GWPs strongly absorb infrared radiation in the so-called atmospheric windows where other atmospheric molecules, particularly H_2O, do not absorb. The major greenhouse gases have a considerable lifetime in the atmosphere, which leads to global distribution that is reasonably homogeneous.

Table 1.1: Atmospheric lifetime, GWP and concentration of the major anthropogenic greenhouse gases.

Molecule	Lifetime / years	GWP	Concentration / ppb
CO_2	100	1	397000
CH_4	12.4	34	1874
N_2O	121	298	324
CCl_2F_2	100	10900	0.527
$CHClF_2$	12	1810	0.231

New Zealand is unique in having its greenhouse gas emissions dominated by non-CO_2 gases, CH_4 (37.4%) and N_2O (17.4%)[18], which is a result of the strong agricultural base of New Zealand's economy and a low level of vehicular CO_2 emissions per unit of land, compared to other countries.

Radiative forcing is the term used to describe increased or decreased greenhouse trapping of radiation to provide a simplified measurement of the potential mechanism of climate change. It describes perturbation to the energy balance of the atmosphere. Values can be compared with the total amount of radiation that arrives to heat the earth, which has a value of approximately 235 W m^{-2}. In total it is estimated that due to changes in greenhouse gas concentrations alone, approximately 3.5 W m^{-2} less power is radiated back into space now compared to before the industrial revolution.

An increased N_2O concentration leads to increased radiative forcing and ultimately an increased temperature at the earth's surface. [22] Atmospheric N_2O is

expected to reach a concentration of approximately 484 ppbv by 2100 under current trend scenarios, which is 57% higher than the current 308 ppbv level, and 70% above that of the preindustrial 285 ppbv level.[1]

There is some uncertainty as to whether the feedback effect of an increased global temperature causes N_2O emissions to increase or decrease. A higher temperature is expected to stimulate microbial action in wetlands, and produce partial melting of permafrost, causing the release of N_2O.[28] However, a higher temperature may have a negative effect by reducing the wetland size via the increased evaporation[28,29]. Potter *et al.* suggest that N_2O emissions will be reduced significantly by a warmer climate, primarily due to the drying of soil due to the increased evaporation.[28,30] Analysis of air pockets in ice cores from 1450-1850 AD[3,4,28] showed both N_2O and CH_4 fell in concentration in this period known as the little ice age but returned to normal once the climate warmed back up. Some environments produce their greatest amount of emissions during freeze-thaw cycling, which may become more frequent under a warmer global temperature.[28]

1.3 – Photodissociation of N_2O

Nitrous oxide is chemically inert and is only removed from the atmosphere through photodissociation or by reacting with electronically excited oxygen atoms;[8,16,31–34]

$$N_2O + h\nu \rightarrow N_2 + O(^1D) \quad (1\text{-}1)$$

$$N_2O + O(^1D) \rightarrow N_2 + O_2 \quad (1\text{-}2)$$

$$N_2O + O(^1D) \rightarrow 2NO \quad (1\text{-}3)$$

Equation 1-1 accounts for 90% of the loss of N_2O in Earth's atmosphere, with equations 1-2 and 1-3 collectively making up the remaining 10%. The estimated atmospheric lifetime of N_2O is 120 years.[23]

Figure 1.4 shows how the concentration of atmospheric N_2O changes with altitude.[35] This shows that the concentration is largest at lower altitudes, which is sensible since the ground is the only source of N_2O. The stratospheric region of

the atmosphere represents the largest rate in reduction in the N_2O concentration, which is where the photodisociation rate is largest. The absolute rate of photodisociation decreases at the higher altitudes but only because most N_2O has already dissociated in the lower stratosphere.

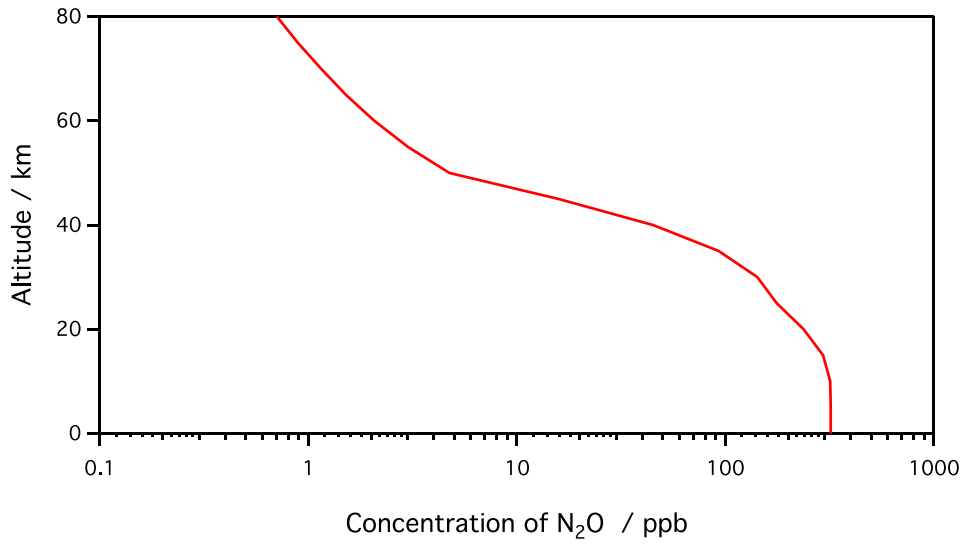

Figure 1.4: Concentration of N_2O as a function of altitude using data from US Standard Atmosphere.[35]

The rate of photodissociation depends on equation 1-4

$$J = \int \phi(\lambda)\sigma(\lambda)F(\lambda) \qquad (1\text{-}4)$$

where ϕ is the quantum yield, σ is the cross-section of the molecule and F is the flux of photons. If any of these three terms is zero, then the rate of photodissociation will also be zero. The dissociation energy required for equation 1-1 is 3.635 eV, which corresponds to a photon with a wavelength shorter than 341 nm. [36] Nitrous oxide undergoes a direct photodissociation mechanism and hence the quantum yield is 1 for all photons shorter than 341 nm.

As shown in Figure 1.5, the lowest energy electronic transition in N_2O has a maximum at 182 nm. The red tail of this absorption band extends to approximately 240 nm with a negligible cross-section at longer wavelengths. The absorption band centred at 182 nm corresponds to an electronic transition between the $X'\Sigma^+$ and $2'A'$ ($'\Delta$) states, which is dipole forbidden for the linear N_2O. The absorption band centred at 145 nm is much stronger as this corresponds to an allowed electronic transition.

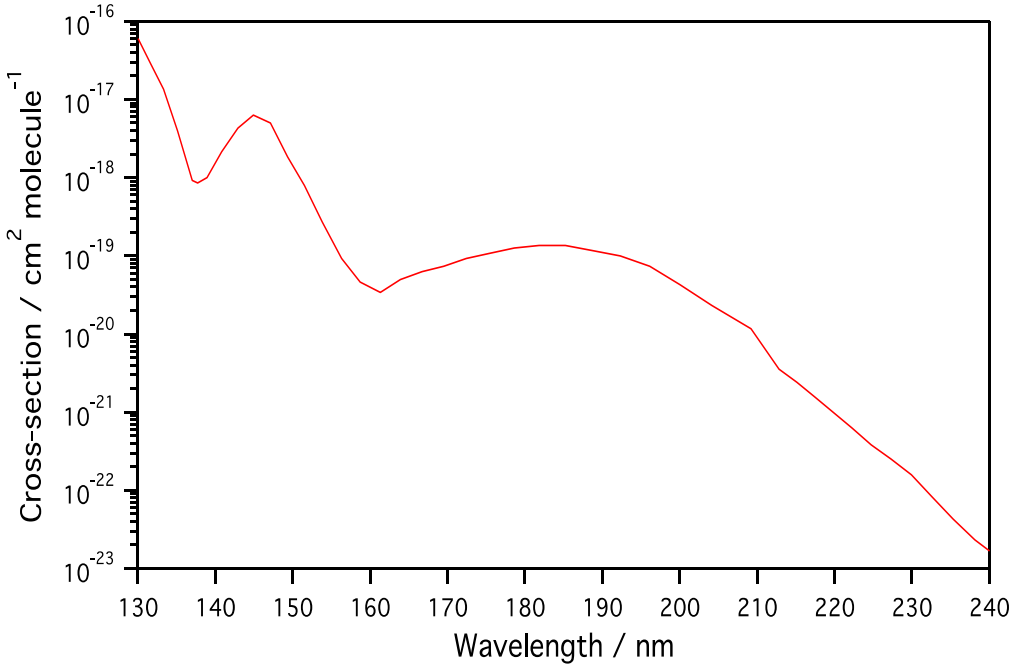

Figure 1.5: Cross-section of N_2O from 130-240 nm.[37]

N_2O photodisociation at 203-205nm has been investigated by Hanisco and Kumel[38] using state resolved resonance enhanced multiphoton ionization. This gave consistent data for one-photon dissociation using the bent 2'A' excited state. The N_2 fragment is rotationally excited as a result of the excited state geometry. Temperature dependence studies suggests increased absorbance with increased temperature is due to an increased proportion of the bending vibration.[38–44] The intensity of photodisociation from the (0,1,0) level has been determined to be 3.7 times that of the photodisociation from the (0,0,0) state.[45–47] This initial excitation is associated with a bending of the N_2O structure away from linear, breaking the symmetry constraint.

In Earth's atmosphere, the flux of solar photons below 300 nm is strongly dependent on altitude, which is shown in Figure 1.6. This is primarily due to absorption by O_3, which peaks in the stratosphere between 30-50 km. Ozone has an unusually strong absorbance in the critical 230-300nm range so it acts as an effective filter even when it is only present in a relatively low concentration as is observed in the atmosphere.[22] This means that there is a reduced amount of photons below 300 nm at the lower altitudes because of the increased amount of total ozone that it passes through. Filtering of this photon range is important for the protection of life from harmful radiation.

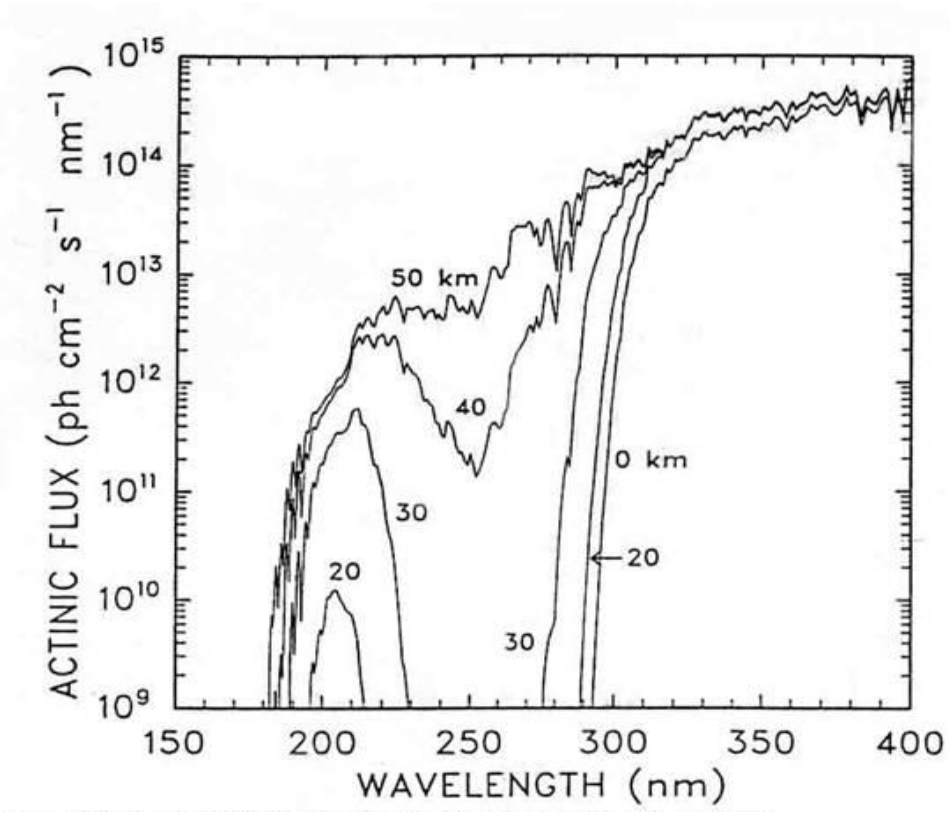

Figure 1.6: Spectral actinic flux for different altitudes as a function of wavelength.[48]

In Figure 1.7 we show the solar flux and the cross sectional area of N_2O at an altitude of 30 km, showing that N_2O photodissociation only occurs in the stratospheric UV window between 180 and 230 nm.[39] The small overlap between the available photons of the solar flux and the cross-sectional area of the N_2O in these wavelength range indicates, in part, why the rate of photodisociation of N_2O is small. Figure 1.7 shows that, in the high wavelength region where there is a large solar flux, the cross-section of N_2O is zero, whereas where there is a large N_2O cross-section in the small wavelength region, there is no solar flux in this region.

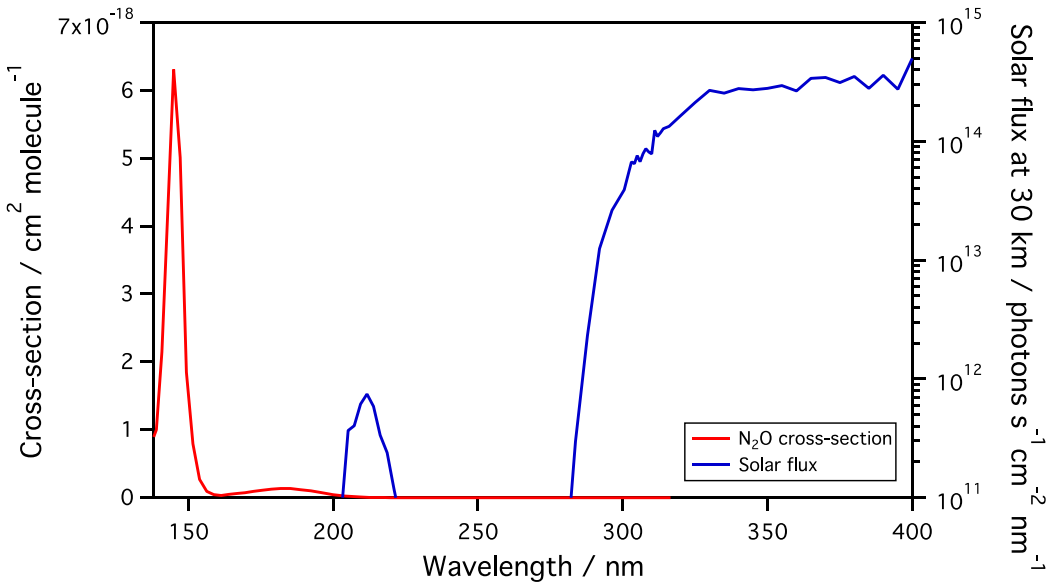

Figure 1.7: Cross-section of N_2O and solar flux at 30 km altitude

1.4 – Ozone depletion

The ozone layer protects life by screening out most of the damaging, high energy, UV radiation from sunlight. Ozone is formed naturally when UV radiation splits O_2 into two oxygen atoms which then combine with other O_2 molecules to form O_3.[49] The work by Chapman gave the first description of the formation and destruction of O_3 and allowed forthe first explanation for the temperature inversion in the stratosphere.[50] Chapman also determined that in addition to the formation reactions, there is a second pair that destroys O_3, in which O_3 absorbs UV and is photodisociated to release an O atom, which then combines with another O_3 molecule to form two molecules of diatomic oxygen, O_2.[50] These reactions are shown below in equations 1-5 to 1-8:

$$O_2 + UV\ (< 242\ nm) \rightarrow O + O \qquad (1\text{-}5)$$

$$O + O_2 + M \rightarrow O_3 + M \qquad (1\text{-}6)$$

$$O_3 + UV \rightarrow O_2 + O \qquad (1\text{-}7)$$

$$O_3 + O \rightarrow 2O_2 \qquad (1\text{-}8)$$

where M denotes a third molecule that must be present to carry off energy released from the process, which allows for stabilization of the ozone molecule.[50,51] The largest O_3 quantity would be expected to be found at low altitudes because the higher pressure will allow the three molecules in equation 1-6 to more readily interact.

Concerns about the stratospheric O_3 layer are largely focused on the reactions of O_3 with Cl and Br, released from the dissociation of CFCs and other halocarbons released from anthropogenic sources.[7] However, recently, Ravishankara *et al* point out that nitrogen oxides including N_2O, destroy more O_3 in the stratosphere than any other reactive chemical family.[7 52] This means that future changes to the climate and distribution of stratospheric O_3 depend on the emissions and change in the concentration of N_2O in the atmosphere.

The O (^{1}D) from the photodisociation of N_2O in Equation 1-1 is one of the major molecules that are able to remove the O_3 in the atmosphere, primarily by reactions 1-2 and 1-3 described earlier.[22] Most of the NO_x in the stratosphere originates from tropospheric N_2O.

Estimates of ozone depletion are difficult because the greenhouse gases affect the distribution of ozone, as well as its actual concentration. Tropospheric N_2O acts as the primary source of NO_x in the stratosphere although NO_x is a catalyst and contributes to the loss of ozone, it also sequesters ClO_x to form $ClONO_2$ reservoir species. The atmospheric N_2O lifetime means that any deleterious effects due to increased N_2O release will occur decades after the initial perturbation first occurs.[22]

The relative contributions of species for ozone depletion are typically quantified by an ozone depletion potential (ODP) value.[7,52] The ODP value relates to the amount of stratospheric ozone destroyed through the release of a unit mass of the chemical from the earth's surface to the amount destroyed by the release of a unit mass of the so called chlorofluorocarbon 11, $CFCl_3$. The ODP of N_2O under current atmospheric conditions is computed to be 0.017, but the large amounts of anthropogenic emissions of N_2O make this value significant. [52] Figure 1.8 shows the weighted ODP values for N_2O and a range of other ozone depleting gases, in particular cluorofluorocarbons (CFCs).[53]

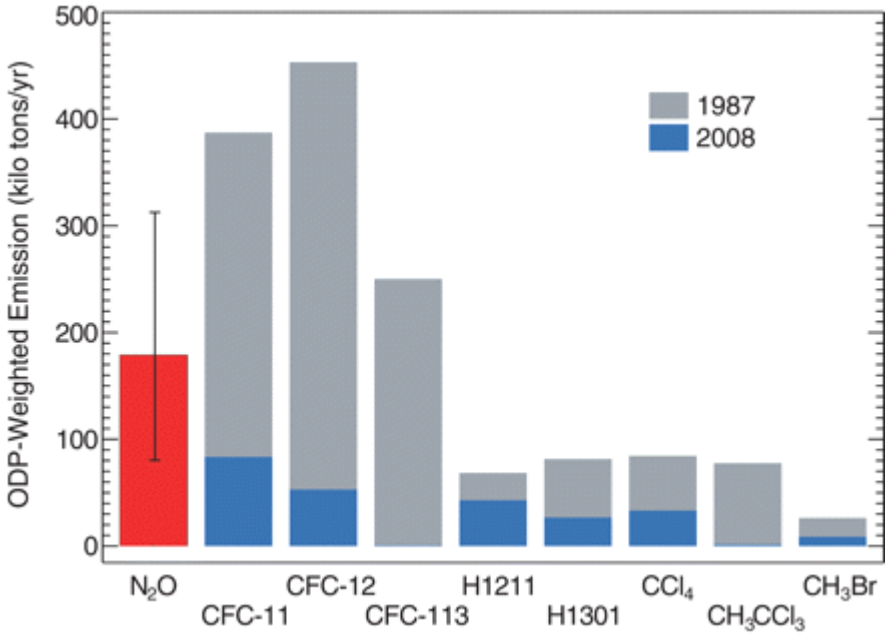

Figure 1.8: ODP-weighted atmospheric emissions[52]

1.5 - Atmospheric complexes

Theoretical and experimental studies have attempted to investigate the role of atmospheric molecular complexes. Some of the known effects of complexation include the shifting and broadening of monomer spectral features, appearance of new absorbance bands, intensity enhancement of forbidden electronic transitions, modification of existing monomer dissociation pathways and the appearance of entirely new photodisociation channels.[54]

Several homo and hetero dimer complexes are known to be important to Earth's atmosphere including the water dimer H_2O-H_2O, the dimeric form of nitrogen, N_2-N_2, the N_2-O_2 dimer and the dimer of ozone O_3-O_3.[54] Due to the nature of these complexes forming in very low concentrations and being restricted to a small altitude range, the properties of species that are difficult to measure with current technology can be computed instead.[55,56]

1.6 – Scope of this thesis

The primary objective of this research is to estimate the abundance of nitrous oxide complexes in Earth's atmosphere. The atmospheric abundance of a weakly bound complex is strongly correlated with the atmospheric abundance of the constituent monomers. Correspondingly, complexes with the four main atmospheric gases, namely N_2, O_2, Ar and H_2O, will be considered.

There have been only limited previous theoretical and experimental investigations of the N_2-N_2O, O_2-N_2O, Ar-N_2O and H_2O-N_2O complexes. A literature review of the previous research for each complex will be presented separately throughout this thesis in the relevant sections.

The lowest energy structures of the N_2-N_2O, O_2-N_2O, Ar-N_2O and H_2O-N_2O complexes will be calculated using high level computational chemistry methods. The equilibrium constant for formation of each complex will then be calculated with standard statistical mechanics equations using input data from the computational chemistry results. Finally, these temperature and pressure dependent equilibrium constants will be used in combination with atmospheric data to estimate the absolute abundance of each complex as a function of altitude.

2 - Theoretical methods

We initially investigated the geometries and interaction energies of the H_2O-N_2O, Ar-N_2O, N_2-N_2O and O_2-N_2O complexes with a range of relatively low cost methods and smaller basis sets. Specifically, the B3LYP, MP2, WB97XD and M062X methods, and the 6-31G(d), 6-311++G(2d,2p) and aug-cc-pVTZ basis sets. We considered all possible structures, however only some of these optimized to unique structures, which were then investigated at higher levels of theory.

The coupled cluster singles doubles and perturbative triples [CCSD(T)] method is often considered as the 'gold standard' for modern electronic structure determination, and is widely used to accurately describe hydrogen bonding and other weakly weak intermolecular interactions. In this thesis, we have used both conventional CCSD(T) and explicitly correlated CCSD(T)-F12. We use the closed shell CCSD(T) method for the H_2O-N_2O, Ar-N_2O and N_2-N_2O complexes and the unrestricted coupled cluster singles doubles and perturbative triples [UCCSD(T)] method for the O_2-N_2O complex .

The CCSD(T)-F12 method includes terms at the CCSD level of theory that depend explicitly on the inter-electronic distance. The slow convergence of electron correlation energy with increasing basis set size is accelerated by the inclusion of a small number of terms to the wave function that depend on the interelectronic distance r_{12}[57]. The CCSD(T)-F12 method enables larger systems to be investigated close to the CCSD(T) complete basis set (CBS) limit.[58] Two variants of CCSD(T)-F12 are commonly used, CCSD(T)-F12a and CCSD(T)-F12b. We have primarily chosen to use the CCSD(T)-F12b variant because this demonstrates systematic convergence of the correlation energy with increasing basis set size and CBS correlation factors have been determined. [57]

In Table 2.1, we present the electronic energy of N_2O calculated with both conventional CCSD(T) and the aug-cc-pVxZ basis sets (where x=D,T,Q) and explicitly correlated CCSD(T)-F12b with the cc-pVxZ-F12 basis sets (where x=D,T,Q). It should be noted that cc-pVxZ-F12 basis sets have been optimized for use with explicitly correlated F12 methods, and are of similar size to the corresponding aug-cc-pVxZ basis set, but contain fewer diffuse basis functions.[57] The geminal Slater exponents were set 0.9, 1.0 and 1.1 for the cc-pVDZ-F12, cc-pVTZ-F12 and cc-pVQZ-F12 basis sets, respectively.[57]

The CBS energies in Table 2.1 were obtained using a Schwenke style extrapolation scheme, whereby the explicitly correlated CCSD-F12 component and conventional (T) component were extrapolated with separate correlation factors. [57] This is important as the CCSD(T)-F12b method only includes explicit electron-electron correlation at the CCSD level of theory, with the perturbative triples contribution calculated conventionally.[57] The general expression for the CBS extrapolation can be written as

$$E_{CBS}^{Corr} = (E_Y^{Corr} - E_X^{Corr})F_{XY}^{Corr} + E_X^{Corr} \quad (2\text{-}1)$$

with the smaller (X) and larger (Y) basis sets respectively designated and F_{XY}^{Corr} is the correlation factor. [57,59] This approach has previously been used for many investigations of weakly bound complexes including the water dimer and base pair binding in DNA.[60]

As expected, we find that the HF energies of the conventional CCSD(T) results of the N_2O monomer become larger as the basis set increases. The reference energies of the explicitly correlated CCSD(T)-F12b method are slightly larger than those of the conventional results, primarily due to the additional complementary auxillary basis set (CABS) term.

The conventional CCSD correlation energies are found to be appreciably smaller than the explicitly correlated CCSD-F12b correlation energies. This is particularly apparent for the smallest double-zeta basis sets. We find that the CCSD correlation energy obtained with the aug-cc-pVQZ basis set is approximately the same value as the CCSD-F12 correlation energy obtained with the much smaller cc-pVDZ-F12 basis set. This highlight the impressive basis set convergence that can be obtained with explicitly correlated methods.

The triples contributions of the conventional CCSD(T) and explicitly correlated CCSD(T)-F12b results are of similar magnitude. This is because the CCSD(T)-F12b method only includes explicit correlation at the CCSD level of theory.

Overall, we find that the total energy obtained with the explicitly correlated CCSD(T)-F12b method is much closer to the CBS limit than the total energy obtained with conventional CCSD(T). The CCSD(T)/aug-cc-pVQZ energy is approximately the same as the CCSD(T)-F12b/cc-pVDZ-F12 energy, despite the fact that the latter took a tenth of the amount of time.

Table 2.1: Contributions to the electronic energy (in au) of N_2O with a range of basis set and method combinations

	HF	CCSD	(T)	Time (seconds)
aug-cc-pVDZ	-183.7093	-0.5331	-0.0270	1.15
aug-cc-pVTZ	-183.7515	-0.6321	-0.0368	6.88
aug-cc-pVQZ	-183.7633	-0.6646	-0.0389	50.78
	HF + CABS	CCSD-F12b	(T)	Time (seconds)
cc-pVDZ-F12	-183.7547	-0.6664	-0.0319	4.57
cc-pVTZ-F12	-183.7641	-0.6808	-0.0373	17.53
cc-pVQZ-F12	-183.7660	-0.6850	-0.0390	87.95
CBS limit		-0.6866	-0.0404	

Basis set superposition error describes the lowering of the energy of the molecule when the electrons of each atom spread into the basis functions associated by the other atoms due to an incomplete basis set.[61] The scheme for estimating BSSE using a counterpoise method , and was first proposed by Boys and Bernardi.[62] The binding energy E_{bind} of a complex AB required to separate into the two isolated monomers A and B is usually calculated as

$$E_{bind} = E_{AB}^{AB} - E_A^A - E_B^B \quad (2\text{-}2)$$

Where E_i^j is the total energy of a system i calculated using the basis sets in a system j. Using this notation, the counterpoise corrected binding energy E_{bind}^{CPC} is expressed as

$$E_{bind}^{CPC} = E_{AB}^{AB} - E_A^{AB} - E_B^{AB} \quad (2\text{-}3)$$

This leads to the BSSE being defined as the difference between equations 2-2 and 2-3

$$BSSE = E_{bind}^{CPC} - E_{bind} = E_A^A = E_A^{AB} + E_B^B - E_B^{AB} \quad (2\text{-}4)^{61}$$

For the standard optimization scheme, BSSE causes an artificial attraction of the two monomeric units and therefore an underestimation of the intermolecular

distance.[57] However, the CP optimization scheme has a slight overestimation of BSSE[57,63], which underestimates the interaction leading to an underestimation of the intermolecular distance.[57] Inclusion of explicit electron-electron correlation with the CCSD(T)-F12b method has been shown to significantly reduce the effects of BSSE for weakly bound complexes because the underlying energies are less affected by basis set incompleteness.[57]

Unless stated, all the coupled cluster calculations assume a frozen core and were performed using MOLPRO 2010.[57,64]

Tight convergence criteria were used in all of the calculations to obtain numerically stable results to an appropriate number of significant figures. The majority of the optimization criteria for the MOLPRO calculations were set as; gradient=$1x10^{-6}$ au, stepsize=$1x10^{-6}$ au and energy=$1x10^{-8}$ au. All of the single point energies were converged to $1x10^{-9}$ au.[57]

Anharmonic frequencies and corrections were also calculated using second order vibrational perturbation theory (VPT2) using CFOUR. These calculations were run using conventional CCSD(T) theory and the aug-cc-pVDZ and aug-cc-pVTZ basis sets. The CFOUR threshold criteria were set to; SCF_CONV=$1x10^{-10}$ au, CC_CONV=$1x10^{-11}$ au, LINEQ_CONV=$1x10^{-11}$ au and GEO_CONV=$1x10^{-10}$ au.

All optimizations allowed full geometric relaxation, whereas the experimental structures of the complexes assumed fixed geometric parameters for the monomeric units.[57] The experimental structures were also determined from rotational constants obtained in the vibrational ground state whereas our calculated geometric parameters use equilibrium values. The intermolecular potential energy surfaces of weakly bound complexes are highly anharmonic so determining the intermolecular distance from the vibrational ground state rotational constants will result in a value that is significantly longer than if it were obtained using the equilibrium rotational constants.[57]

3 - H_2O-N_2O

3.1 - Introduction

Weakly bound complexes containing H_2O have generated substantial scientific interest as H_2O is a major player in the absorption of solar and terrestrial radiation. Because of this, complexes with H_2O have great potential in altering the chemistry and radiative balance of Earth's atmosphere. [54]

The structure of the H_2O-N_2O complex has been experimentally measured using microwave spectroscopy and rotationally resolved infrared (IR) spectroscopy. These structures are shown in Figure 3.1a and 3.1c.

In 1992, Zolandz *et al.* first determined the structure of H_2O-N_2O from rotational constants obtained by microwave spectroscopy. This study measured rotational constants for the H_2O-N_2O, D_2O-N_2O and HDO-N_2O isotopomers and found the structure to be planar, with an approximate T-shape for the heavy atoms. [6] In 2002, Gimmler *et al.* measured rotational constants for H_2O-N_2O and D_2O-N_2O using high-resolution infrared spectroscopy. They also found a planar, approximately T-shape structure but with a more distinct tilt of the H_2O group to form a stronger secondary OH---O hydrogen bond.

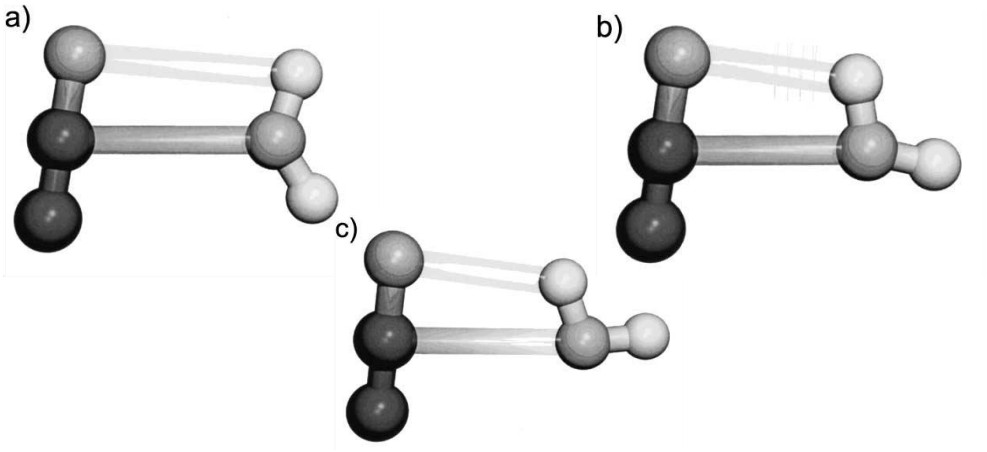

Figure 3.1: The structure of the H_2O-N_2O complex determined by microwave spectroscopy (a), previous theoretical calculations (b) and rotationally resolved infrared spectroscopy (c).[65]

In these experimental investigations, the authors assume that the monomer structures are unchanged when the complex is formed, which is a common assumption for the structural determination of complexes. Consequently, the complex was described by three parameters; R_{cms} to describe the distance between the centres of mass of the subunits, the angle of the N_2O molecular axis against the intermolecular axis, and the angle of the water C_{2v} axis against the intermolecular axis.

The structure of the H_2O-N_2O complex has also been previously theoretically investigated by Sadlej and Sicinski[65,66] using the Hartree-Fock method and 4-31G basis set. This calculated structure is shown in Figure 3.1b and exhibits the secondary OH---O hydrogen bond as found in the rotationally resolved infrared experiments but not in the earlier microwave experiments.[65,67]

In this chapter we present results for the optimised structure, vibrational modes and binding energy of H_2O-N_2O that we have conducted. Figure 3.2 shows the geometric parameters that were used to define the H_2O-N_2O structure. We conclude the chapter by presenting a "best estimate" structure and binding energy for H_2O-N_2O that takes into account the effects of core correlation, complete basis set limit extrapolations and counterpoise corrections.

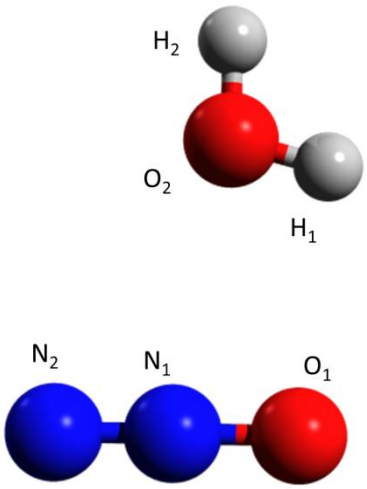

Figure 3.2: Geometric parameters used to define the structure of the H_2O-N_2O complex

3.2 - Structure of the H_2O-N_2O complex

In Tables 3.1 and 3.2 we present the CCSD(T)-F12a and CCSD(T)-F12b optimised geometric parameters of H_2O-N_2O, obtained using the cc-pVxZ-F12 basis sets, (x=D,T,Q), including and excluding a counterpoise correction. Table 3.2 also includes the optimised geometric parameters calculated at the CCSD(T)-F12b/CBS limit, obtained from the cc-pVTZ-F12/cc-pVQZ-F12 basis set pair. Overall we find excellent agreement between the CCSD(T)-F12a and CCSD(T)-F12b results, with the differences shown in Table A.1 in the appendix.

Consistent with previous studies of mixed water complexes[67], we find that geometric parameters optimised with the CCSD(T)-F12a and CCSD(T)-F12b methods rapidly converge with increasing basis set. Impressively, even the smallest cc-pVDZ-F12 basis set yields results in close agreement with the CBS limit.

There are relatively small differences between the standard and counterpoise corrected geometric parameters obtained with a given basis set. This indicates that basis set superposition error (BSSE) is relatively small in these calculations. The greatest differences between the standard and counterpoise corrected results are observed for the intermolecular bond distance and angles. As expected, we find that the magnitude of BSSE decreases as the basis set increases from cc-pVDZ-F12 to cc-pVTZ-F12, and finally to cc-pVQZ-F12. This is evident by the difference between the standard and counterpoise corrected runs reducing in magnitude as the basis set increases. Both of the CCSD(T)-F12a and CCSD(T)-F12b data sets show a reduction in the intermolecular bond length with the increasing zeta value.

The difference in the angles between the calculations with and without counterpoise correction shows that the slight increase in the $N_2N_1O_2$ bond angle is matched by a slight decrease in the $O_1N_1O_2$ bond angle of an approximately equal magnitude. Nonetheless these variations are relatively small given the inherently low potential energy surface of intermolecular angles.

Upon formation of the complex, the OH bond lengths of the H_2O unit become non-equivalent. The hydrogen atom closest to the N_2O unit increases by

approximately 0.0007Å whereas the other hydrogen atom, furthest from the N_2O unit, decreases by approximately 0.0003Å. This provides a difference between these two bond lengths of approximately 0.0010Å within the complex. The H_2O intramolecular bond angle increases by approximately 0.6° for the formation of the complex, in both of the CCSD(T)-F12a and CCSD(T)-F12b methods. The change in this parameter in particular indicates that the general approach of assuming the monomer geometric parameters remain unchanged upon complexation is not completely valid here. We see that for the N_2O bond lengths, the NO bond increases by approximately 0.002Å upon formation of the complex, whereas the NN bond decreases by approximately the same magnitude. This indicates that formation of the complex shifts the central nitrogen closer to the terminal nitrogen atom, and conversely further from the terminal oxygen atom.

Table 3.1: The CCSD(T)-F12a optimised structure of H_2O, N_2O and the H_2O-N_2O obtained with and without counterpoise correction

H_2O-N_2O	cc-pVDZ-F12			cc-pVTZ-F12			cc-pVQZ-F12		
	Standard	Counterpoise	Difference	Standard	Counterpoise	Difference	Standard	Counterpoise	Difference
$R_{(H1O2)}$	0.9596	0.9596	0.0000	0.9595	0.9595	0.0000	0.9591	0.9591	0.0000
$R_{(H2O2)}$	0.9588	0.9587	0.0000	0.9585	0.9585	0.0000	0.9582	0.9582	0.0000
$R_{(O1N1)}$	1.1903	1.1903	0.0000	1.1893	1.1893	-0.0001	1.1888	1.1887	-0.0001
$R_{(N1N2)}$	1.1270	1.1270	0.0000	1.1261	1.1261	0.0000	1.1255	1.1255	0.0000
$A_{(H1O2H2)}$	104.91	104.89	-0.02	104.99	104.98	-0.01	105.05	105.04	-0.01
$R_{(N1O2)}$	2.8514	2.8662	0.0148	2.8498	2.8544	0.0046	2.8494	2.8502	0.0007
$A_{(N2N1O2)}$	100.18	100.43	0.24	100.61	100.62	0.01	100.69	100.65	-0.04
$A_{(H2O2N1)}$	168.15	168.75	0.60	169.95	169.69	-0.26	170.04	169.84	-0.20
$A_{(O1N1O2)}$	80.18	79.96	-0.22	79.79	79.79	-0.01	79.73	79.77	0.03
H_2O									
$R_{(OH)}$	0.9589			0.9588			0.9587		
$A_{(HOH)}$	104.35			104.40			104.40		
N_2O									
$R_{(NO)}$	1.1882			1.1871			1.1865		
$R_{(NN)}$	1.1291			1.1282			1.1277		

Table 3.2: The CCSD(T)-F12b optimised structure of H_2O, N_2O and the H_2O-N_2O complex obtained with and without counterpoise correction, and at the CBS limit

	cc-pVDZ-F12			cc-pVTZ-F12			cc-pVQZ-F12			CBS limit
H_2O-N_2O	Standard	Counterpoise	Difference	Standard	Counterpoise	Difference	Standard	Counterpoise	Difference	
$R_{(H1O2)}$	0.9584	0.9584	0.0000	0.9584	0.9584	0.0000	0.9581	0.9581	0.0000	0.9581
$R_{(H2O2)}$	0.9593	0.9592	0.0000	0.9593	0.9593	0.0000	0.9591	0.9591	0.0000	0.9591
$R_{(N1O1)}$	1.1895	1.1895	0.0000	1.1890	1.1889	-0.0001	1.1887	1.1886	-0.0001	1.1885
$R_{(N1N2)}$	1.1266	1.1267	0.0000	1.1259	1.1260	0.0001	1.1255	1.1255	0.0000	1.1255
$A_{(H1O2H2)}$	104.89	104.87	-0.02	104.99	104.97	-0.02	105.04	105.03	-0.01	105.05
$R_{(N1O2)}$	2.8578	2.8734	0.0155	2.8518	2.8573	0.0055	2.8503	2.8519	0.0016	2.8487
$A_{(N2N1O2)}$	100.24	100.46	0.21	100.66	100.62	-0.04	100.73	100.65	-0.08	100.63
$A_{(H2O2N1)}$	167.94	168.46	0.53	169.98	169.48	-0.51	170.19	169.73	-0.46	169.75
$A_{(O1N1O2)}$	80.15	79.95	-0.20	79.76	79.8	0.04	79.69	79.77	0.08	79.79
H_2O										
$R_{(OH)}$	0.9586			0.9586			0.9583			0.9583
$A_{(HOH)}$	104.33			104.40			104.45			104.47
N_2O										
$R_{(NO)}$	1.1874			1.1868			1.1864			1.1863
$R_{(NN)}$	1.1287			1.1281			1.1277			1.1276

To assess the impact of freezing the core electrons, we have also optimised the geometries of H_2O, N_2O and the H_2O-N_2O complex with all electrons correlated. In Table 3.3 we present the CCSD(T)-F12b optimised geometric parameters of H_2O, N_2O and the H_2O-N_2O complex obtained with the cc-pVQZ-F12 basis set utilising the frozen core approximation and with the cc-pCVQZ-F12 basis set correlating all electrons. The difference between these two calculations is used as an estimate of the effect of core correlation.

We find that the inclusion of core correlation consistently reduces the bond lengths. It has an appreciable but non-systematic effect on the bond angles. In an absolute sense, core correlation has a greater effect on the intermolecular bond length than it does on the intramolecular bond lengths. However, because the intermolecular bond length is approximately three times larger, the relative change due to core correlation is similar.

We find that the inclusion of the core valence correlation reduces the intramolecular bond lengths and increases the intramolecular bond angles. This is the same effect that is observed in previous work on the H_2O-H_2O complex. [58]

Also shown in Table 3.3 is our best estimate of the geometric parameters of the H_2O-N_2O complex. This structure is obtained by adding the difference between the all electron cc-pCVQZ-F12 optimization and frozen core cc-pVQZ-F12 optimization to the CBS limit structure. We find that the "best estimate" geometry is in excellent agreement with the all electron CCSD(T)-F12b/cc-pCVQZ-F12 structure, highlighting again the impressive basis set convergence obtained with the explicitly correlated CCSD(T)-F12b method.

Table 3.3: All electron and frozen core counterpoise corrected optimised geometric parameters of H_2O, N_2O and the H_2O-N_2O complex obtained with the CCSD(T)-F12b method

	cc-pVQZ-F12	cc-pCVQZ-F12	Difference	CCSD(T)-F12b/CBS	Best estimate
H_2O-N_2O					
$R_{(H1O2)}$	0.9581	0.9572	-0.0009	0.9581	0.9572
$R_{(H2O2)}$	0.9591	0.9581	-0.0009	0.9591	0.9582
$R_{(O1N1)}$	1.1887	1.1864	-0.0022	1.1885	1.1863
$R_{(N1N2)}$	1.1255	1.1233	-0.0022	1.1255	1.1233
$A_{(H1O2H2)}$	105.04	105.16	+0.11	105.05	105.16
$R_{(N1O2)}$	2.8503	2.8482	-0.0021	2.8487	2.8466
$A_{(N2N1O2)}$	100.73	100.67	-0.06	100.63	100.57
$A_{(H2O2N1)}$	170.19	169.75	-0.44	169.75	169.31
$A_{(O1N1O2)}$	79.69	79.75	+0.06	79.79	79.85
H_2O					
$R_{(OH)}$	0.9583	0.9574	-0.0009	0.9583	0.9574
$A_{(HOH)}$	104.45	104.57	+0.12	104.47	104.59
N_2O					
$R_{(NO)}$	1.1864	1.1842	-0.0022	1.1863	1.1841
$R_{(NN)}$	1.1277	1.1254	-0.0022	1.1254	1.1232

Table 3.4 we present the optimized geometric parameters of H_2O-N_2O obtained with conventional CCSD(T) and the aug-cc-pVxZ basis sets, (x=D,T), and at the CCSD(T)-F12b/CBS limit. The CCSD(T) results were obtained with CFOUR utilizing analytical derivatives whereas the CCSD(T)-F12b/CBS result was obtained using MOLPRO with numerical derivatives. This comparison is necessary as only CFOUR has implemented the calculation of anharmonic vibrational frequencies using second order vibrational perturbation theory (VPT2) with the CCSD(T) method.

As expected, we find that the CCSD(T) optimized geometric parameters converge towards the CBS limit as the basis set increases from aug-cc-pVDZ to aug-cc-pVTZ. The calculated bond lengths become shorter as the basis set increases, however there is no systematic change in the calculated bond angles. For easy comparison, we also show in Table 3.4 the difference between the CCSD(T)/aug-cc-pVTZ and CCSD(T)-F12b/CBS optimized geometric parameters. Overall, we find that the CCSD(T)/aug-cc-pVTZ optimised geometric parameters are in reasonable agreement with the CCSD(T)-F12b/CBS limit. The CCSD(T)/aug-cc-pVTZ optimised bond lengths are 0.003-0.006 Å longer than the CCSD(T)-F12b/CBS limit. The corresponding bond angles have flatter potentials, hence there is more variation between these two methods with up to a 1.3° difference.

Table 3.4: The structure of H_2O, N_2O and the H_2O-N_2O complex optimised with conventional CCSD(T) and at the explicitly correlated CCSD(T)-F12b/CBS limit

	CCSD(T)/aug-cc-pVDZ	CCSD(T)/aug-cc-pVTZ	CCSD(T)-F12b/CBS	Difference[1]
H_2O-N_2O				
$R_{(H1O2)}$	0.9659	0.9613	0.9581	-0.0032
$R_{(H2O2)}$	0.967	0.9623	0.9591	-0.0032
$R_{(N1O1)}$	1.2047	1.1935	1.1885	-0.0050
$R_{(N1N2)}$	1.1467	1.1303	1.1255	-0.0049
$A_{(H1O2H2)}$	104.56	104.77	105.05	0.28
$R_{(N1O2)}$	2.8733	2.8547	2.8487	-0.0059
$A_{(N2N1O2)}$	101.32	100.63	100.63	-0.01
$A_{(H2O2N1)}$	176.09	171.06	169.75	-1.31
$A_{(O1N1O2)}$	79.17	79.79	79.79	0.01
H_2O				
$R_{(OH)}$	0.9665	0.9616	0.9583	-0.0033
$A_{(HOH)}$	103.94	104.18	104.47	0.29
N_2O				
$R_{(NO)}$	1.2018	1.1912	1.1863	-0.0049
$R_{(NN)}$	1.1491	1.1326	1.1276	-0.005

[1] Difference between CCSD(T)/aug-cc-pVTZ and CCSD(T)-F12b/CBS

3.3 - Vibrational modes of the H_2O-N_2O complex

In Table 3.5 we present harmonic vibrational frequencies of H_2O, N_2O and the H_2O-N_2O complex calculated with the CCSD(T)-F12a and CCSD(T)-F12b methods, and the cc-pVxZ-F12 basis sets. These results were obtained without counterpoise correction using the standard geometries from Tables 3.1 and 3.2. No vibrational intensities are presented as these cannot be calculated in MOLPRO due to the use of numerical energy derivatives

The vibrational modes of the H_2O-N_2O complex can be seen to vary only slightly between the CCSD(T)-F12a and CCSD(T)-F12b results. There is also little variation between the harmonic frequencies obtained with the different basis sets, indicating that the results are close to being converged to the CBS limit. The five lowest vibrational modes of H_2O-N_2O represent the intermolecular vibrational modes. These modes are calculated to be slightly smaller with the CCSD(T)-F12b method than the CCSD(T)-F12a method. Interestingly, the opposite trend is observed for the intramolecular vibrational modes with the CCSD(T)-F12b method generally calculating larger vibrational frequencies than the CCSD(T)-F12a method.

The lowest energy vibrational mode of N_2O monomer increases by approximately 10 cm^{-1} upon complexation. This mode is also doubly-degenerate in the monomer but separates by more than 1 cm^{-1} in the complex. It is noted that despite the very tight convergence used, the monomer vibrational frequencies of this mode are not calculated to be perfectly degenerate due to numerical errors.

The vibrational modes of the H_2O monomer change to a smaller amount upon complexation as compared to the N_2O monomer. All three vibrational modes in the H_2O monomer are reduced in wavenumber upon forming the complex by 2-7 cm^{-1}. In comparison, the vibrational modes of N_2O monomer change by 7-33 cm^{-1} upon complexation.

Table 3.5: Harmonic vibrational frequencies (cm^{-1}) of H_2O, N_2O and the H_2O-N_2O complex calculated with the CCSD(T)-F12a and CCSD-F12b methods and the cc-pVxZ-F12 (x=D,T,Q) basis set

	cc-pVDZ-F12		cc-pVTZ-F12		cc-pVQZ-F12	
	CCSD(T)-F12a	CCSD(T)-F12b	CCSD(T)-F12a	CCSD(T)-F12b	CCSD(T)-F12a	CCSD(T)-F12b
H_2O-N_2O						
ν_1	70.1	68.5	69.4	68.7	67.9	66.7
ν_2	95.4	94.8	85.0	84.6	70.4	77.5
ν_3	120.0	118.1	120.9	120.4	122.1	121.5
ν_4	157.5	155.7	156.5	155.9	157.3	157.0
ν_5	194.9	192.3	200.2	199.7	198.1	205.9
ν_6	592.1	593.3	596.2	596.3	597.4	597.6
ν_7	593.6	595.0	597.6	597.8	598.6	598.9
ν_8	1294.5	1297.6	1297.5	1298.8	1299.4	1299.4
ν_9	1643.7	1646.7	1642.1	1643.4	1641.6	1642.4
ν_{10}	2291.7	2292.7	2296.4	2296.8	2299.1	2298.7
ν_{11}	3829.2	3834.0	3828.0	3830.3	3831.8	3831.5
ν_{12}	3939.5	3943.6	3939.8	3941.7	3944.0	3943.7
H_2O						
ν_1	1649.9	1652.9	1649.1	1650.5	1649.6	1649.1
ν_2	3832.6	3836.9	3831.5	3833.6	3830.2	3835.0
ν_3	3941.3	3944.9	3941.8	3943.5	3940.6	3945.7
N_2O						
ν_1	581.7	583.	586.5	586.7	587.8	588.0
ν_2	581.8	583.3	586.6	586.7	587.8	588.0
ν_3	1300.4	1303.7	1304.6	1305.9	1306.2	1306.8
ν_4	2259.7	2260.3	2264.6	2265.1	2266.0	2266.3

In Table 3.6 we present harmonic and anharmonic vibrational frequencies and intensities for H_2O, N_2O and H_2O-N_2O calculated with conventional CCSD(T) and the aug-cc-pVxZ basis sets (x=D, T). These results were obtained without counterpoise correction using the geometries from Table 3.4. The anharmonic results were calculated within the second order vibrational perturbation theory (VPT2) framework.

The harmonic frequencies calculated with conventional CCSD(T) and the aug-cc-pVDZ or aug-cc-pVTZ basis set are in general slightly smaller than those calculated with explicitly correlated CCSD(T)-F12b and the cc-pVDZ-F12 or cc-pVTZ-F12 basis set. This difference is expected, as bond lengths contract and hence harmonic frequencies become larger as the basis set increases towards the CBS limit.

The harmonic intensities of the vibrational modes for both of the monomer species show a reasonable consistency between the aug-cc-pVDZ and aug-cc-pVTZ results, indicating that these are reasonably well converged with respect to the CBS limit.

As expected, in both of the monomers and for the complex, the anharmonic vibrational frequencies are calculated to be smaller than the respective harmonic mode. For the monomers, these calculated anharmonic frequencies are all sensible and are in reasonably good agreement with the experimental fundamental frequencies. The intramolecular vibrational frequencies also appear to be reasonable; however there is more extreme change in some of the intermolecular vibrational modes. It is likely that these unphysical anharmonic vibrational frequencies are a consequence of numerical instabilities in the VPT2 calculation, which require very accurate third and fourth order energy derivatives. The VPT2 implementation in CFOUR obtains these higher order derivatives by numerical differentiation of analytical second order energy derivatives. We have used the tightest energy convergence criteria that are practicable in CFOUR however this has not entirely solved the problem.

The monomer frequencies and intramolecular vibrational frequencies of the complex are seen to be in a good agreement between the aug-cc-pVDZ and aug-cc-pVTZ, with the anhamonic data being in a greater agreement for the N_2O unit than the harmonic data, whereas the harmonic data for the H_2O unit seems more consistent upon formation of the complex. With the exception of the harmonic ν_3 mode in the H_2O unit, and the ν_4 mode in N_2O, the magnitudes of the modes are smaller in the complex than the respective mode in the complex. In a similar manner, with the exception of the anhamonic ν_3 mode in the H_2O unit, and the ν_4 mode in N_2O, the intensities of the modes are larger in the complex than the respective

intensity in the complex. The v_4 mode in N_2O shows that the frequency increases upon complexation, but the intensity of this mode decreases upon the formation. The change in the vibrational modes upon complexation are in part produced by the geometric differences discussed earlier, as well as the presence of the other atoms within the complex.

Similar to the observation of the harmonic modes, the intensities of the anharmonic modes are consistent between the aug-cc-pVDZ and aug-cc-pVTZ basis sets for both N_2O and H_2O monomers, indicating a good convergence of the structure

Table 3.6: Harmonic and anharmonic vibrational frequencies (cm^{-1}) and intensities (in km mol^{-1}) of H_2O, N_2O and the H_2O-N_2O complex

	aug-cc-pVDZ				aug-cc-pVTZ			
	Harmonic		Anharmonic		Harmonic		Anharmonic	
H_2O-N_2O	Frequency	Intensity	Frequency	Intensity	Frequency	Intensity	Frequency	Intensity
ν_1	67.8	20.9	45.7	21.9	67.7	27.0		
ν_2	129.6	189.4	9.7	15.7	96.1	183.7		
ν_3	133.9	0.1	48.8	129.4	124.5	4.4		
ν_4	162.3	73.0	133.2	33.6	151.5	53.7		
ν_5	223.1	26.1	125.5	25.8	201.6	30.9		
ν_6	562.3	4.2	555.7	3.2	589.5	5.2		
ν_7	563.2	3.7	557.6	3.0	591.1	4.1		
ν_8	1271.0	66.7	1256.6	63.3	1282.6	67.6		
ν_9	1631.7	115.4	1589.0	79.6	1638.9	114.6		
ν_{10}	2250.5	315.3	2189.5	287.4	2276.8	335.0		
ν_{11}	3785.2	2.5	3594.2	1.0	3808.5	3.8		
ν_{12}	3905.6	51.6	3699.4	37.9	3919.3	58.7		
H_2O								
ν_1	1638.2	65.5	1589.1	65.9	1645.9	70.4	1592.6	70.6
ν_2	3786.9	1.9	3599.1	0.9	3810.8	3.2	3637.4	1.9
ν_3	3904.9	46.4	3703.9	40.7	3919.9	54.4	3731.9	48.2
N_2O								
ν_1	567.1	3.0	559.7	2.5	593.2	3.7	587.1	3.4
ν_2	567.1	3.0	559.7	2.3	593.2	3.7	587.1	3.4
ν_3	1277.0	56.8	1261.0	57.7	1286.8	59.1	1275.8	57.4
ν_4	2240.8	359.3	2182.2	300.7	2266.5	377.0	2208.6	340.9

We obtain an estimation of the anharmonic correction upon the vibrational modes of the H_2O-N_2O complex, which is shown in Table 3.7. We calculate the difference in each vibrational mode by subtracting the harmonic frequency from the respective anharmonic value, which are seen in the column designated Δ. We then apply this change, all of which show a decrease, to the values of our CCSD(T)-F12b/cc-pVQZ-F12 data, and give values that represent the best estimate of the vibrational modes to take into account the anharmonic effect on the vibrational modes. The intermolecular vibrational modes are the most changed with the application of the correction. The calculated best esimate ν_2 mode gives a negative value, as the difference between the anharmonic and harmonic frequency for this mode obtained with the CCSD(T)/aug-cc-pVDZ method is larger than the CCSD(T)-F12b/cc-pVQZ-F12 harmonic frequency. It is the ν_6 and ν_7 modes, which are the previously degenerative modes from the N_2O monomer, that give the smallest change with the anharmonic correction.

Table 3.7: H_2O-N_2O best estimate frequencies using the aug-cc-pVDZ basis set

	Harmonic	Anharmonic	Δ	CCSD(T)-F12b/ cc-pVQZ-F12	Best estimate
	Frequency	Frequency		Frequency	Frequency
ν_1	67.8	45.7	-22.1	66.7	44.6
ν_2	129.6	9.7	-119.9	77.5	*[2]
ν_3	133.9	48.8	-85.1	121.5	36.4
ν_4	162.3	133.2	-29.1	157.0	127.9
ν_5	223.1	125.5	-97.6	205.9	108.3
ν_6	562.3	555.7	-6.6	597.6	591.0
ν_7	563.2	557.6	-5.6	598.9	593.3
ν_8	1271.0	1256.6	-14.4	1299.4	1285.0
ν_9	1631.7	1589.0	-42.7	1642.4	1599.7
ν_{10}	2250.5	2189.5	-61.0	2298.7	2237.7
ν_{11}	3785.2	3594.2	-191.0	3831.5	3640.5
ν_{12}	3905.6	3699.4	-206.2	3943.7	3737.5

[2] This calculated frequency is negative and therefore unreasonable

3.4 – Interaction energy of the H_2O-N_2O complex

In Table 3.8 we present the interaction energy of the H_2O-N_2O complex obtained with and without counterpoise correction. These interaction energies are calculated using the optimised geometry of the corresponding method from the respective structures shown in Tables 3.1-3.4.

We see a decrease of the interaction energy without the counterpoise correction with the increasing basis set size, with both the CCSD(T)-F12a and CCSD(T)-F12b methods. In contrast, we observe an increase in the counterpoise corrected interaction energy as the basis set increases to the CBS limit. As expected, in both of the CCSD(T)-F12a and CCSD(T)-F12b analyses, the standard calculations gave a smaller energy value than the respective counterpoise corrected value. It is also observed that the CCSSD(T)-F12a method gives slightly larger interaction energy than the CCSD(T)-F12b method.

Table 3.8: CCSD(T)-F12a and CCSD(T)-F12b interaction energies (kJ mol^{-1}) of the H_2O-N_2O complex obtained with and without counterpoise correction

	CCSD(T)-F12a		CCSD(T)-F12b	
	Standard	Counterpoise	Standard	Counterpoise
cc-pVDZ-F12	-11.45	-10.72	-11.19	-10.46
cc-pVTZ-F12	-11.20	-10.89	-11.15	-10.78
cc-pVQZ-F12	-11.20	-11.04	-11.19	-10.99
CBS			-11.09	
cc-pCVQZ-F12			-11.01	

In Table 3.9 we present our best estimate at the interaction energy of the H_2O-N_2O complex. This is calculated by taking the CCSD(T)-F12b CBS limit interaction energy and adding a correction for core correlation and a correction for zero-point vibrational energy. The core correlation correction is obtained as the difference between the counterpoise corrected all

electron CCSD(T)-F12b/cc-pCVQZ-F12 result and the counterpoise corrected frozen core CCSD(T)-F12b/cc-pVQZ-F12 result. The zero-point energy correction is obtained from the CCSD(T)-F12b/cc-pVQZ-F12 harmonic frequencies in Table 3.6.

Table 3.9: Best estimate of interaction energy of the H_2O-N_2O complex

	Energy ($kJmol^{-1}$)
CBS	-11.09
Core correction	-0.02
ZPVE correction	+3.96
Best estimate	**-8.85**

3.5 – Conclusion

We have optimized the structure of the H_2O-N_2O complex and calculated the interaction energy to be -8.85 $kJmol^{-1}$. When this is compared to the previous computationally determined structure in Figure 3.1b and the infrared determined structure in Figure 3.1c, we see a good match of the structure. Our present results confirm that the actual structure of H_2O-N_2O more closely resembles that determined by the infrared data, rather than the structure determined by the microwave data as per Figure 3.1a.

We show that upon formation of the complex the central nitrogen of the N_2O unit moves closer to the terminal nitrogen and that the H_2O bond lengths become non degenerative and the intramolecular of this portion increases in the formation.

within Chapter 7 we use the interaction energy and vibrational modes from the CCSD(T)-F12b/cc-pVQZ-F12 data to determine the thermodynamic parameters for the H2O-N2O complex

4 - Ar-N_2O

4.1 - Introduction

Argon is the third most abundant component of the atmosphere behind nitrogen and oxygen, which are discussed for their N_2O containing complexes in chapters 5 and 6 respectively. Despite the relatively inert nature of argon, it has been studied in the formation of complexes. Previous work of complexes containing argon have in part focussed on analysing dimers consisting of an argon atom weakly bonded to a linear molecule such as N_2O, OCS and CO_2. These structures have been examined using microwave or infrared spectroscopic techniques, or a combination of these methods.[68]

The structure of the Ar-N_2O complex has been previously investigated by both experimental and theoretical research groups. Studies of the excited state of the complex show that there is negligible change to the structure upon excitation from the ground to the vibrationally excited state.[68] The structure of the Ar-N_2O complex from Gimmler and Havenith, determined by rotationally resolved infrared analysis and shown in Figure 4.1, closely matches our investigated structure, (Figure 4.2).

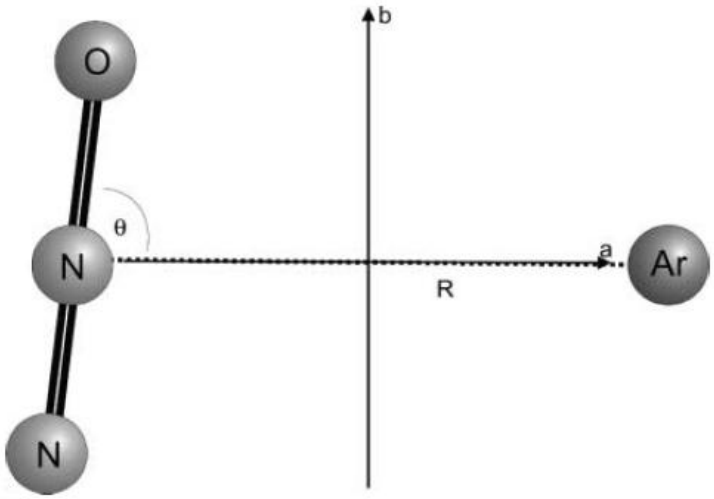

Figure 4.1: The structure of the Ar-N_2O complex determine by Gimmler and Havenith[69]

An earlier investigation by Hu, Chappell and Sharpe also used rotationally resolved infrared spectroscopic techniques on the Ar-N_2O complex.[68] They investigated the low frequency, intermolecular modes of the structure not determined by the studies of Gimmler and Havenith.

In this chapter we show the results of our investigation of the structure of Ar-N_2O, presenting the results for the optimised structure, vibrational modes and binding energy. Figure 4.2 shows the geometric parameters that were used in our investigation to define the Ar-N_2O structure. We conclude the chapter by presenting a "best estimate" structure and binding energy for Ar-N_2O that takes into account the effects of core correlation, complete basis set limit extrapolations and counterpoise corrections.

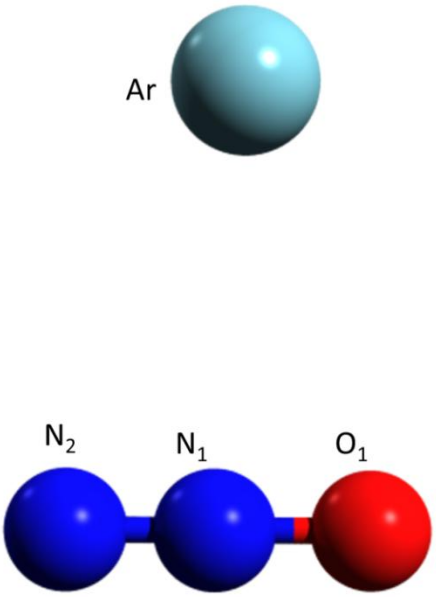

Figure 4.2: Geometric parameters used to define the structure of the Ar-N_2O complex

4.2 - Structure of the Ar-N_2O complex

In Tables 4.1 and 4.2 we present the CCSD(T)-F12a and CCSD(T)-F12b optimised geometric parameters of Ar-N_2O and N_2O monomer, obtained using the cc-pVxZ-F12 basis sets, (x=D,T,Q) including and excluding a counterpoise correction. Table 4.2 also contains reults obtained at the CCSD(T)-F12b/CBS limit. The CBS extrapolated limit is obtained from the cc-pVTZ-F12/cc-pVQZ-F12 basis set pair. Overall we find excellent agreement between the CCSD(T)-F12a and CCSD(T)-F12b results, with the differences shown in Table A.2 in the appendix.

Similar to the observation in the H_2O-N_2O complex, the geometric parameters optimised with the CCSD(T)-F12a and CCSD(T)-F12b methods rapidly converge with increasing basis set, yielding results in close agreement with the CBS limit. The relatively small differences between the standard and counterpoise corrected geometric parameters obtained with a given basis set indicates that BSSE is relatively small in these calculations.

The difference in the angles with and without counterpoise correction show the N_2N_1Ar intermolecular bond angle decrease is matched by the O_1N_1Ar angle increase by approximately the same magnitude. The variations are relatively small due to the inherently low potential energy surface for the intermolecular angles. As expected, we find that the difference between the geometric parameters with and without counterpoise correction optimization schemes decreases as the basis set size increases.

The cc-pVQZ-F12 calculation of the Ar-N_2O structure most closely matches the complete basis set limit. The intermolecular distance has closer agreement without counterpoise correction, whereas the intermolecular angles with counterpoise correction more closely match the CBS calculations. In both CCSD(T)-F12a and CCSD(T)-F12b calculations, the cc-pVQZ-F12 method shows less convergence of the intermolecular angles between with and without counterpoise correction, compared to the cc-pVDZ-F12 and cc-VTZ-F12 calculations.

We see a slight decrease in the intramolecular bond lengths upon complex formation with both the CCSD(T)-F12a and CCSD(T)-F12b methods.

Table 4.1: The CCSD(T)-F12a optimised structure of N_2O and the Ar-N_2O complex obtained with and without counterpoise correction

	cc-pVDZ-F12			cc-pVTZ-F12			cc-pVQZ-F12		
Ar-N_2O									
	Standard	Counterpoise	Difference	Standard	Counterpoise	Difference	Standard	Counterpoise	Difference
$R_{(O1N1)}$	1.1881	1.1881	0.0000	1.1870	1.1870	0.0000	1.1864	1.1864	0.0000
$R_{(N1N2)}$	1.1291	1.1291	0.0000	1.1282	1.1282	0.0000	1.1277	1.1277	0.0000
$R_{(N1Ar)}$	3.3817	3.4197	0.0380	3.3917	3.4084	0.0167	3.3935	3.4002	0.0067
$A_{(N2N1Ar)}$	94.03	93.95	-0.08	93.77	93.75	-0.02	93.69	93.55	-0.14
$A_{(O1N1Ar)}$	85.79	85.89	0.10	86.07	86.10	0.03	86.16	86.31	0.15
N_2O									
$R_{(NO)}$	1.1882			1.1871			1.1865		
$R_{(NN)}$	1.1291			1.1282			1.1277		

Table 4.2: The CCSD(T)-F12b optimised structure of N_2O and the Ar-N_2O complex obtained with and without counterpoise correction, and with the CBS limit

	cc-pVDZ-F12			cc-pVTZ-F12			cc-pVQZ-F12			CBS limit
Ar-N_2O										
	Standard	Counterpoise	Difference	Standard	Counterpoise	Difference	Standard	Counterpoise	Difference	
$R_{(O1N1)}$	1.1874	1.1874	0.0000	1.1867	1.1867	0.0000	1.1863	1.1863	0.0000	1.1863
$R_{(N1N2)}$	1.1288	1.1287	0.0000	1.1281	1.1281	0.0000	1.1277	1.1277	0.0000	1.1276
$R_{(N1Ar)}$	3.4013	3.4397	0.0383	3.3976	3.4165	0.0189	3.3950	3.4048	0.0098	3.3939
$A_{(N2N1Ar)}$	94.21	94.12	-0.09	93.84	93.82	-0.02	93.71	93.58	-0.13	93.45
$A_{(O1N1Ar)}$	85.63	85.73	0.10	86.01	86.04	0.03	86.15	86.28	0.13	86.40
N_2O										
$R_{(NO)}$	1.1882			1.1871			1.1865			1.1863
$R_{(NN)}$	1.1291			1.1282			1.1277			1.1276

In Tables 4.3 and 4.4 we present the CCSD(T)-F12a and the CCSD(T)-F12b optimised geometric parameters, respectively, of the Ar-N_2O complex obtained with the augmented basis sets aug-cc-pVxZ, (x=D,T,Q,5) including and excluding a counterpoise correction. We have chosen to investigate the Ar-N_2O complex with both the cc-pVxZ-F12 and aug-cc-pV(x)Z basis sets as there has been a suggestion in the literature that the former basis set does not include a sufficient number of diffuse basis functions to accurately describe very weak van der Waals type interactions. It is worth noting that the cc-pVxZ-F12 basis sets do include diffuse basis functions but only s and p type. Similar to the observations for the cc-pVxZ-F12 basis sets, the aug-cc-pVxZ results show an overall excellent agreement between the CCSD(T)-F12a and CCSD(T)-F12b results.

The main difference we see between the cc-pVxZ-F12 and aug-cc-pVxZ calculations is in the intermolecular angles, where $A_{(N2N1Ar)}$ is shown to decrease upon application of the counterpoise correction with the cc-pVxZ-F12 methods, but increases here for the augmented calculations. Similarly, the $A_{(O1N1Ar)}$ angle increases upon application of the counterpoise correction with the cc-pVxZ-F12 methods, and decreases for the augmented calculations

Table 4.3: The CCSD(T)-F12a optimised structure of N_2O and the Ar-N_2O complex, using the aug-cc-pVxZ basis sets, obtained with and without counterpoise correction

	aug-cc-pVDZ			aug-cc-pVTZ		
Ar-N_2O	Standard	Counterpoise	Difference	Standard	Counterpoise	Difference
$R_{(O1N1)}$	1.1874	1.1874	0.0000	1.1869	1.1869	0.0000
$R_{(N1N2)}$	1.1285	1.1285	0.0000	1.1281	1.1281	0.0000
$R_{(N1Ar)}$	3.3327	3.3776	0.0449	3.3827	3.4018	0.0191
$A_{(N2N1Ar)}$	93.14	93.54	0.40	93.54	93.72	0.18
$A_{(O1N1Ar)}$	86.64	86.27	-0.37	86.3	86.13	-0.17
N_2O						
$R_{(NN)}$	1.1285			1.1281		
$R_{(NO)}$	1.1875			1.1870		

	aug-cc-pVQZ			aug-cc-pV5Z		
Ar-N_2O	Standard	Counterpoise	Difference	Standard	Counterpoise	Difference
$R_{(O1N1)}$	1.1864	1.1864	0.0000	1.1864	1.1864	0.0000
$R_{(N1N2)}$	1.1276	1.1276	0.0000	1.1276	1.1279	0.0003
$R_{(N1Ar)}$	3.3910	3.3973	0.0063	3.4110	3.3943	-0.0167
$A_{(N2N1Ar)}$	93.73	93.74	0.01	96.43	95.53	-0.90
$A_{(O1N1Ar)}$	86.13	86.12	-0.01	83.51	84.22	0.71
N_2O						
$R_{(NN)}$	1.1276			1.1276		
$R_{(NO)}$	1.1865			1.1864		

Table 4.4: The CCSD(T)-F12b optimised structure of N_2O and the Ar-N_2O complex, using the aug-cc-pVxZ basis sets, obtained with and without counterpoise correction

	aug-cc-pVDZ			aug-cc-pVTZ		
Ar-N_2O	Standard	Counterpoise	Difference	Standard	Counterpoise	Difference
$R_{(O1N1)}$	1.1860	1.1860	0.0000	1.1865	1.1865	0.0000
$R_{(N1N2)}$	1.1281	1.1281	0.0000	1.1281	1.1281	0.0000
$R_{(N1Ar)}$	3.3552	3.3995	0.0443	3.3886	3.4111	0.0225
$A_{(N2N1Ar)}$	93.32	93.76	0.44	93.59	93.8	0.21
$A_{(O1N1Ar)}$	86.48	86.07	-0.41	86.26	86.06	-0.20
N_2O						
$R_{(NN)}$	1.1287			1.1282		
$R_{(NO)}$	1.1867			1.1866		

	aug-cc-pVQZ			aug-cc-pV5Z		
Ar-N_2O	Standard	Counterpoise	Difference	Standard	Counterpoise	Difference
$R_{(O1N1)}$	1.1862	1.1862	0.0000	1.1862	1.1862	0.0000
$R_{(N1N2)}$	1.1276	1.1276	0.0000	1.1276	1.1276	0.0000
$R_{(N1Ar)}$	3.3927	3.4023	0.0097	3.3916	3.3963	0.0047
$A_{(N2N1Ar)}$	93.76	93.77	0.01	93.76	93.74	-0.01
$A_{(O1N1Ar)}$	86.09	86.08	-0.01	86.10	86.11	0.01
N_2O						
$R_{(NN)}$	1.1277			1.1276		
$R_{(NO)}$	1.1863			1.1863		

In Table 4.5 we present the CCSD(T)-F12b optimised geometric parameters of Ar-N_2O and the N_2O monomer obtained with the cc-pVQZ-F12 basis set utilising the frozen core approximation and with the cc-pCVQZ-F12 basis set correlating all electrons. The difference between these two calculations is used as an estimate of the effect of core correlation.

Similar to the observed trends in the H_2O-N_2O chapter, inclusion of core correlation consistently reduces the bond lengths in the Ar-N_2O complex. This also shows an effect on the bond angles, in which the argon atom becomes closer to the terminal nitrogen atom. Core correlation has a greater effect on the intermolecular bond length than it does on the intramolecular bond lengths.The intermolecular bond length is approximately three times larger however the change upon application of the core correlation is approximately twice as large when the percent change is considered.

Also shown in Table 4.5 is our best estimate of the geometric parameters of the Ar-N_2O complex. This structure is obtained by adding the difference between the all electron cc-pCVQZ-F12 optimization and frozen core cc-pVQZ-F12 optimization to the CBS limit structure.

Table 4.5: All electron and frozen core counterpoise corrected optimised geometric parameters of N_2O and the Ar-N_2O complex obtained with the CCSD(T)-F12b method

	cc-pVQZ-F12	cc-pCVQZ-F12	Difference	CCSD(T)-F12b/CBS	Best estimate
Ar-N_2O					
$R_{(O1N1)}$	1.1868	1.1841	-0.0027	1.1862	1.1835
$R_{(N1N2)}$	1.1283	1.1254	-0.0029	1.1276	1.1248
$R_{(N1Ar)}$	3.4184	3.4032	-0.0152	3.3971	3.3818
$A_{(N2N1Ar)}$	94.24	93.48	-0.76	93.49	92.73
$A_{(O1N1Ar)}$	85.62	86.38	0.77	86.36	87.13
N_2O					
$R_{(NO)}$	1.1864	1.1842	-0.0022	1.1863	1.1841
$R_{(NN)}$	1.1277	1.1254	-0.0022	1.1276	1.1254

In Table 4.6 we present the optimized geometric parameters of Ar-N_2O obtained with conventional CCSD(T) and the aug-cc-pVxZ basis sets, (x=D,T), and at the CCSD(T)-F12b/CBS limit. The CCSD(T) results were obtained with CFOUR utilizing analytical derivatives whereas the CCSD(T)-F12b/CBS result was obtained using MOLPRO with numerical derivatives. We find that the CCSD(T) optimized geometric parameters converge towards the CBS limit as the basis set increases from aug-cc-pVDZ to aug-cc-pVTZ. As expected, the calculated bond lengths become shorter as the basis set increases. There is no systematic change in the calculated bond angles. Overall, we find that the CCSD(T)/aug-cc-pVTZ optimised geometric parameters are in reasonable agreement with the CCSD(T)-F12b/CBS limit. The CCSD(T)/aug-cc-pVTZ optimised bond lengths are between 0.004-0.010 Å longer than the CCSD(T)-F12b/CBS limit, with the largest variation observed for the intermolecular bond length change. This is expected since this bond length is approximately three times as long in magnitude as either of the intramolecular bond length, and because this is the parameter most affected by BSSE. The corresponding bond angles have flatter

potentials, hence there is more variation between these two methods with up to 1.0° difference observed here.

Table 4.6: The structure of N_2O and the Ar-N_2O complex optimised with conventional CCSD(T) and at the explicitly correlated CCSD(T)-F12b/CBS limit

	CCSD(T)/aug-cc-pVDZ	CCSD(T)/aug-cc-pVTZ	CCSD(T)-F12b/CBS	Difference
Ar-N_2O				
$R_{(O1N1)}$	1.2018	1.1911	1.1862	-0.0049
$R_{(N1N2)}$	1.1491	1.1326	1.1276	-0.0049
$R_{(N1Ar)}$	3.4878	3.3875	3.3971	0.0096
$A_{(N2N1Ar)}$	94.08	93.00	93.49	0.49
$A_{(O1N1Ar)}$	85.86	86.86	86.36	-0.50
N_2O				
$R_{(NO)}$	1.2018	1.1912	1.1863	-0.0049
$R_{(NN)}$	1.1491	1.1326	1.1276	-0.0050

It is expected that the experimental value for the intermolecular bond length will be larger than our calculated value because our calculations determine the equilibrium bond length, which doesn't take into account vibrational averaging of the bond length. We obtain both a value with aug-cc-pVTZ for the difference between the ground state and equilibrium intermolecular distance of approximately 0.10Å, which is a good comparison to the difference between the experimental distance and our value, which gave a difference of between 0.08 and 0.10Å

It has been previously determined by Gimmler and Havenith that the T-shaped structure had the parameters of 3.4686Å for the intermolecular bond length and 82.92^0 for the oxygen-nitrogen-argon angle in this intermolecular interaction.[69] This angle closer matches our observation of the argon atom being closer to the terminal oxygen, rather than being closer to the terminal nitrogen.

The analysis by Hu, Chappell and Sharpe gave an intermolecular bond length of 3.482Å and the oxygen-nitrogen-argon intermolecular angle of 81.69°.[68] Both of these parameters are less consistent with our best estimate parameters than those stated in Gimmler and Havenith.[69]

4.3 - Vibrational modes of the Ar-N_2O complex

In Table 4.7 we present harmonic vibrational frequencies of N_2O and the Ar-N_2O complex calculated with the CCSD(T)-F12a and CCSD(T)-F12b methods, and the cc-pVxZ-F12 basis sets. These results were obtained without counterpoise correction using the standard geometries from Tables 4.1 and 4.2. No vibrational intensities are presented as these cannot be calculated in MOLPRO due to the use of numerical energy derivatives.

The vibrational modes of the Ar-N_2O complex can be seen to vary only slightly between the CCSD(T)-F12a and CCSD(T)-F12b results. There is also little variation between the harmonic frequencies obtained with the different basis sets, indicating that the results are close to being converged to the CBS limit. The intermolecular vibrational modes of the Ar-N_2O complex are seen to be slightly smaller with the CCSD(T)-F12b method than using the CCSD(T)-F12a method. However, the opposite trend is observed for the intramolecular vibrational modes with CCSD(T)-F12b method giving slightly larger values for the vibrational frequencies than those calculated with the CCSD(T)-F12a method.

Similar to the observation in the previous chapter, the lowest energy vibrational mode of N_2O monomer increases by approximately 13 cm^{-1} upon complexation. This doubly-degenerate mode in the monomer separates by a maximum of 0.3 cm^{-1} in the complex. We observe that the largest mode around 2260 cm^{-1} in the N_2O monomer increases by approximately 20 cm^{-1} upon complexation, with the other vibrational mode of the N_2O monomer decreasing by approximately 3 $cm^{-1}$when the complex is formed .

Table 4.7: Harmonic vibrational frequencies (cm^{-1}) of N_2O and the Ar-N_2O complex calculated with the CCSD(T)-F12a and CCSD-F12b methods and the cc-pVxZ-F12 (x=D,T,Q) basis set

	cc-pVDZ-F12		cc-pVTZ-F12		cc-pVQZ-F12	
	CCSD(T)-F12a	CCSD(T)-F12b	CCSD(T)-F12a	CCSD(T)-F12b	CCSD(T)-F12a	CCSD(T)-F12b
Ar-N_2O						
ν_1	41.0	40.0	40.2	39.9	38.9	39.0
ν_2	49.4	47.6	47.1	46.6	46.3	46.0
ν_3	594.6	595.8	599.0	599.1	599.8	600.0
ν_4	594.8	596.1	599.1	599.2	599.9	600.0
ν_5	1298.4	1301.4	1301.9	1303.1	1303.2	1303.8
ν_6	2282.0	2283.1	2286.7	2287.2	2288.8	2289.1
N_2O						
ν_1	581.7	583.3	586.5	586.7	587.8	588.0
ν_2	581.8	583.3	586.6	586.7	587.8	588.0
ν_3	1300.4	1303.7	1304.6	1305.9	1306.2	1306.8
ν_4	2259.7	2260.3	2264.6	2265.1	2266.0	2266.3

In Table 4.8 we present the harmonic and anharmonic vibrational frequencies and intensities for N_2O and the Ar-N_2O complex calculated with conventional CCSD(T) and the aug-cc-pVxZ basis sets (x=D,T). These results were obtained without counterpoise correction using the geometries from Table 4.6. The anharmonic results were calculated within the second order vibrational perturbation theory (VPT2) framework.

Similar to the observation for the H_2O-N_2O complex, the harmonic frequencies calculated with conventional CCSD(T) and the aug-cc-pVDZ or aug-cc-pVTZ basis set are in general slightly smaller than those calculated with explicitly correlated CCSD(T)-F12b and the cc-pVDZ-F12 or cc-pVTZ-F12 basis set. This observation excludes the intermolecular stretching mode ν_2 mode. This difference is expected, as bond lengths contract and hence harmonic frequencies become larger as the basis set increases towards the CBS limit. The explicitly correlated results are therefore closer to the CBS limit than the conventional results.

The harmonic and anharmonic vibrational modes, as well as their intensities, for the Ar-N_2O complex shows a reasonable consistency between the aug-cc-pVDZ and aug-cc-pVTZ results, indicating that these are reasonably well converged with respect to the CBS limit.

As expected, in both of the N_2O monomer and for the complex, the anharmonic vibrational frequencies are calculated to be smaller than the respective harmonic frequencies. The intermolecular vibrational frequencies appear to be reasonable, however there is a larger relative change in the intermolecular vibrational modes than the intramolecular vibrational modes.We see a small variation between the cc-pVDZ and cc-pVTZ anharmonic frequencies, which would be expected for the change in the basis set used.

There is very little change in the vibrational modes of N_2O upon formation of the Ar-N_2O complex. The degenerative modes of the N_2O monomer form slightly non-degenerative modes in the complex, with the harmonic modes with the aug-cc-pVTZ basis set showing the same frequency but different intensities for these modes. These modes show a slight decrease upon complexation with the aug-cc-pVDZ basis set, but there is no consistent change for the aug-cc-pVTZ results. As was shown in Table 4.6, there was negligible difference in the geometric parameters of the N_2O unit upon formation of the complex, which is reflected in the very small changes to the vibrational modes. Not surprisingly, we find the intermolecular vibrational modes show the largest amount of anharmonicity. While some intramolecular vibrational modes give larger differences between the harmonic and anharmonic modes , the relative change is smaller than the differences in the intermolecular modes.

Table 4.8: Harmonic and anhamonic vibrational frequencies (cm^{-1}) and intensities (in km mol^{-1}) of N_2O and the Ar-N_2O complex calculated with the CCSD(T) method

	aug-cc-pVDZ				aug-cc-pVTZ			
	Harmonic		Anharmonic		Harmonic		Anharmonic	
Ar-N_2O	Frequency	Intensity	Frequency	Intensity	Frequency	Intensity	Frequency	Intensity
ν_1	35.9	0.1	11.8	0.0	33.4	0.0	26.8	0.0
ν_2	40.4	0.0	7.7	0.0	62.1	0.0	57.2	0.0
ν_3	565.2	3.8	559.0	3.4	593.6	4.5	587.9	4.0
ν_4	566.3	2.8	559.1	2.6	593.6	3.3	586.9	3.1
ν_5	1277.3	53.4	1261.2	53.7	1286.4	54.3	1275.7	52.3
ν_6	2241.1	331.9	2181.7	298.8	2265.8	345.9	2207.8	312.7
N_2O								
ν_1	567.1	3.0	559.7	2.5	593.2	3.7	587.1	3.4
ν_2	567.1	3.0	559.7	2.3	593.2	3.7	587.1	3.4
ν_3	1277.0	56.8	1261.0	57.7	1286.8	59.1	1275.8	57.4
ν_4	2240.8	359.3	2182.2	300.7	2266.5	377.0	2208.6	340.9

In Table 4.9 we present our best estimate vibrational frequencies for the Ar-N_2O complex. These are calculated by adding the difference between the harmonic and anharmonic frequencies obtained with conventional CCSD(T) to the CCSD(T)-F12b/cc-pVQZ-F12 results.

The magnitude of this anharmonic correction (denoted Δ) appears more physically sensible for the aug-cc-pVTZ results tha the aug-cc-pVDZ results. This is especially evident in the two lowest frequency intermolecular modes, which show large relative differences with the aug-cc-pVDZ basis set.

We also show in Table 4.9 the experimental vibrational modes of the Ar-N_2O complex collected from various experimental studies. The best estimate vibrational frequencies with the aug-cc-pVTZ basis set show in general a better consistency with the experimental frequencies than the frequencies with the aug-cc-pVDZ basis set. However, the ν_5 frequency with the aug-cc-pVDZ basis set shows a closer value to the best estimate than the respective frequency with the aug-cc-pVTZ basis set.

Table 4.9: Ar-N_2O Harmonic and anharmonic frequencies using the aug-cc-pVxZ (x=D,T) basis set, best estimate and experimental modes

	Harmonic		Anharmonic		Δ	CCSD(T)-F12b/cc-pVQZ-F12	Best estimate	Experimental
aug-cc-pVDZ	frequency	Intensity	frequency	Intensity		frequency	frequency	
ν_1	35.9	0.1	11.8	0.0	-24.1	39.0	14.9	33.0[3]
ν_2	40.4	0.0	7.7	0.0	-32.7	46.0	13.3	40.1[3]
ν_3	565.2	3.8	559.0	3.4	-6.2	600.0	593.8	
ν_4	566.3	2.8	559.1	2.6	-7.2	600.0	592.8	
ν_5	1277.3	53.4	1261.2	53.7	-16.1	1303.8	1287.7	1285.1[4]
ν_6	2241.1	331.9	2181.7	298.8	-59.4	2289.1	2229.7	2256.1[5]
aug-cc-pVTZ								
ν_1	33.4	0.0	26.8	0.0	-6.6	39.0	32.4	33.0
ν_2	62.1	0.0	57.2	0.0	-4.9	46.0	41.1	40.1
ν_3	593.6	4.5	587.9	4.0	-5.7	600.0	594.3	
ν_4	593.6	3.3	586.9	3.1	-6.7	600.0	593.3	
ν_5	1286.4	54.3	1275.7	52.3	-10.7	1303.8	1293.1	1285.1
ν_6	2265.8	345.9	2207.8	312.7	-58.0	2289.1	2231.1	2256.1

[3] Ngari and Jager[70]

[4] Gimmler and Havenith[69]

[5] Hu, Chappell and Sharpe[68]

4.4 - Interaction energy of the Ar-N_2O complex

In Table 4.10 we present the interaction energy of the Ar-N_2O complex obtained with and without counterpoise correction. These interaction energies are calculated using the optimised geometry of the corresponding method from the respective structures shown in Tables 4.1-4.6.

As expected, we find that the non-counterpoise corrected interaction energies are larger in magnitude than the respective counterpoise corrected values, and is seen for both of the aug-cc-pVxZ and cc-pVxZ-F12 basis sets. In general, the CCSD(T)-F12a interaction energies are calculated to be slightly larger than the CCSD(T)-F12b results for the same basis set size with both the aug-cc-pVxZ and cc-pVxZ-F12 basis sets.

In general we find that the interaction energy obtained with the aug-cc-pVxZ basis sets are slightly larger than the corresponding cc-pVxZ-F12 basis sets. The aug-cc-pVxZ results are 0.13-0.16 kJ mol^{-1} larger than the cc-pVxZ-F12 results for both CCSD(T)-F12 methods including and excluding counterpoise correction.

Table 4.10: CCSD(T)-F12a and CCSD(T)-F12b interaction energies (kJ mol^{-1}) of the Ar-N_2O complex obtained with and without counterpoise correction

	CCSD(T)-F12a		CCSD(T)-F12b	
	Standard	Counterpoise	Standard	Counterpoise
cc-pVDZ-F12	-3.04	-2.53	-2.83	-2.35
cc-pVTZ-F12	-2.67	-2.45	-2.62	-2.38
cc-pVQZ-F12	-2.56	-2.45	-2.55	-2.42
CBS			-2.46	
cc-pCVQZ-F12			-2.32	
aug-cc-pVDZ	-3.29	-2.55	-2.57	-2.22
aug-cc-pVTZ	-2.86	-2.58	-2.84	-2.48
aug-cc-pVQZ	-2.70	-2.60	-2.71	-2.55
aug-cc-pV5Z	-2.74	-2.66	-2.71	-2.64

In Table 4.11 we present our best estimate at the interaction energy of the Ar-N_2O complex. This is calculated by taking the CCSD(T)-F12b CBS limit interaction energy and adding a correction for core correlation and a correction for zero-point energy. The core correlation correction is obtained as the difference between the counterpoise corrected all electron CCSD(T)-F12b/cc-pCVQZ-F12 result and the counterpoise corrected frozen core CCSD(T)-F12b/cc-pVQZ-F12 result. The zero-point energy correction is obtained from the CCSD(T)-F12b/cc-pVQZ-F12 harmonic frequencies in Table 4.7.

Table 4.11: Best estimate of interaction energy of the Ar-N_2O complex

	Energy ($kJmol^{-1}$)
CBS	-2.46
Core correction	-0.09
ZPVE correction	+0.70
Best estimate	**-1.85**

4.5 – Conclusion

We have investigated the lowest energy structure of the Ar-N_2O complex. We find that the structure is approximately T-shape, which is consistent with earlier experimental and theoretical investigations. Our best estimate of the interaction energy is -1.85 $kJmol^{-1}$.

Unlike the observations in the H_2O -N_2O complex, there is minimal change in the structure of the N_2O unit upon formation of the complex.

The Ar-N_2O complex exhibits the weakest interaction energy of all the complexes considered in this thesis. Consequently, we investigated it with both the cc-pVxZ-F12 and aug-cc-pVxZ basis set series. For a given cardinal number, we find there to be relatively small but appreciable differences between the results obtained with the two basis sets.

5 - N_2-N_2O

5.1 - Introduction

Nitrogen represents the major portion of Earth's atmosphere at approximately 78% of the total atmosphere, and has therefore been important in the study of atmospheric complexes.

The rotationally resolved infrared spectra of the N_2-N_2O structure was first reported by Randall, Dyke and Howard.[71] This structure is seen in Figure 5.1, and matches our investigated structure, with the N_2 unit angled pointed toward the terminal nitrogen of the N_2O unit and positioned over the terminal oxygen atom.

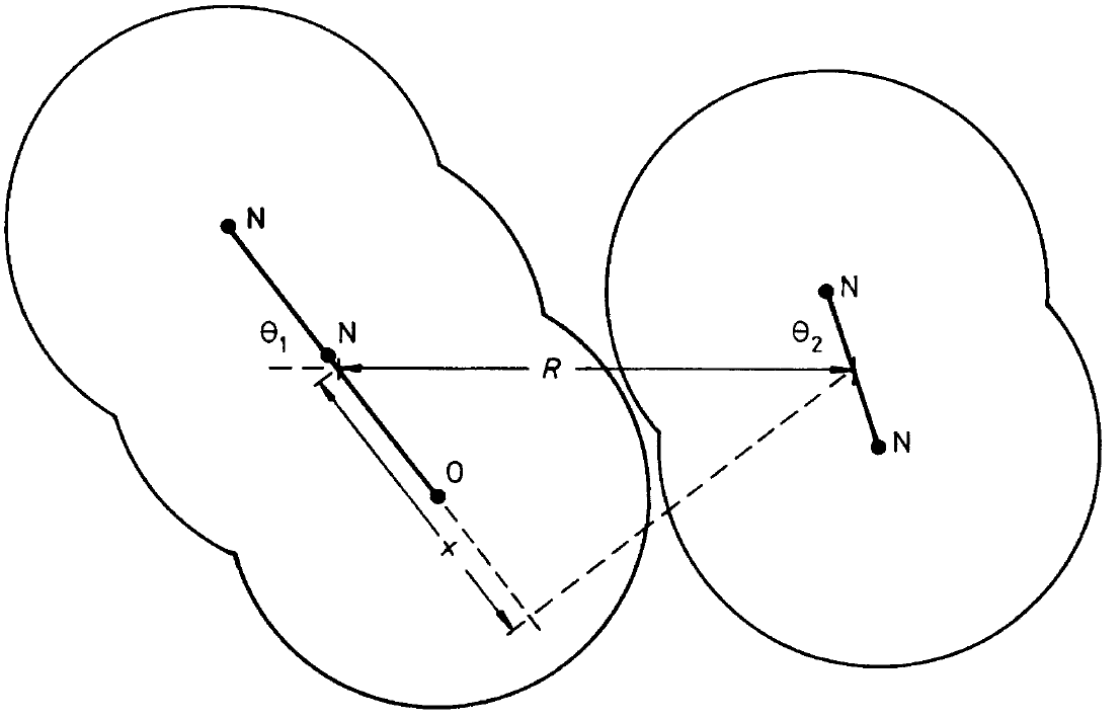

Figure 5.1: Co-ordinates of the N_2-N_2O complex of Randall, Dyke and Howard [71]

Previous work on the theoretical computed structure obtained the structure, interaction energy and vibrational spectra using the Gaussian 98 program employing MP2 theory with the 6-311+G(d) basis set.[72] This was, at least in part, due to the computational limits of the time which our work hopes to address.

In this chapter we present results for the optimised structure, vibrational modes and binding energy of N_2-N_2O that we have conducted. Figure 5.2 shows the geometric parameters that were used to define the N_2-N_2O structure. We conclude the chapter by presenting a best estimate of the structure and binding energy for N_2-N_2O that takes into account the effects of core correlation, complete basis set limit extrapolations and counterpoise corrections.

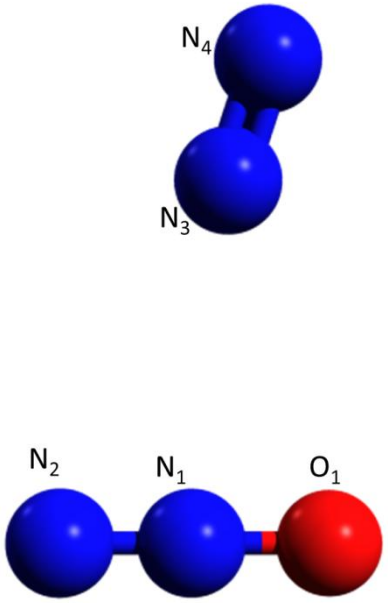

Figure 5.2: Geometric parameters used to define the structure of the N_2-N_2O complex

5.2 - Structure of the N_2-N_2O complex

In Tables 5.1 and 5.2 we present the CCSD(T)-F12a and CCSD(T)-F12b optimised geometric parameters of N_2-N_2O, obtained using the cc-pVxZ-F12 basis sets, (x=D,T,Q), including and excluding a counterpoise correction. Table 5.2 also includes the optimised geometric parameters calculated at the CCSD(T)-F12b/CBS limit. Overall we find excellent agreement between the CCSD(T)-F12a and CCSD(T)-F12b results, with the differences shown in Table A.3 in the appendix. The CBS limit is obtained from the cc-pVTZ-F12/cc-pVQZ-F12 basis set pair.

Consistent with the previous chapters, we find that geometric parameters optimised with the CCSD(T)-F12a and CCSD(T)-F12b methods rapidly converge with increasing basis set, with even the smallest cc-pVDZ-F12 basis set yielding results in close agreement with the CBS limit.

There are relatively small differences between the standard and counterpoise corrected geometric parameters obtained with a given basis set, which like the other complexes, indicates that basis set superposition error (BSSE) is relatively small. As expected, the greatest differences between the standard and counterpoise corrected results are observed for the intermolecular bond distance and angles.

The difference in the angles between the calculations with and without counterpoise correction exhibit a slight increase in the $N_2N_1N_3$ bond angle that is matched by a decrease in the $O_1N_1N_3$ bond angle of an approximately equal magnitude. Nonetheless these variations are relatively small given the inherently low potential energy surface of intermolecular angles.

Not surprisingly, the geometric parameters optimized with the the cc-pVQZ-F12 CCSD(T)-F12b method most closely match those obtained at the CBS limit. In general, we observe a slight contraction of the optimized bond lengths between the CCSD(T)-F12a and CCSD(T)-F12b results, which is shown in the appendix in Table A.3.

The NN bond from the N_2O portion is seen to decrease by slightly upon formation of the complex, whereas there is negligible change in the other intramolecular bond lengths.

The calculated bond lengths of the N_2-N_2O complex, as well as the N_2O and N_2 monomers, are seen to decrease in length with the increasing basis set size. This trend is observed in both the standard and counterpoise corrected results, and is especially evident in the decreasing length of the intermolecular distance with increasing basis set size, R_{N1N3}. In a similar observation, we show that the intermolecular angle, $A_{(N2N1N3)}$ increases as the basis set size. The change in this angle closely matches the value of the change in the $A_{(O1N1N3)}$ angle, which is expected from a shifting of molecules from each other. This indicates that as the basis set size increases, the N_2 molecule moves closer to the N_2O axis, making a structure where the closest nitrogen atom is more perpendicular to the N_2O molecules axis. The other intermolecular angle, $A_{(N4N3N1)}$, is also seen to increase in magnitude with the increasing basis set size. This corroborates the fact that the N_2 unit becomes closer to a perpendicular angle as the basis set size increases.

In both the CCSD(T)-F12a and CCSD(T)-F12b results, the distance of the NN bond in the N_2 monomer is seen to decrease in magnitude as the basis set size increases. The intramolecular parameters are consistent between the complete basis set extrapolation values and the CCSD(T)-F12b/cc-pVQZ-F12 values, both for the standard and counterpoise optimizations. Of the intramolecular bond lengths, both of the NN bond lengths in the N_2 and N_2O units, show no change between the standard and counterpoise corrected optimized values.

We show that the length of the intermolecular distance is longer with the counterpoise correction than the respective standard optimized value, in both the CCSD(T)-F12a and CCSD(T)-F12b results. The difference between the data sets reduces with the increasing basis set size. For the cc-pVQZ-F12 results, the standard optimized intermolecular distance is found to be slightly closer to the CBS limit than the counterpoise corrected value whereas the opposite is true for the intermolecular angles.

Table 5.1: The CCSD(T)-F12a optimised structure of N_2, N_2O and the N_2-N_2O complex obtained with and without counterpoise correction

	cc-pVDZ-F12			cc-pVTZ-F12			cc-pVQZ-F12		
N_2-N_2O									
	Standard	Counterpoise	Difference	Standard	Counterpoise	Difference	Standard	Counterpoise	Difference
$R_{(O1N1)}$	1.1882	1.1881	-0.0001	1.1870	1.1869	-0.0001	1.1864	1.1863	-0.0001
$R_{(N1N2)}$	1.1288	1.1288	0.0000	1.1279	1.1279	0.0000	1.1274	1.1274	0.0000
$R_{(N3N4)}$	1.1002	1.1002	0.0000	1.0994	1.0994	0.0000	1.0989	1.0989	0.0000
$R_{(N1N3)}$	3.1203	3.1378	0.0175	3.1147	3.1226	0.0079	3.1104	3.1137	0.0033
$A_{(N2N1N3)}$	95.73	95.46	-0.27	95.61	95.29	-0.32	95.43	95.22	-0.21
$A_{(O1N1N3)}$	84.16	84.45	0.29	84.30	84.62	0.32	84.47	84.68	0.21
$A_{(N4N3N1)}$	165.46	166.86	1.40	166.15	167.45	1.30	167.20	167.78	0.58
N_2O									
$R_{(NO)}$	1.1882			1.1871			1.1865		
$R_{(NN)}$	1.1291			1.1282			1.1277		
N_2									
$R_{(NN)}$	1.1003			1.0995			1.099		

Table 5.2: The CCSD(T)-F12b optimised structure of N_2, N_2O and the N_2-N_2O complex obtained with and without counterpoise correction, and with the CBS limit

	cc-pVDZ-F12			cc-pVTZ-F12			cc-pVQZ-F12			CBS limit
N_2-N_2O	Standard	Counterpoise	Difference	Standard	Counterpoise	Difference	Standard	Counterpoise	Difference	
$R_{(N1O1)}$	1.1874	1.1873	-0.0001	1.1867	1.1866	-0.0001	1.1862	1.1862	0.0000	1.1862
$R_{(N1N2)}$	1.1284	1.1284	0.0000	1.1278	1.1278	0.0000	1.1273	1.1273	0.0000	1.1273
$R_{(N3N4)}$	1.0997	1.0997	0.0000	1.0992	1.0992	0.0000	1.0988	1.0988	0.0000	1.0988
$R_{(N1N3)}$	3.1317	3.1500	0.0183	3.1178	3.1274	0.0096	3.111	3.1162	0.0052	3.1085
$A_{(N2N1N3)}$	95.67	95.41	-0.26	95.61	95.3	-0.31	95.43	95.23	-0.20	95.19
$A_{(O1N1N3)}$	84.24	84.51	0.27	84.3	84.62	0.32	84.47	84.68	0.21	84.71
$A_{(N4N3N1)}$	166.1	167.42	1.32	166.33	167.59	1.26	167.26	167.85	0.59	167.95
N_2O										
$R_{(NO)}$	1.1874			1.1868			1.1864			1.1863
$R_{(NN)}$	1.1287			1.1281			1.1277			1.1276
N_2										
$R_{(NN)}$	1.0999			1.0993			1.0989			1.0989

In Table 5.3 we present the CCSD(T)-F12b optimised geometric parameters of N_2, N_2O and the N_2-N_2O complex obtained with the cc-pVQZ-F12 basis set utilising the frozen core approximation and with the cc-pCVQZ-F12 basis set correlating all electrons. The difference between these two calculations is used as an estimate of the effect of core correlation.

We find that the inclusion of core correlation consistently reduces the intramolecular bond lengths by approximately 0.002Å, but increases the intermolecular bond length to a smaller magnitude. This contrasts the observation in the previous chapters where all of the bond lengths decrease with the inclusion of core correlation. It also has an appreciable but non-systematic effect on the bond angles.

Also shown in Table 5.3 is our best estimate of the geometric parameters of the N_2-N_2O complex. This structure is obtained by adding the difference between the all electron cc-pCVQZ-F12 optimization and frozen core cc-pVQZ-F12 optimization to the CBS limit structure. We find that the "best estimate" geometry is in excellent agreement with the all electron CCSD(T)-F12b/cc-pCVQZ-F12 structure, highlighting again the impressive basis set convergence obtained with the explicitly correlated CCSD(T)-F12b method.

Table 5.3: All electron and frozen core counterpoise corrected optimised geometric parameters of N_2, N_2O and the N_2-N_2O complex obtained with the CCSD(T)-F12b method

	cc-pVQZ-F12	cc-pCVQZ-F12	Difference	CCSD(T)-F12b/CBS	Best estimate
N_2-N_2O					
$R_{(N1O1)}$	1.1862	1.1840	-0.0022	1.1862	1.1840
$R_{(N1N2)}$	1.1273	1.1251	-0.0022	1.1273	1.1251
$R_{(N3N4)}$	1.0988	1.0967	-0.0021	1.0988	1.0967
$R_{(N1N3)}$	3.1110	3.1123	+0.0013	3.1085	3.1108
$A_{(N2N1N3)}$	95.43	95.16	-0.27	95.19	94.92
$A_{(O1N1N3)}$	84.47	84.75	+0.28	84.71	84.99
$A_{(N4N3N1)}$	167.26	168.09	+0.83	167.95	168.78
N_2O					
$R_{(NO)}$	1.1864	1.1842	-0.0022	1.1863	1.1841
$R_{(NN)}$	1.1277	1.1254	-0.0022	1.1276	1.1254
N_2					
$R_{(NN)}$	1.0989	1.0968	-0.0021	1.0989	1.0968

In Table 5.4 we present the optimized geometric parameters of N_2-N_2O obtained with conventional CCSD(T) and the aug-cc-pVxZ basis sets, (x=D,T), and at the CCSD(T)-F12b/CBS limit.

As expected, we find that the CCSD(T) optimized geometric parameters converge towards the CBS limit as the basis set increases from aug-cc-pVDZ to aug-cc-pVTZ. The calculated bond lengths become shorter as the basis set increases, however here is no systematic change in the calculated bond angles. For easy comparison, we also show in Table 5.4 the difference between the CCSD(T)/aug-cc-pVTZ and CCSD(T)-F12b/CBS optimized geometric parameters. Overall, we find that the CCSD(T)/aug-cc-pVTZ optimised geometric parameters are in reasonable agreement with the CCSD(T)-F12b/CBS limit. The CCSD(T)/aug-cc-pVTZ optimised intramolecular bond lengths are approximately 0.005 Å longer than the CCSD(T)-F12b/CBS limit, wheras the CCSD(T)/aug-cc-pVTZ optimised intermolecular bond length is approximately 0.017 Å shorter than the CCSD(T)-F12b/CBS limit value. The corresponding bond angles have flatter potentials; hence there is more variation between these two methods with up to a 0.3° difference.

Table 5.4: The structure of N_2, N_2O and the N_2-N_2O complex optimised with conventional CCSD(T) and at the explicitly correlated CCSD(T)-F12b/CBS limit

	CCSD(T)/aug-cc-pVDZ	CCSD(T)/aug-cc-pVTZ	CCSD(T)-F12b/CBS	Difference
N_2-N_2O				
$R_{(N1O1)}$	1.2017	1.1910	1.1862	-0.0048
$R_{(N1N2)}$	1.1487	1.1322	1.1273	-0.0049
$R_{(N3N4)}$	1.1206	1.1038	1.0988	-0.0050
$R_{(N1N3)}$	3.0935	3.0916	3.1085	0.0169
$A_{(N2N1N3)}$	94.31	94.86	95.19	0.33
$A_{(O1N1N3)}$	85.58	85.03	84.71	-0.32
$A_{(N4N3N1)}$	168.67	168.33	167.95	-0.38
N_2O				
$R_{(NO)}$	1.2018	1.1912	1.1863	-0.0049
$R_{(NN)}$	1.1491	1.1323	1.1276	-0.0050
N_2				
$R_{(NN)}$	1.1209	1.1040	1.0989	-0.0051

Figure 5.3 shows the structure of the N_2-N_2O complex calculated by Zheng *et al* at the CCSD(T) level of theory, utilising the aug-cc-pVDZ basis set with a set of mid bond functions. These mid bond functions are used to describe the weak interactions between the monomer units in the complex.

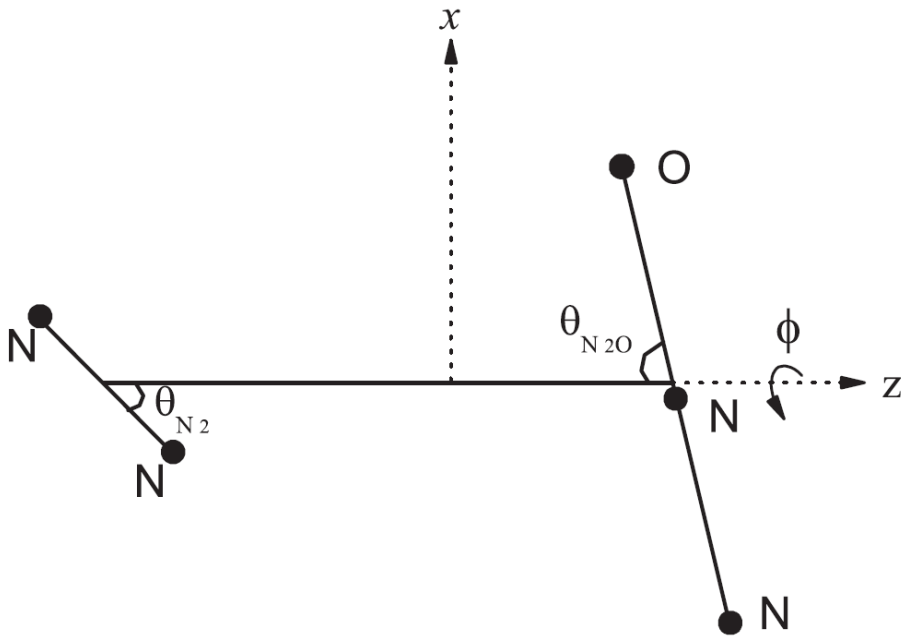

Figure 5.3: Structure of the N_2-N_2O complex from Zheng *et al*.[73]

Our calculated structure is generally in good agreement with that calculated by Zheng *et al*, except for the intermolecular distance. For this parameter Zheng *et al* used data from rotatationally resolved infrared spectroscopy and hence their value is actually a vibrationally averaged experimental result.

The difference between the equilibrium and ground state intermolecular distance of N_2-N_2O is calculated to be 0.079Å with the CCSD(T)/aug-cc-pVTZ method. If we add this to our "best estimate" equilibrium intermolecular distance from Table 5.3, we get a value of 3.190 Å.

5.3 - Vibrational modes of the N_2- N_2O complex

In Table 5.5 we present harmonic vibrational frequencies of N_2O, N_2 and the N_2-N_2O complex calculated with the CCSD(T)-F12a and CCSD(T)-F12b methods, and the cc-pVxZ-F12 basis sets. These results were obtained without counterpoise correction using the standard geometries from Tables 5.1 and 5.2. No vibrational intensities are presented as these cannot be calculated in MOLPRO due to the use of numerical energy derivatives.

The vibrational modes of the N_2-N_2O complex can be seen to vary only slightly between the CCSD(T)-F12a and CCSD(T)-F12b results. There is also little variation between the harmonic frequencies obtained with the different basis sets, indicating that the results are close to being converged to the CBS limit. The four lowest vibrational modes of N_2-N_2O represent the intermolecular vibrational modes. With the exception of the ν_2 mode with the cc-pVTZ-F12, these modes are calculated to be slightly smaller with the CCSD(T)-F12b method than the CCSD(T)-F12a method. Similar to the observation in the H_2O-N_2O chapter, the opposite trend is observed for the intramolecular vibrational modes with the CCSD(T)-F12b method generally calculating larger vibrational frequencies than the CCSD(T)-F12a method.

We see a relatively consistent increase in the degenerative modes from the N_2O monomer upon complexation by approximately 13 cm^{-1}. This mode is doubly-degenerate in the monomer but separates by up to 1 cm^{-1} in the complex.

The vibrational mode of the N_2 monomer changes a smaller amount upon complexation compared to the modes in the N_2O monomer. The N_2 monomer mode is reduced in wavenumber upon forming the complex by approximately 2 cm^{-1}. In comparison, the vibrational modes of N_2O monomer change by 1-25 cm^{-1} upon complexation. Interestingly, the N_2O monomer mode of approximately 1300 cm^{-1} is seen to decrease by approximately 1 cm^{-1} upon formation of the complex, whereas all the other monomer modes increase in magnitude upon formation of the complex.

Table 5.5: Harmonic vibrational frequencies (cm^{-1}) of N_2, N_2O and the N_2-N_2O complex calculated with the CCSD(T)-F12a and CCSD(T)-F12b methods and the cc-pVxZ-F12 (x=D,T,Q) basis set

	cc-pVDZ-F12		cc-pVTZ-F12		cc-pVQZ-F12	
	CCSD(T)-F12a	CCSD(T)-F12b	CCSD(T)-F12a	CCSD(T)-F12b	CCSD(T)-F12a	CCSD(T)-F12b
N_2-N_2O						
ν_1	26.6	26.6	26.5	26.4	26.9	25.9
ν_2	38.0	37.9	36.4	36.5	35.5	35.1
ν_3	61.6	60.3	61.2	60.8	61.4	61.3
ν_4	84.2	83.2	84.0	83.7	84.1	84.0
ν_5	594.9	596.1	599.0	599.2	600.2	600.3
ν_6	595.3	596.6	599.8	599.9	600.8	600.8
ν_7	1299.0	1302.1	1302.6	1303.9	1304.1	1304.7
ν_8	2284.5	2285.6	2289.3	2289.8	2291.5	2291.8
ν_9	2357.6	2361.5	2360.9	2362.3	2363.5	2364.2
N_2O						
ν_1	581.7	583.3	586.5	586.7	587.8	588.0
ν_2	581.8	583.3	586.6	586.7	587.8	588.0
ν_3	1300.4	1303.7	1304.6	1305.9	1306.2	1306.8
ν_4	2259.7	2260.3	2264.6	2265.1	2266.0	2266.3
N_2						
ν_1	2355.5	2359.2	2359.3	2360.6	2361.9	2362.5

In Table 5.6 we present the harmonic and anharmonic vibrational frequencies and intensities for N_2, N_2O and N_2-N_2O calculated with conventional CCSD(T) and the aug-cc-pV xZ basis sets (x=D, T). These results were obtained without counterpoise correction using the geometries from Table 5.4. The anharmonic results were calculated within the second order vibrational perturbation theory (VPT2) framework.

The harmonic frequencies calculated with conventional CCSD(T) and the aug-cc-pVDZ and aug-cc-pVTZ basis set are in general slightly smaller than those calculated with explicitly correlated CCSD(T)-F12b and the cc-pVDZ-F12 or cc-pVTZ-F12 basis set.

The harmonic intensities of the vibrational modes for both of the monomer species show a reasonable consistency between the aug-cc-pVDZ and aug-cc-pVTZ results, indicating that these are reasonably well converged with respect to the CBS limit.

As expected, in both of the monomers and for the complex, the anharmonic vibrational frequencies are calculated to be smaller than the respective harmonic mode. For the monomers, these calculated anharmonic frequencies are all sensible and are in reasonably good agreement with the experimental fundamental frequencies. The intramolecular vibrational frequencies also appear to be reasonable; however there is a larger relative change in some of the intermolecular vibrational modes.

The vibrational modes of the N_2O monomer are seen to only change by approximately 1 cm^{-1} upon formation of the complex. The intensities of the anharmonic modes in the complex follow the same trend observed in the intensities of the harmonic modes.

Table 5.6: Harmonic and anharmonic vibrational frequencies (cm^{-1}) and intensities (in km mol^{-1}) of N_2O, N_2 and the N_2-N_2O complex calculated with the CCSD(T) method

	aug-cc-pVDZ				aug-cc-pVTZ			
	Harmonic		Anharmonic		Harmonic		Anharmonic	
N_2-N_2O	Frequency	Intensity	Frequency	Intensity	Frequency	Intensity	Frequency	Intensity
ν_1	22.4	0.0	8.1	0.0	24.9	0.0	13.0	0.0
ν_2	34.1	0.0	15.9	0.0	37.3	0.0	31.3	0.0
ν_3	64.7	0.0	17.6	0.0	65.9	0.0	29.4	0.0
ν_4	83.1	0.1	51.6	0.0	84.2	0.1	55.5	0.0
ν_5	564.0	4.5	558.3	3.9	592.7	5.1	586.9	4.5
ν_6	566.1	2.8	558.8	2.6	593.9	3.4	586.4	3.1
ν_7	1278.2	54.5	1262.0	54.6	1288.3	56.7	1277.0	54.5
ν_8	2244.1	333.9	2183.9	298.3	2270.2	351.1	2211.0	314.6
ν_9	2320.6	0.0	2291.6	0.0	2341.4	0.0	2313.0	0.0
N_2								
ν_1	2318.8	0.0	2290	0.0	2339.6	0.0	2311.6	0.0
N_2O								
ν_1	567.1	3.0	559.7	2.5	593.2	3.7	587.1	3.4
ν_2	567.1	3.0	559.7	2.3	593.2	3.7	587.1	3.4
ν_3	1277.0	56.8	1261.0	57.7	1286.8	59.1	1275.8	57.4
ν_4	2240.8	359.3	2182.2	300.7	2266.5	377	2208.6	340.9

In Table 5.7 we present the calculated and experimental vibrational modes of the N_2-N_2O complex from Venayagamoorthy and Ford. We also show in Table 5.7 our best estimate vibrational modes of the N_2-N_2O complex, obtained by adding the difference between the CCSD(T/aug-cc-pVTZ harmonic and anharmonic frequencies to the CCSD(T)-F12b/cc-pVQZ-F12 values.

We show that the vibrational modes are less consistent between the experimental and our calculated values for the intermolecular modes, compared to the intramolecular modes. This may come about from the small size of these modes, so that changes appear larger in a relative sense. We see that our best estimate intramolecular frequencies for the N_2-N_2O complex are larger than those of Venayagamoorthy and Ford, whereas the opposite is seen for the intermolecular frequencies here. The two largest intramolecular frequencies of our best estimate modes show a better consistency with the experimental monomer modes than the respective modes in the complex.

Table 5.7: Vibrational modes of N_2, N_2O and N_2-N_2O from Venayagamoorthy and Ford[72] and our best estimate

Computed	Experimental	Computed	Experimental	Vibrational mode	Intensity	Best estimate modes
N_2[83]		N_2O[84]		N_2-N_2O		
2175.7	2359.6			2245.3	347.0	2335.8
		2243.2	2223.8	2176.5	0.0	2232.6
		1286.1	1284.9	1287.2	10.9	1293.4
		537.8	588.8	538.5	4.1	593.3
				83.5	0.2	55.3
				63.6	0.0	29.1
				29.0	0.0	14.0
				537.5	2.9	594.5
				69.5	0.0	24.8

5.4 - Interaction Energy of the N_2- N_2O complex

In Table 5.8 we present the interaction energy of the N_2-N_2O complex obtained with and without counterpoise correction. These interaction energies are calculated using the optimised geometry of the corresponding method from the respective structures shown in Tables 5.1-5.4.

We see that the interaction energy of the complex without counterpise correction becomes smaller in magnitude as the basis set size increases for the CCSD(T)-F12a method but increases in this trend for the CCSD(T)-F12b method. We see that for both the CCSD(T)-F12a and CCSD(T)-F12b methods, the calculations with the counterpoise correction have the interaction energy increase in magnitude as the basis set size increases.

In both of the CCSD(T)-F12a and CCSD(T)-F12b methods, the calculations without counterpoise correction gave a smaller energy value than the respective counterpoise corrected value. It is also observed that the CCSSD(T)-F12a data gives a larger interaction energy than the respective value with the CCSD(T)-F12b method.

We find that inclusion of core correlation reduces the interaction energy of the N_2-N_2O complex slightly, by 0.1 kJ mol^{-1}.

Table 5.8: CCSD(T)-F12a and CCSD(T)-F12b interaction energies (kJ mol^{-1}) of the N_2-N_2O complex obtained with and without counterpoise correction

	CCSD(T)-F12a		CCSD(T)-F12b	
	Standard	Counterpoise	Standard	Counterpoise
cc-pVDZ-F12	-4.14	-3.68	-3.99	-3.61
cc-pVTZ-F12	-4.04	-3.76	-4.01	-3.77
cc-pVQZ-F12	-4.02	-3.86	-4.02	-3.89
CBS			-3.96	
cc-pCVQZ-F12			-3.86	

In Table 5.9 we present our best estimate at the interaction energy of the N_2-N_2O complex. This is calculated by taking the CCSD(T)-F12b CBS limit interaction energy and adding a correction for core correlation and a correction for zero-point energy. The core correlation correction is obtained as the difference between the counterpoise corrected all electron CCSD(T)-F12b/cc-pCVQZ-F12 result and the counterpoise corrected frozen core CCSD(T)-F12b/cc-pVQZ-F12 result. The zero-point energy correction is obtained from the CCSD(T)-F12b/cc-pVQZ-F12 harmonic frequencies in Table 5.6.

Table 5.9: Best estimate of the interaction energy of the N_2-N_2O complex

	Energy (kJ mol^{-1})
CBS	-3.96
Core correction	-0.03
ZPVE correction	+1.50
Best estimate	**-2.49**

5.5 – Conclusion

We have optimized the structure of the N_2-N_2O complex and calculated its vibrational frequencies with both conventional CCSD(T) and explicitly correlated CCSD(T)-F12 methods. We find that the minimum energy structure is approximately T-shape, in agreement with previous expeirmental and theoretical investigations. Our best estimate of the interaction energy for N_2-N_2O is 2.49 kJ mol^{-1}, which is obtained at the CCSD(T)-F12b/CBS limit and includes a correction for core correlation and a correction for zero-point vibrational energy.

We show that the optimized structure of the N_2-N_2O complex closely matches the structure described by Zheng *et al*. This indicates that this structure does in fact represent the global minimum structure of the complex.

In chapter 7 we use our best estimate interaction energy and the CCSD(T)-F12b/cc-pVQZ-F12 harmonic frequencies to determine the equilibrium constants for formation of N_2-N_2O as a function of altitude.

6 - O_2-N_2O

6.1 - Introduction

Oxygen is the second most abundant molecule in Earth's atmosphere. Several complexes involving oxygen, such as the O_2-H_2O complex and the O_2-O_2 dimer, have been found to be atmospherically important.[74] Similar to the H_2O-N_2O complex, the O_2-N_2O complex will influence the radiative balance of atmospheric water, which contributes to the global warming potential of water.

The O_2-N_2O complex has been previously investigated both theoretically and experimentally. In Figure 6.1 we show the structure of the O_2-N_2O complex determined by Qian, Seccombe and Howard using rotationally resolved infrared spectroscopy.[82] The authors found that two different approximately T-shape structures of the complex fitted the experimental rotational constants equally well. The structure shown in Figure 6.1 was preferred as it was consistent with the global minimum structure obtained from MP2 calculations using a small basis set. However as we will show in this chapter, higher level coupled cluster calculations indicate that their alternative structure is more likely to be the global minimum.

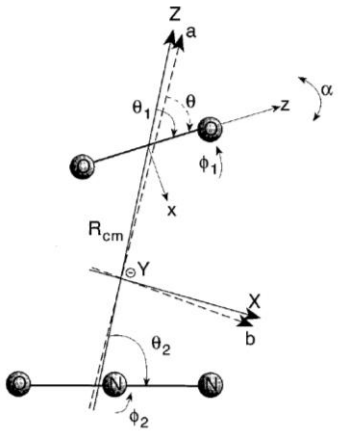

Figure 6.1: O_2-N_2O structure determined by Qian, Seccombe and Howard [84]

Figure 6.2 shows the geometric parameters that were used to define the O_2-N_2O complex in our investigation. Two different minima are considered, with the oxygen molecule either pointing away from the O-end of N_2O (global minimum) or from the N-end of N_2O (local minimum). The local minimum structure initially appeared to be a saddle-point, hence there is less data presented for this structure.

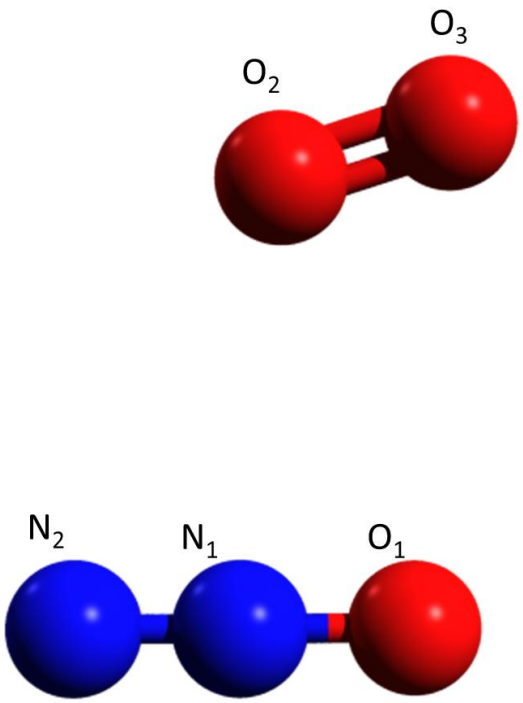

Figure 6.2: Geometric parameters used to define the structure of the O_2-N_2O complex

In this chapter we present results for the optimised structure, vibrational modes and binding energy of O_2-N_2O that we have conducted. We have investigated the structure of O_2-N_2O using both conventional and explicitly correlated coupled cluster methods, inclusive and exclusive of counterpoise (CP) correction. Difficulties were found in the characterization of the minima structure, which are discussed within, and is why this complex is presented last.

6.2 - Structure of the O_2-N_2O complex

In Figure 6.3 we plot the UCCSD(T)-F12b/cc-pVDZ-F12 energy of the O_2-N_2O complex as a function of the angles θ_1 (denoted A1) and θ_2 (denoted as A2) from Figure 6.1. The intermolecular distance is fixed at 3.4 Å and the intramolecular geometric parameters are fixed at the UCCSD(T)-F12b/cc-pVDZ-F12 optimized values for N_2O and O_2. A similar potential energy surface was generated with the MP2 method and 6-311G** basis set by Qian, Seccombe and Howard.

Two minima are evident on the potential energy surface. The local minimum occurs at $\theta_1=53^0$ and $\theta_2=83^0$ whereas the global minimum occurs at $\theta_1=121^0$ and $\theta_2=104^0$. Qian, Seccombe and Howard found that two sets of geometric parameters fitted the measured rotational constants equally well with either $\theta_1=58^0$ and $\theta_2=77^0$ or $\theta_1=122^0$ and $\theta_2=100^0$. Based on our present results, the former structure corresponds to a local minimum whereas the latter corresponds to the global minimum. However, characterization of these two minima was only completed at the very end of this thesis due to problems calculating reliable harmonic frequencies for each structure.

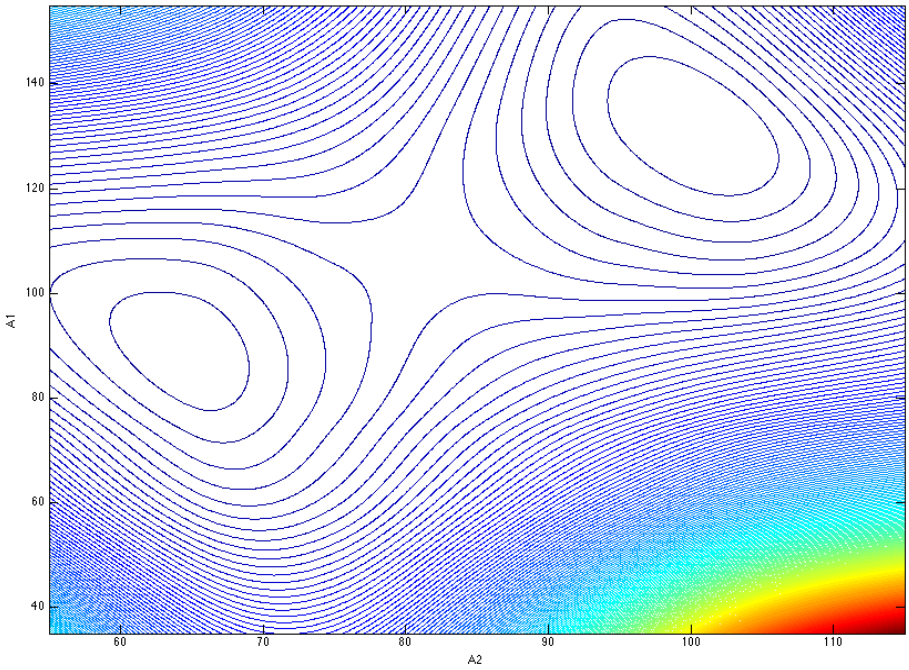

Figure 6.3: Contour map of the optimization of the O_2-N_2O complex

In Tables 6.1 and 6.2 we show the UCCSD(T)-F12b/cc-pVDZ-F12 calculated vibrational frequencies of the global minimum and local minimum respectively. These results were obtained using varying step-sizes for the calculation of the numerical Hessian. We show that using the default step-size in MOLPRO, gives at least one imaginary frequency for both structures, indicating that neither structure is a minimum. This result was a signficant source of confusion and substantially delayed progress with this chapter. When the step-size decreases, we observe significant changes in the lowest energy vibrational frequencies. At a step-size of 0.004 or smaller, we find that both structures are indeed minima with all positive frequencies.

It is worth noting that the same trend was not observed for conventional UCCSD(T) with the aug-cc-pVDZ basis set. In this case the vibrational frequencies were all positive for the full range of step-sizes considered. This may be due to BSSE, which causes the intermolecular potential energy surface to be artifically less flat.

Table 6.1: UCCSD(T)-F12b/cc-pVDZ-F12 vibrational frequencies for the global minimum of O_2-N_2O with various step sizes used fot the numerical Hessian

	Step-size for numerical Hessian (a.u.)							
	0.001	0.002	0.003	0.004	0.005	0.006	0.008	0.010 (default)
ν_1	30.4	25.1	24.1	20.6	-15.3	-34.8	-68.3	-111.1
ν_2	39.7	34.1	29.4	23.7	23.6	23.5	23.4	-27.6
ν_3	50.5	47	45.6	44.1	42.1	39.3	28.5	23.4
ν_4	73.9	72.1	71.6	71.5	72	73.1	78.8	91.8
ν_5	596.1	595.8	595.8	595.7	595.7	595.7	595.7	595.7
ν_6	596.5	596.2	596.1	596.1	596	596	596	595.9
ν_7	1300.8	1300.7	1300.7	1300.7	1300.7	1300.7	1300.7	1300.7
ν_8	1614.2	1614.3	1614.5	1614.8	1615.2	1615.7	1617.5	1620.7
ν_9	2283.4	2283.4	2283.4	2283.4	2283.4	2283.4	2283.4	2283.5

Table 6.2: UCCSD(T)-F12b/cc-pVDZ-F12 vibrational frequencies for the local minimum of O_2-N_2O with various step sizes used for the numerical Hessian

	Step-size for numerical Hessian (a.u)							
	0.001	0.002	0.003	0.004	0.005	0.006	0.008	0.010 (default)
ν_1	25.8	19.8	18.2	10.0	-15.5	-25.5	-46.0	-72.5
ν_2	33.6	23.8	24.1	24.0	23.0	23.6	23.3	23.1
ν_3	49.4	46.0	47.1	47.5	47.8	49.2	50.2	36.4
ν_4	70.2	66.8	66.0	64.5	62.3	60.1	55.1	60.1
ν_5	597.1	596.2	596.3	596.3	596.3	596.3	596.3	596.3
ν_6	597.4	596.8	596.8	596.8	596.7	596.8	596.7	596.7
ν_7	1302.2	1302.1	1302.1	1302.1	1302.1	1302.1	1302.1	1302.1
ν_8	1606.6	1606.5	1606.6	1606.7	1606.9	1607.2	1608.1	1609.5
ν_9	2283.3	2283.2	2283.2	2283.2	2283.2	2283.2	2283.2	2283.3

In Table 6.3 we present the UCCSD(T)-F12b optimised geometric parameters of the global minimum O_2-N_2O structure, obtained using the cc-pVxZ-F12 basis sets, (x=D,T,Q), including and excluding a counterpoise correction. We find that there is very small change in the intramolecular bond lengths when the counterpoise correction is applied,which closely matches the trends observed in the calculations of the complexes in the previous chapters.

Similar to the observation in previous chapters, the bond lengths in the N_2O unit show negligible change in the parameters upon. However, the OO bond from the O_2 unit is seen to decrease by approximately 0.01Å upon formation of the complex, which shows a not unsubstantial change in contrast to the general approach of fixed intramolecular bond lengths upon complexation.

Table 6.3: The UCCSD(T)-F12b optimised structure of O_2, N_2O and the global minimum O_2-N_2O complex obtained with and without counterpoise correction

	cc-pVDZ-F12			cc-pVTZ-F12			cc-pVQZ-F12			CBS
O_2-N_2O	Standard	Counterpoise	Difference	Standard	Counterpoise	Difference	Standard	Counterpoise	Difference	
$R_{(N2N1)}$	1.1286	1.1286	0.0000	1.1280	1.1279	-0.0001	1.1275	1.1275	0.0000	1.1275
$R_{(O1N1)}$	1.1876	1.1876	0.0000	1.1869	1.1869	0.0000	1.1865	1.1865	0.0000	1.1864
$R_{(O2O3)}$	1.2077	1.2076	-0.0001	1.2068	1.2068	0.0000	1.2062	1.2062	0.0000	1.2062
$R_{(O2N1)}$	3.0740	3.0994	0.0254	3.0658	3.0806	0.0148	3.0601	3.0689	0.0088	3.0627
$A_{(N2N1O2)}$	95.75	95.74	-0.01	95.28	95.22	-0.06	95.27	95.09	-0.18	95.02
$A_{(O3O2N1)}$	112.54	112.63	0.09	113.21	113.63	0.42	114.26	114.64	0.38	114.85
$A_{(N2N1O1)}$	179.83	179.85	0.02	179.84	179.85	0.01	179.85	179.85	0.00	179.85
N_2O										
$R_{(NO)}$	1.1874			1.1868			1.1864			
$R_{(NN)}$	1.1287			1.1281			1.1277			
O_2										
$R_{(OO)}$	1.2188			1.2183			1.2177			

We present the geometric parameters for the secondary structure of the O_2-N_2O complex in Appendix A.5. This structure represents the preferred experimental structure shown in Figure 6.1. The interaction energy of this local minimum structure, discussed later, is slightly smaller than that of the global minimum.

We have optimised the geometries of O_2, N_2O and the O_2-N_2O complex with all electrons correlated, to assess the impact of freezing the core electrons. In Table 6.4 we present the UCCSD(T)-F12b optimised geometric parameters of O_2, N_2O and the global minimum structure of O_2-N_2O obtained with the cc-pVQZ-F12 basis set utilising the frozen core approximation and with the cc-pCVQZ-F12 basis set correlating all electrons. The difference between these two calculations is used as an estimate of the effect of core correlation.

We find that the inclusion of core correlation reduces the intramolecular bond lengths by approximately 0.002Å, but increases the intermolecular bond length to a smaller magnitude. It also has an appreciable but non-systematic effect on the bond angles.

Also shown in Table 6.4 is our best estimate of the geometric parameters of the O_2-N_2O complex. This structure is obtained by adding the difference between the all electron cc-pCVQZ-F12 optimization and frozen core cc-pVQZ-F12 optimization to the CBS limit structure.

Table 6.4: **:** All electron and frozen core counterpoise corrected optimised geometric parameters of O_2, N_2O and the global minimum O_2-N_2O complex obtained with the UCCSD(T)-F12b method

	cc-pVQZ-F12	cc-pCVQZ-F12	Difference	UCCSD(T)-F12b/CBS	Best estimate
O_2-N_2O					
$R_{(N2N1)}$	1.1275	1.1253	-0.0022	1.1275	1.1253
$R_{(O1N1)}$	1.1865	1.1843	-0.0022	1.1864	1.1842
$R_{(O2O3)}$	1.2062	1.2042	-0.0020	1.2062	1.2042
$R_{(O2N1)}$	3.0601	3.0645	0.0044	3.0627	3.0671
$A_{2(N2N1O2)}$	95.09	95.07	-0.02	95.02	95.00
$A_{(O3O2N1)}$	114.26	115.64	1.38	114.85	116.23
$A_{(N2N1O1)}$	179.85	179.85	0.00	179.85	179.85
N_2O					
$R_{(NO)}$	1.1864	1.1842	-0.0022	1.1863	1.1841
$R_{(NN)}$	1.1277	1.1254	-0.0022	1.1276	1.1254
O_2					
$R_{(OO)}$	1.2177	1.2156	-0.0021	1.2178	1.2179

In Table 6.5 we present the optimized geometric parameters of the global minimum O_2-N_2O structure obtained with conventional UCCSD(T) and the aug-cc-pVDZ basis set, and at the UCCSD(T)-F12b/CBS limit.

We see a reasonable consistency between the UCCSD(T)/aug-cc-pVDZ and UCCSD(T)-F12b/CBS calculations, especially in the intramolecular bond lengths. The largest variation appears to come from the the intermolecular angle $A_{(O3O2N1)}$, with a not unsubstantial difference in the intermolecular bond length. This would be expcted to be larger due to this bond being approximately three times as large as the intramolecular bond lengths.

Table 6.5: The structure of O_2, N_2O and the global minimum O_2-N_2O complex optimised with conventional UCCSD(T) and at the explicitly correlated UCCSD(T)-F12b/CBS limit

	UCCSD(T)/aug-cc-pVDZ	UCCSD(T)-F12b/CBS	Difference
O_2-N_2O			
$R_{(N2N1)}$	1.1280	1.1275	-0.0005
$R_{(O1N1)}$	1.1864	1.1864	0.0000
$R_{(O2O3)}$	1.2072	1.2062	-0.0010
$R_{(O2N1)}$	3.0151	3.0627	0.0476
$A_{2(N2N1O2)}$	95.86	95.02	-0.84
$A_{(O3O2N1)}$	109.88	114.85	4.97
$A_{(N2N1O1)}$	179.75	179.85	0.10
N_2O			
$R_{(NO)}$	1.2018	1.1863	-0.0049
$R_{(NN)}$	1.1491	1.1276	-0.0050
O_2			
$R_{(OO)}$	1.2188	1.2183	-0.0005

The two sets of geometric parameters reported by Qian, Seccombe and Howard are shown in Table 6.6. We find that our global minimum structure is in good agreement with the second set of experimental parameters of Qian, Seccombe and Howard. Our local minimum structure is also in reasonable agreement with the preferred experimental parameters.

Conversion of our best estimate structure into a centre of mass equivalent produces a calculated distance between the centres of mass of 3.2918 Å. This is seen to be slightly smaller than the distance presented in experiment which is to be expected as our best estimate structure is determined as an equilibrium bond length, which doesn't take into account

anharmonic effects on the bond length, whereas the experimental structure is obtained as a vibrationally averaged structure.

Table 6.6: Parameters of the global and local minimum O_2-N_2O structures from Qian, Seccombe and Howard [75]

Parameter	Global minimum	Local mimimum
R_{cms}	3.432Å	3.432Å
A_{O2}	122^0	58^0
A_{N2O}	100^0	77^0

6.3 - Vibrational modes of the N_2O- O_2 complex

In Table 6.7 we present harmonic vibrational frequencies of N_2O, O_2 and our global minimum O_2-N_2O complex calculated with the UCCSD(T)-F12b method, with the cc-pVxZ-F12 basis sets,(x=D,T). These results were obtained without counterpoise correction using the standard geometries from Table 6.2. This uses the numerical hessian value of 0.004 for the step size.

With the exception of the ν_3 and ν_8 modes of the complex, each mode is larger with the cc-pVTZ-F12 basis set than the cc-pVDZ-F12 value. The ν_3 and ν_8 modes are seen to be slightly smaller in the cc-pVTZ-F12 data than in the cc-pVTZ-F12 data, but there appears no overall observable trend for the degree to which the modes change.

Similar to the observation for the previous complexes, the two degenerative modes and the largest mode from the N_2O monomer are seen to increase upon forming the complex. The ν_3 mode here is seen to decrease due to complexation. The magnitude of the change in the modes upon complex formation appears consistent between the cc-pVDZ-F12 and cc-pVTZ-F12 basis sets. The O_2 stretching vibrational mode is found to increase by approximately 10 cm^{-1} upon complexation, which is consistent with te decrease in the O_2 bondlength.

Table 6.7: Harmonic vibrational frequencies (cm^{-1}) of O_2, N_2O and the global minimum O_2-N_2O complex calculated with the UCCSD(T)-F12b method and the cc-pVxZ-F12 (x=D,T) basis set

	cc-pVDZ-F12	cc-pVTZ-F12
O_2-N_2O		
ν_1	20.1	21.2
ν_2	23.2	26.9
ν_3	43.8	45.7
ν_4	71.4	69.8
ν_5	595.7	599.0
ν_6	596.1	599.0
ν_7	1300.7	1302.5
ν_8	1614.8	1612.9
ν_9	2283.4	2287.5
N_2O		
ν_1	583.3	586.7
ν_2	583.3	586.7
ν_3	1303.7	1305.9
ν_4	2260.3	2265.1
O_2		
ν_1	1601.8	1603.5

6.4 – Interaction energy of the N_2O- O_2 complex

In Table 6.8 we present the interaction energy of both the global minimum and local minimum structures of the O_2-N_2O complex obtained with and without counterpoise correction. These interaction energies are calculated using the optimised geometry of the corresponding method. We also show the core correlation and complete basis set extrapolated value for the global minimum.

We show that as the basis set size increases, the interaction energy value for the complex increases in the calculations without the counterpoise correction, whereas the value decreases in magnitude in the counterpoise corrected UCCSD(T)-F12b calculations. We observed in the previous chapters that the calculated value without counterpoise correction is larger than that of the equivalent counterpoise corrected value. This also occurs for all of the basis sets for the O_2-N_2O complex.

Table 6.8: UCCSD(T)-F12b interaction energies (kJ mol^{-1}) of the O_2-N_2O complex obtained with and without counterpoise correction

	Global minimum		Local minimum	
	Standard	Counterpoise	Standard	Counterpoise
cc-pVDZ-F12	-3.38	-2.93	-3.03	-2.60
cc-pVTZ-F12	-3.32	-3.01	-3.03	-2.73
cc-pVQZ-F12	-3.23	-3.02		
cc-pCVQZ-F12	-2.94			
CBS	-3.05			

In Table 6.9 we present our best estimate at the interaction energy of the O_2-N_2O complex. This is calculated by taking the UCCSD(T)-F12b CBS limit interaction energy and adding a correction for core correlation and a correction for zero-point energy. The core correlation correction is obtained as the difference between the counterpoise corrected all electron UCCSD(T)-F12b/cc-pCVQZ-F12 result and the counterpoise corrected frozen core UCCSD(T)-F12b/cc-pVQZ-F12 result. The zero-point energy correction is obtained from the UCCSD(T)-F12b/cc-pVTZ-F12 harmonic frequencies in Table 6.7.

Table 6.9: Best estimate of the interaction energy of the global minimum O_2-N_2O complex

	Energy (kJ mol^{-1})
CBS	-3.05
Core correction	-0.08
ZPVE correction	+1.74
Best estimate	**-1.39**

6.5: Conclusion

We have presented the structure of the T-shaped O_2-N_2O complex, which we have determined to have a best estimate of the interaction energy of -1.39 kJ mol^{-1} for the global minimum structure. It was determined that two structures match the T-shape structure, both of which were reported by Qian, Seccombe and Howard, and that it is the structure that they did not prefer that we have determined to represent the global minimum structure. The structure prefered by Qian, Seccombe and Howard is found to have a smaller interaction energy and is therefore a local minimum instead. We experienced significant difficulty in characterizing both the local and global minimum structures due to problems with the numerical Hessian. We found that reliable vibrational frequencies could only be obtained when the step-size used for the numerical Hessian was reduced from the default value of 0.010 a.u. to 0.004 a.u. or smaller.

In chapter 7 we use our best estimate interaction energy and the UCCSD(T)-F12b/cc-pVTZ-F12 harmonic frequencies to determine the equilibrium constants for formation of the global minimum O_2-N_2O stucture as a function of altitude.

7 - Abundance of N_2O complexes in Earth's atmosphere

In this chapter we conclude the results of this thesis using the calculated information from chapters 3-6 to determine an estimation of the atmospheric concentration profile of our investigated complexes in the Earth's atmosphere. This is produced using statistical thermodynamic parameters and the effect of altitude on these parameters is investigated within this chapter. We also use the final section of this chapter to propose some recommendations of further research that should be considered for this work.

7.1 - Structure of Earth's atmosphere

The major constituents of Earth's atmosphere are N_2 at 78.08%, O_2 at 20.95% and Ar at 0.934% in a dry atmosphere. Along with H_2O at around 0.4% of the total atmosphere, these gases are the four whose complexes with N_2O are studied in this work.[22]

As shown in Figure 7.1, Earth's atmosphere is separated into distinct regions, which are defined by temperature inversion points. The lowest region is the troposphere, which extends from 0-15 km altitude and is characterised by a reduction in temperature with increasing altitude. There is a short region called the Tropopause where there is no change in the temperature. This is followed by the stratosphere in the 20-47 km region, in which there is an increase in atmospheric temperature with altitude. There is also a short region after this called the stratopause, where the temperature remains constant in the 47 and 52 km range. After this is the Mesosphere between 52 and 80 km. This region is characterised by a decrease in temperature with altitude down to 187 K, which represents the minimum temperature observed in the atmosphere. The Mesopause extends from 80 to 90 km altitude range and maintains this minimum temperature. Above 90 km is the Thermosphere region, which again has an increase in temperature with altitude. The temperature profile of the atmosphere is dependent on the incoming solar flux, which is influenced by the presence of the atmospheric gases providing both absorbtion and reflection interactions with the incoming photons. [22]

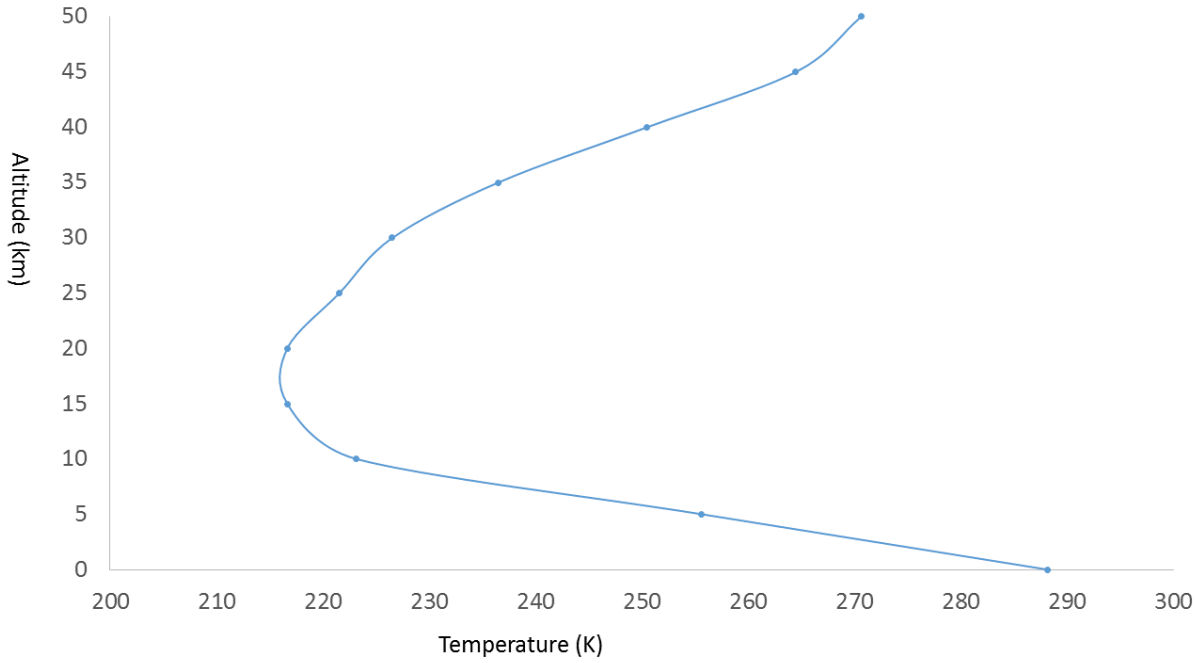

Figure 7.1: Temperature profile of the atmosphere [76]

7.2 - Atmospheric complexes

Complexes in Earth's atmosphere are responsible for changes to the absorption spectra compared to monomers, as well as producing different chemical reactivity and, as previously indicated, photodisociation dynamics. For example, the water dimer complex (H_2O-H_2O) is estimated to increase the absorbtion of radiation between 0.3 and 0.7 W m^{-2} over that of the monomer unit. [78] A second example involves the reaction of SO_3 with H_2O to form H_2SO_4, which is important for formation of cloud droplets. The involvement of a second water molecule to form the SO_3-$(H_2O)_2$ complex, lowers the barrier for reaction by 2.9 kJ mol^{-1}, catalysing the reaction. This result is consistent with the observation of a second order dependence with respect to the water pressure, for formation of H_2SO_4.[78]

Figure 7.2 shows the estimated concentration profiles of the H_2O-H_2O, O_2-H_2O and O_3-H_2O complexes in Earth's atmosphere.[74] These three profiles show a distinct inflection point around 20 km, which is primarily due to the concentration profile of H_2O monomer. As expected, this is most evident in the water dimer profile.

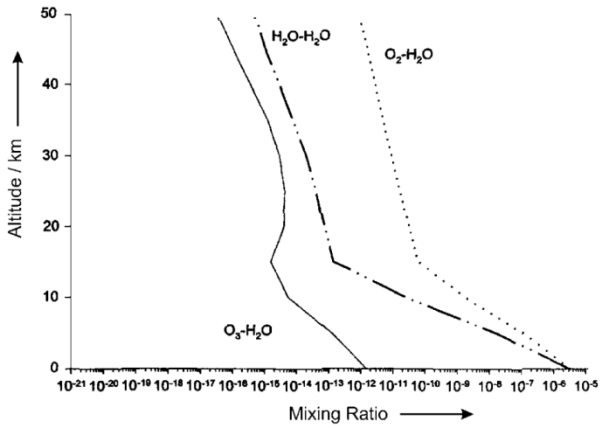

Figure 7.2: Concentration profiles of atmospheric H_2O containing complexes

Vaida and Hendick have also investigated the atmospheric abundances of a selection of hydrated complexes including the three shown in Figure 7.2 They found that the abundance of a complex was primarily controlled by monomer concentrations, temperature and dimer binding energies. Some complexes, such as H_2O-H_2O and HNO_3-H_2O are bound by substantial intermolecular hydrogen bonding so these have much larger binding energies than those bound by weak van der Waal interactions, such as the interaction in the H_2O-O_2 complex.[54]

The relatively high atmospheric temperatures in the range of 200 – 300 K threaten the stability of weakly bound neutral molecular complexes, making their characterisation somewhat difficult, and it is not known whether they are stable species with a substantial lifetime or if they are better described as short lived collision complexes.[54] Most experimental investigations utilize very cold conditions, such as those obtained from supersonic jet expanision, although complexes can also be formed under ambient thermal conditions.[79]

7.3 - Photodissociation of N_2O complexes

As discussed in Section 1.3, N_2O is primarily removed from Earth's atmosphere by a photodisociation process that involves absorption of UV light between 180 – 230 nm. The absorption band responsible for this photodissociation process is very weak as the transition between the linear $X'\Sigma^+$ ground state and bent $2'A'$ ($'\Delta$) excited state is forbidden. It follows

that change to the degenerate vibrational bending mode has a strong impact on the absorption cross-section.[45,80] As seen in Chapters 3-6, formation of the H_2O-N_2O, Ar-N_2O, N_2-N_2O and O_2-N_2O complexes causes small changes in the vibrational modes of N_2O. The degenerate N_2O bending modes shift to slightly larger frequency and split to be non-degenerate, with the largest frequency in the N_2O monomer also increasing upon complexation. The second largest frequency in the N_2O monomer decreases upon formation of the complex. These observations are observed for all four complexes.

The previous investigations of the complexes dealt more with the optimisation of the structure, and used the general approach of fixed geometric intramolecular geometric parameters of the monomers upon complexation. This is a reasonable concept, and we have shown in chapters 3-6 that in general, there are only small changes in geometric parameters of N_2O upon complexation. The only considerable change in the bond lengths is seen in the formation of the H_2O-N_2O complex, where there is a shifting of the electron density towards the terminal nitrogen, which is shown by the NN bond length decreasing upon formation of the complex, with an increase in NO bond length in this process. There has not been a complete investigation of the vibrational modes of the complexes that we have investigated using either experimental investigations or computational methods. There has yet to be an investigation to estimate the effect that complexation has on the absorption cross sectional area of the N_2O molecule, and how this affects the rate of photodisociation.

7.4 - Statistical thermodynamics

Below we describe the approach of Vaida and Headrick that can be used to estimate the abundance of a weakly bound complex.[54] The formation of a weakly bound complex involving N_2O can be written as

$$X + N_2O \rightarrow X - N_2O \tag{7-1}$$

With the corresponding equilibrium

$$K_c = \frac{[X-N_2O]}{[X][N_2O]} \tag{7-2}$$

It follows that if the Gibbs free energy for formation of a constant is known, the equilibrium constant can be calculated using

$$Kc = Exp(\frac{-\Delta G}{RT}) \quad (7\text{-}3)$$

The Gibbs free energy of formation for the complexes can be calculated using the standard statistical mechanics equations,[81] with input data for the zero-point vibrational energy corrected interaction energies (E_{ZPVE}), harmonic frequencies, rotational constants and masses obtained from the results in Chapters 3-6.

$$\Delta G = E_{ZPVE} + \Delta H + \Delta S \quad (7\text{-}4)$$

Enthalpy is defined as the sum of internal energy (U) and PV work

$$H = U + RT \quad (7\text{-}5)$$

The electronic, vibrational, rotational and translational contributions to U are given by

$$U = U_{elec} + U_{vib} + U_{trans} + U_{rot} \quad (7\text{-}6)$$

$$U_{elec} = E_j * R_e \quad (7\text{-}7)$$

$$U_{vib} = Nhcv_i \, , i = 1,2,3 \ldots, \quad (7\text{-}8)$$

$$U_{rot} = \frac{3}{2}RT \quad (7\text{-}9)$$

$$U_{trans} = \frac{3}{2}RT \quad (7\text{-}10)$$

The corresponding entropic contributions are given by

$$S_{total} = S_E + S_V + S_R + S_T \quad (7\text{-}11)$$

$$S_E = R\, lng_0 \quad (7\text{-}12)$$

$$(S_V)_{total} = \sum_{i-1}^{3N-6}(S_V)_i \quad (7\text{-}13)$$

$$S_V = R\left[\frac{hcv}{kT}\frac{1}{e^{\frac{hcv}{kT}-1}} - ln\left(1 - e^{\frac{hcv}{kT}}\right)^{-}\right] \quad (7\text{-}14)$$

$$(S_R)_{linear} = Rln\left(\frac{kTe^1}{\sigma\tilde{B}_A hc}\right) \quad (7\text{-}15)$$

$$(S_R)_{non\ linear} = Rln\left[\left(\frac{k^3T^3}{\tilde{B}_A\tilde{B}_B\tilde{B}_C h^3c^3}\right)^{\frac{1}{2}}\left(\frac{\pi^{\frac{1}{2}}e^{\frac{3}{2}}}{\sigma}\right)\right] \quad (7\text{-}16)$$

$$S_T = Rln\left[\left(\frac{2\pi mkT}{h^2}\right)^{\frac{3}{2}}\left(\frac{e^{\frac{5}{2}}kT}{P}\right)\right] \quad (7\text{-}17)$$

7.5 – Thermochemical results

An Excel spreadsheet was constructed to calculate the enthalpy, entropy, and Gibbs free energy of formation for the X-N_2O complexes as a function of altitude. The corresponding atmospheric temperatures at these altitudes was obtained from the US Standard Atmosphere.[35] The calculations of the H_2O-N_2O, Ar -N_2O, N_2-N_2O and O_2-N_2O complexes use the interaction energy and rotational constants obtained using the CBS limit values, with this interaction energy having a core correlation correction, along with the vibrational frequencies obtained at the highest available level. The H_2O-N_2O, Ar -N_2O and N_2-N_2O complexes use the CCSD(T)-F12b/cc-pVQZ-F12b calculated frequencies. The O_2-N_2O complex uses the UCCSD(T)-F12b method with the cc-pVTZ-F12 basis set. For the other complexes we find only small differences between the cc-pVTZ-F12 and cc-pVQZ-F12 harmonic frequencies so this is not expected to significantly reduce the accuracy.

In Figure 7.3 we show the enthalpy change associated with formation of the N_2-N_2O, O_2-N_2O, Ar-N_2O and H_2O-N_2O complexes as a function of altitude. The corresponding tabulated data is shown in Appendix A.7. The enthalpy values are seen to be reasonably consistent with the change in altitude, so are largely independent of the temperature profile of the atmosphere. The H_2O-N_2O complex has a much larger calculated enthalpy value than that of the other complexes, followed by N_2-N_2O, then Ar-N_2O, with the O_2-N_2O complex having the smallest calculated enthalpy value at all of the investigated altitudes.

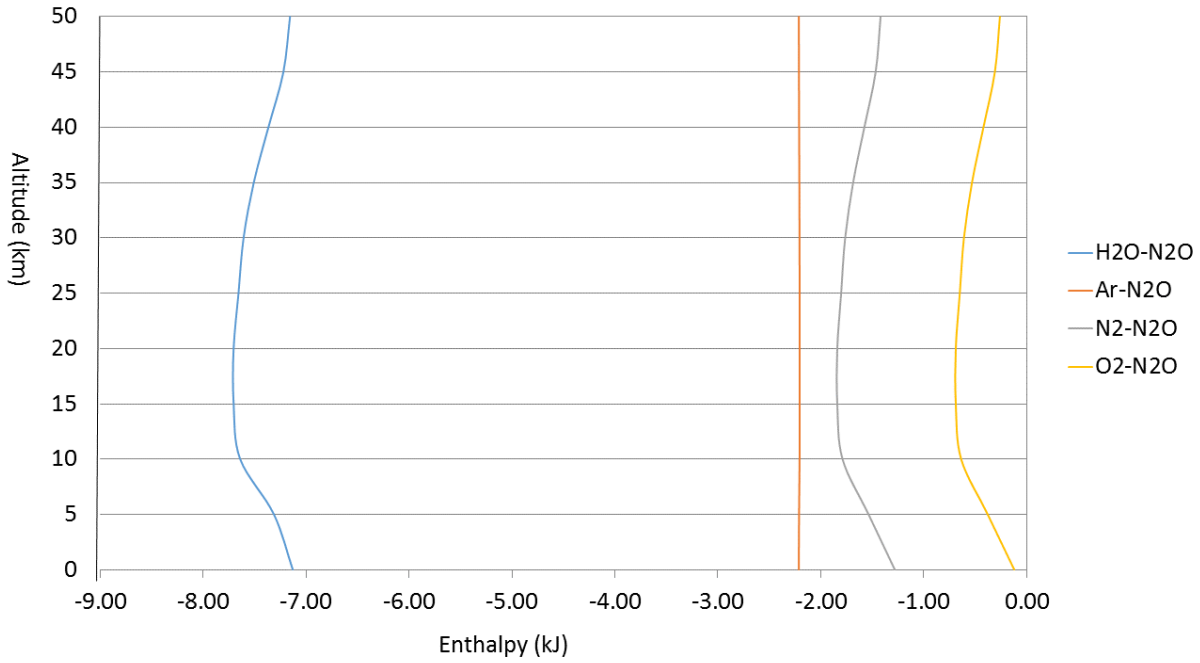

Figure 7.3: Effect of altitude on enthalpy of the complexes

In Figure 7.4 we show the entropy change associated with formation of the N_2-N_2O, O_2-N_2O, Ar-N_2O and H_2O-N_2O complexes as a function of altitude. The corresponding tabulated data is shown in the appendix in Table A.8. These are presented in the form of $T\Delta S$. This shows that the H_2O-N_2O complex gives the largest magnitude for the $T\Delta S$ term at all altitudes, followed by N_2-N_2O, then Ar-N_2O, and finally O_2-N_2O. These last three complexes are close to each other, but have distinct, non-crossing profile in the altitude range that we investigate.

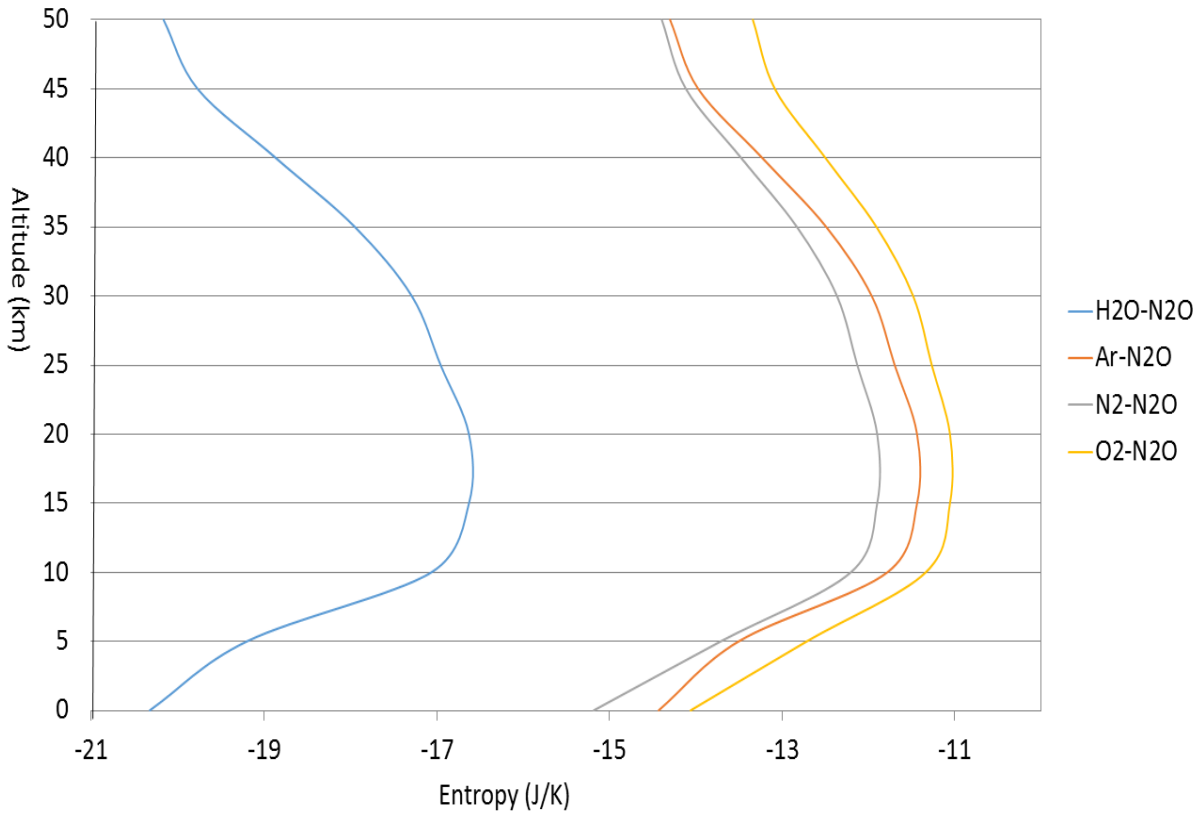

Figure 7.4: Effect of altitude on entropy of the complexes

In Figure 7.5 we show the change in Gibbs free energy associated with formation of the N_2-N_2O, O_2-N_2O, Ar-N_2O and H_2O-N_2O complexes as a function of altitude. The corresponding tabulated data is shown in the appendix in Table A.9. The inflection seen in the entropy plots in Figure 7.4 are increased in amplitude when the Gibbs free energy values are calculated. There is some crossing in the profiles, but generally the O_2-N_2O complex has the most positive calculated Gibbs free energy values. The overall Gibbs free energy trend for all of the complexes follows the same trend as the entropy contribution, where it is inversely proportional due to the subtraction of the $T\Delta S$ term when the Gibbs free energy is calculated.

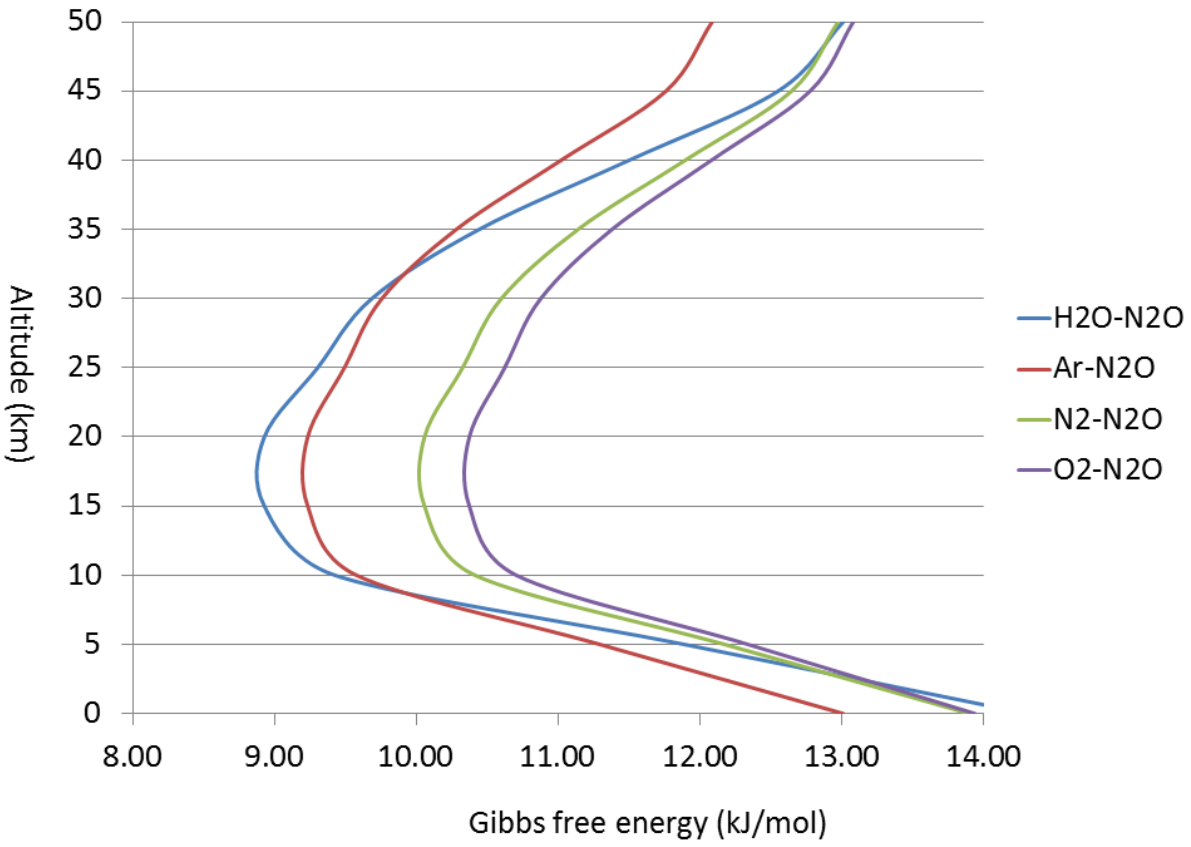

Figure 7.5: Effect of altitude on Gibbs free energy of the complexes

In Figure 7.6 we show the equilibrium constant associated with formation of the N_2-N_2O, O_2-N_2O, Ar-N_2O and H_2O-N_2O complexes as a function of altitude. We find that the equilibrium constants all increase as the alitide increases from 0-15 km. Above 20 km the equilibrium constant decreases again. The corresponding tabulated data is shown in the appendix in Table A.6. We see that the Ar-N_2O complex has the largest equilibrium constant at the 0, 5 and in the 35-50 km range, whereas the H_2O-N_2O complex has the largest value in the 10-30 km range. The N_2-N_2O complex shows a consistently larger equilibrium constant than is calculated for the O_2-N_2O complex at all altitudes.

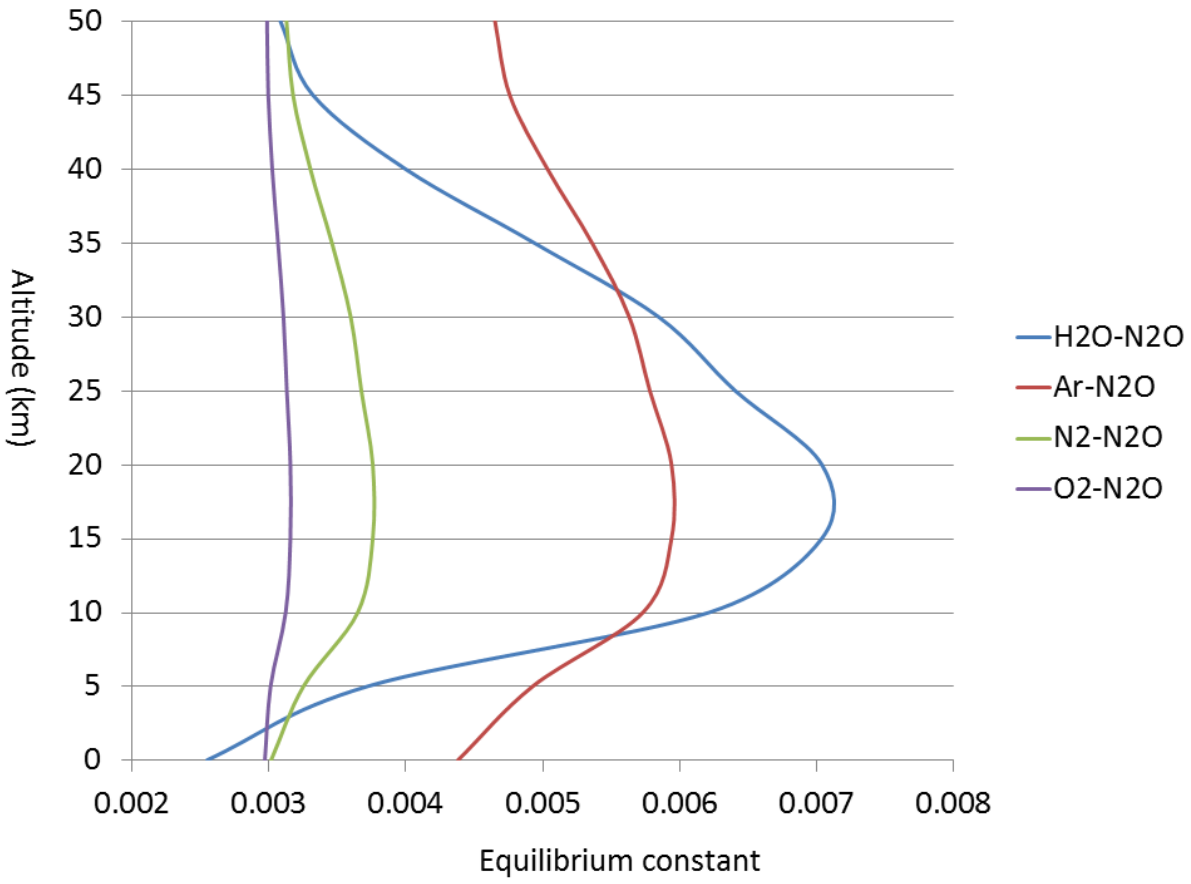

Figure 7.6: Change in equilibrium constant of our investigated structures with altitude

7.6 - Abundances

In Figure 7.7 we present the calculated abundances of our investigated complexes, using the equilibrium constants from Figure 7.6 and the concentrations of the monomers. The raw data for all of the monomers are presented in the appendix in Table A.10. The Argon data was obtained by Pidwirny[82], with all other monomer concentrations obtained from Anderson *et al.*[35] The raw data for the abundances are shown in the appendix in Table A.11.

We present abundances for the complexes from 0 to 50 km altitude as this is where photodisociation of N_2O is of primary importance. These calculations indicate that the N_2-N_2O complex has the largest calculated abundances of the complexes. This indicates that despite the low equilibrium constant of the N_2-N_2O complex, the large concentration of N_2, leads to this complex having the largest calculated concentration. In a similar manner, the

second most abundant component of the atmosphere, O_2, leads to the O_2-N_2O complex having the second most abundant calculated values. We also indicate that the Ar-N_2O complex gives larger concentration values than the respective H_2O-N_2O complex concentration when compared at the same altitude. The overall calculations show that even though the H_2O-N_2O complex has the largest value for the equilibrium constant in the 10-25 km range, as indicated earlier, it has the smallest calculated concentration. This is also in spite of this complex having the largest interaction energy. The sharp change in the profile of the H_2O monomer in the 10-15 km region is produced by the sharp change in the H_2O concentration, due to the sharp reduction in its concentration in the first 15 km of the atmosphere. The other complexes generally follow the concentration profile of the N_2O monomer due in part to the constant concentration of the other monomers with altitude.

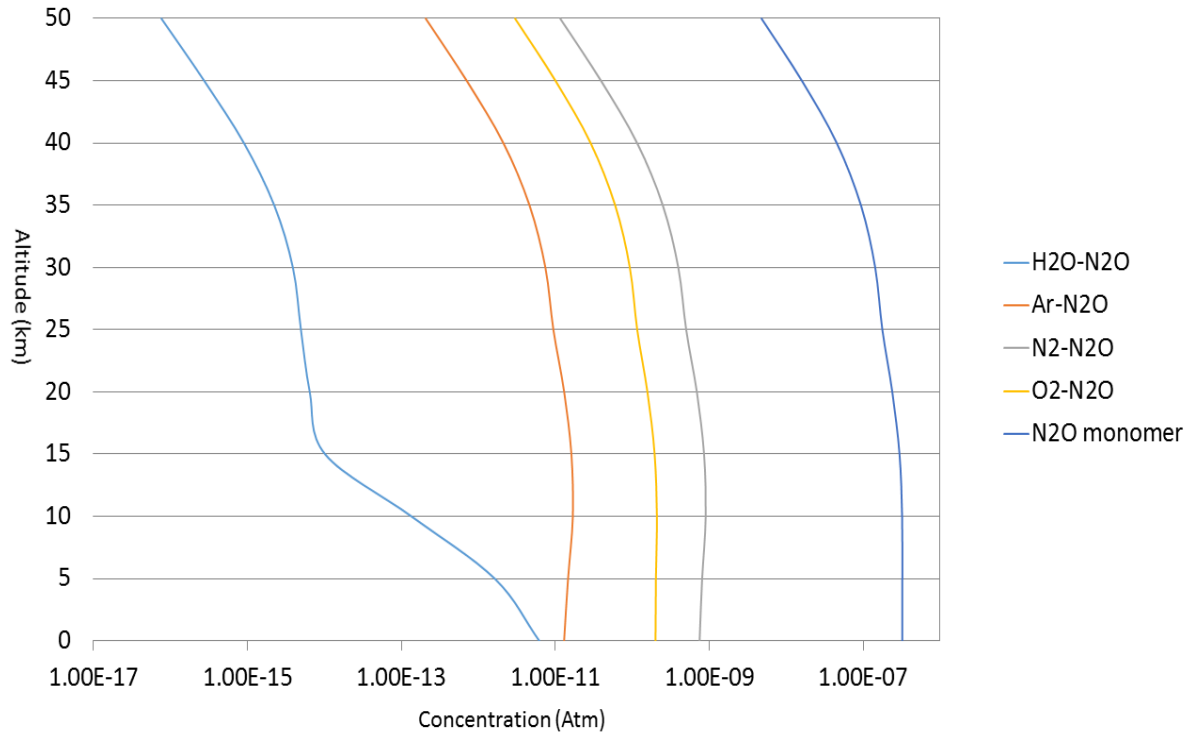

Figure 7.7: Calculated complex abundances in the 0 - 50 km altitude range

In the above calculations, we only consider the global minimum structure of the O_2-N_2O complex. The discovery of the higher energy local minimum for O_2-N_2O occurred very late, when this thesis was in its final stages of preparation. Nonetheless, for comparative purposes we have calculated the atmospheric abundance of the local and global minima of O_2-N_2O at a

single altitude of 50 km. As shown in appendix Table A.12, the abundance of both the local and global minimum structures of O_2-N_2O is appreciably dependent on the step-size used to calculate the numerical Hessian. This effect is primarily due to changes in the lowest frequency vibrational modes, which significantly impacts on the contribution to entropy. With a step-size of 0.003 a.u. we find that the local minimum structure gives larger relative abundance than the global minimum structure, despite the smaller interaction energy. With a step-size of 0.001 a.u., the local and global minimum structures are predicted to have effectively the same Gibbs free energy and hence relative abundance. If we were to weight the abundance of each minimum using a Boltzmann distribution, the total abundance would be essentially the same as if we considered the global minimum structure only.

7.7 – Conclusion

We have estimated the abundances of the N_2-N_2O, O_2-N_2O, Ar-N_2O and H_2O-N_2O complexes using the approach of Vaida and Headrick. We find that the concentration of the monomer species that constitute the complex has the greatest effect on the absolute abundance of the complex. This is evident by the N_2-N_2O complex, which uses the largest portion of the atmosphere, N_2, having the largest calculated concentration, whereas the H_2O-N_2O complex is seen to have the smallest calculated concentrations at all altitudes. This is despite our calculations showing that the H_2O-N_2O has the largest binding energy of the complexes studied here, as well as having having either the largest or second largest equilibrium constant depending on altitude.

When we consider the sum of the four complexes compared with the amount of monomer as a function of altitude, we see that there is roughly 1 complex for approximately 300 N_2O monomer molecules. The N_2O monomer will be the limiting species in the formation of the complexes, and this total concentration of the complexes will be dominated by the N_2-N_2O complex which has the largest complex concentration as previously indicated.

7.8 Future research

This work has calculated the abundances of the N_2-N_2O, O_2-N_2O, Ar-N_2O and H_2O-N_2O complexes as a function of altitude in Earth's atmosphers. To determine the effect that complexation has on the N_2O photodissociation rate, the electronic absorption spectra of each complex must also be calculated or preferably measured experimentally. For a particular complex to be atmospherically important it must have both an appreciable abundance in the atmosphere and cause and significant change in the electronic absorption spectrum.

Further research on the local and global minimum structures of O_2-N_2O needs to be obtained, in particular how this impacts on the final calculated abundance. The low frequency modes of the four complexes shows the greatest effect on the statistical thermodynamic parameters of all of the parts of our investigation. Because of this, further work on estimating the sensitivity of the resulting thermodynamic paramters should be undertaken. A complete investigation of the global minimum O_2-N_2O structure needs to be completed with the cc-pVQZ-F12 basis set to ensure the best comparison between the results of all of our investigated complexes.

Further investigations should also be completed using the aug-cc-pV(x+d)Z basis set for the Ar-N_2O complex. This basis set contains additional tight d basis functions compared to the aug-cc-pVxZ basis set that are thought to improve the description of second row elements like Ar.

References

1. Kroeze, C. Nitrous oxide and global warming. *Sci. Total Environ.* **143,** 193–209 (1994).

2. Prinn, R. *et al.* Atmospheric emissions and trends of nitrous oxide deduced from 10 years of ALE–GAGE data. *J. Geophys. Res.* **95,** 18369 (1990).

3. Rasmussen, R. A. & Khalil, M. A. K. Atmospheric Trace Gases: Trends and Distributions Over the Last Decade. *Science* **232,** 1623–1624 (1986).

4. Khalil, M. A. K. & Rasmussen, R. A. Climate-induced feedbacks for the global cycles of methane and nitrous oxide. *Tellus B* **41B,** 554–559 (1989).

5. Van Aardenne, J. *Atmospheric greenhouse gas concentrations (CSI 013/CLIM 052) - Assessment published Feb 2015*. (NOAA, 2015). at <http://www.eea.europa.eu/data-and-maps/indicators/atmospheric-greenhouse-gas-concentrations-4/assessment>

6. Intergovernmental Panel on Climate Change & Intergovernmental Panel on Climate Change. *Climate change 2007: The physical science basis: contribution of Working Group I to the Fourth Assessment Report of the Intergovernmental Panel on Climate Change*. (Cambridge University Press, 2007).

7. Wuebbles, D. J. Chlorocarbon emission scenarios: Potential impact on stratospheric ozone. *J. Geophys. Res.* **88,** 1433 (1983).

8. Schilt, A., Baumgartner. M., Schwander. *J.*,Buiron. D., Capron. E., Chappellaz. J., Loulergue. L., Schüpbach. S., Spahni. R., Fischer. H., Stocker. T. Atmospheric nitrous oxide during the last 140,000 years. *Earth Planet. Sci. Lett.* **300,** 33–43 (2010).

9. Trogler, W. C. Physical properties and mechanisms of formation of nitrous oxide. *Coord. Chem. Rev.* **187,** 303–327 (1999).

10. Cicerone, R. J. Analysis of sources and sinks of atmospheric nitrous oxide (N_2O). *J. Geophys. Res.* **94,** 18265 (1989).

11. *Denitrification, nitrification, and atmospheric nitrous oxide*. (Wiley, 1981).

12. Law, C. S., Rees, A. P. & Owens, N. J. P. Nitrous oxide: Estuarine sources and atmospheric flux. *Estuar. Coast. Shelf Sci.* **35,** 301–314 (1992).

13. Vankessel, C., Pennock, D. . & Farrell, R. . Seasonal variations in denitrification and nitrous oxide evolution at the landscape scale. *Soil Sci. Soc. Am. J.* **57,** 988–995 (1993).

14. Badr, O. & Probert, S. D. Sources of atmospheric nitrous oxide. *Appl. Energy* **42,** 129–176 (1992).

15. Averill, B. A. Dissimilatory Nitrite and Nitric Oxide Reductases. *Chem. Rev.* **96,** 2951–2964 (1996).

16. Finlayson-Pitts, B. J. *Chemistry of the upper and lower atmosphere: theory, experiments, and applications*. (Academic Press, 2000).

17. Hanaike, D. Hawai'i Natural History. (2001). at <http://www2.hawaii.edu/~uhmalama/dhanaike/Cycles_lesson/N_cycle.jpg>

18. Saggar, S., Tate, K. R., Giltrap, D. L. & Singh, J. Soil-atmosphere exchange of nitrous oxide and methane in New Zealand terrestrial ecosystems and their mitigation options: a review. *Plant Soil* **309,** 25–42 (2007).

19. Saggar, S. *et al.* Modelling nitrous oxide emissions from dairy-grazed pastures. *Nutr. Cycl. Agroecosystems* **68,** 243–255 (2004).

20. *Microbial production and consumption of greenhouse gases: methane, nitrogen oxides, and halomethanes*. (American Society for Microbiology, 1991).

21. Jenny, H. A. *The Soil Resource Origin and Behavior*. (Springer New York, 1980). at <http://dx.doi.org/10.1007/978-1-4612-6112-4>

22. Wayne, R. P. *Chemistry of atmospheres: an introduction to the chemistry of the atmospheres of earth, the planets, and their satellites*. (Oxford University Press, 2000).

23. Drake, F. *Global warming: the science of climate change*. (Arnold ; Co-published in the United States of America by Oxford University Press, 2000).

24. Cohen, Y. & Gordon, L. I. Nitrous oxide production in the Ocean. *J. Geophys. Res.* **84,** 347 (1979).

25. Hahn, J. in *Denitrification and Atmospheric Nitrous Oxide* 191–240 (Wiley-Interscience, 1981).

26. Jensen, H. B., Jorgensen, K. S. & Sorensen, J. Diurnal variation of nitrogen cycling in coastal, marine sediments: II. Nitrous oxide emission. *Mar. Biol.* **83,** 177–183 (1984).

27. Sørensen, J. Occurrence of nitric and nitrous oxides in a coastal marine sediment. *Appl. Environ. Microbiol.* **36,** 809–813 (1978).

28. Smith, K. The potential for feedback effects induced by global warming on emissions of nitrous oxide by soils. *Glob. Change Biol.* **3,** 327–338 (1997).

29. Laine, J. *et al.* Effect of water-level drawdown on global climatic warming: Northern peatlands. *R. Swed. ACAD Sci.* **25,** 179–184 (1996).

30. Potter, C. S., Matson, P. A., Vitousek, P. M. & Davidson, E. A. Process modeling of controls on nitrogen trace gas emissions from soils worldwide. *J. Geophys. Res.* **101,** 1361 (1996).

31. Volk, C. M. *et al.* Evaluation of source gas lifetimes from stratospheric observations. *J. Geophys. Res.* **102,** 25543 (1997).

32. Minschwaner, K., Carver, R. W., Briegleb, B. P. & Roche, A. E. Infrared radiative forcing and atmospheric lifetimes of trace species based on observations from UARS. *J. Geophys. Res.* **103,** 23243 (1998).

33. Doering, J. P. & Mahan, B. H. Photoionization of Nitric Oxide. *J. Chem. Phys.* **36,** 669 (1962).

34. McEwan, M. J. *Chemistry of the atmosphere*. (Edward Arnold, 1975).

35. Anderson, G., Clough, S., Kneizys, F., Chetwynd, J. & Shettle, E. *AFGL Atmospheric Constituent Profiles (0-120km)*. (AIR FORCE GEOPHYSICS LABORATORY, 1987).

36. Cheong, N. *et al.* Photodissociation of Nitrous Oxide by Slice Ion Imaging: The Stagnation Pressure Dependence. *Bull. KOREAN Chem. Soc.* **30,** 2661–2664 (2009).

37. Nicolet, M. & Peeterma, W. Production of nitric-oxide in stratosphere by oxidation of nitrous-oxide. *Ann. Geophys.* **28,** 751–761 (1972).

38. Hanisco, T. F. & Kummel, A. C. State-resolved photodissociation of nitrous oxide. *J. Phys. Chem.* **97,** 7242–7246 (1993).

39. Schinke, R. Photodissociation of N_2O: Temperature dependence. *Chem. Phys.* **399,** 142–145 (2012).

40. Selwyn, G. S. Ultraviolet absorption spectrum of nitrous oxide as a function of temperature and isotopic substitution. *J. Chem. Phys.* **74,** 3791 (1981).

41. Holliday, M. G. & Reuben, B. G. Temperature dependence of the absorption of nitrous oxide in the quartz ultra-violet. *Trans. Faraday Soc.* **64,** 1735 (1968).

42. Selwyn, G., Podolske, J. & Johnston, H. S. Nitrous oxide ultraviolet absorption spectrum at stratospheric temperatures. *Geophys. Res. Lett.* **4,** 427–430 (1977).

43. Merienne, M. F., Coquart, B. & Jenouvrier, A. Temperature effect on the ultraviolet absorption of $CFCl_3$, CF_2Cl_2 and N_2O. *Planet. Space Sci.* **38,** 617–625 (1990).

44. Rontu Carlon, N. *et al.* UV absorption cross sections of nitrous oxide (N_2O) and carbon tetrachloride (CCl_4) between 210 and 350 K and the atmospheric implications. *Atmospheric Chem. Phys.* **10,** 6137–6149 (2010).

45. Kawamata, H., Kohguchi, H., Nishide, T. & Suzuki, T. Photodissociation of nitrous oxide starting from excited bending levels. *J. Chem. Phys.* **125,** 133312 (2006).

46. Janssen, M. H., Teule, J., Neyer, D. ., Chandler, D. . & Groenenboom, G. *Atomic and Molecular Beams The State of the Art 2000* (Springer, 2000).

47. Teule, J. M., Groenenboom, G. C., Neyer, D. W., Chandler, D. W. & Janssen, M. H. M. State-to-state photodynamics of nitrous oxide and the effect of long-range interaction on the alignment of $O(^1D)$. *Chem. Phys. Lett.* **320,** 177–185 (2000).

48. Demore, W. B. *et al.* Tables of rate constants extracted fromchemical kinetics and photochemical data for use in stratospheric modeling. Evaluation number 7. *Int. J. Chem. Kinet.* **17,** 1135–1151 (1985).

49. Sturman, A. P. *The weather and climate of Australia and New Zealand*. (Oxford University Press, 2006).

50. Parson, E. A. *Protecting the ozone layer: science and strategy*. (Oxford Univ. Press, 2003).

51. Chapman, S. A theory of Atmospheric Ozone. *Memo. R. Meteorol. Soc.* **3,** 103–125 (1930).

52. Ravishankara, A. R., Daniel, J. S. & Portmann, R. W. Nitrous Oxide (N_2O): The Dominant Ozone-Depleting Substance Emitted in the 21st Century. *Science* **326,** 123–125 (2009).

53. Valsala, V., Alsibai, H. M., Ikeda, M. & Maksyutov, S. Interannual variability of CFC-11 absorption by the ocean: an offline model study. *Clim. Dyn.* **36,** 1435–1452 (2011).

54. Vaida, V. & Headrick, J. E. Physicochemical Properties of Hydrated Complexes in the Earth's Atmosphere. *J. Phys. Chem. A* **104,** 5401–5412 (2000).

55. *Molecular complexes in earth's planetary, cometary, and interstellar atmospheres*. (World Scientific, 1998).

56. Slanina, Z., Uhlík, F., Saito, A. . & Ōsawa, E. Computing molecular complexes in earth's and other atmospheres. *Phys. Chem. Earth Part C Sol. Terr. Planet. Sci.* **26,** 505–511 (2001).

57. McMahon, J. D. & Lane, J. R. Explicit correlation and basis set superposition error: The structure and energy of carbon dioxide dimer. *J. Chem. Phys.* **135,** 154309 (2011).

58. Lane, J. R. CCSDTQ Optimized Geometry of Water Dimer. *J. Chem. Theory Comput.* **9,** 316–323 (2013).

59. Schwenke, D. W. The extrapolation of one-electron basis sets in electronic structure calculations: How it should work and how it can be made to work. *J. Chem. Phys.* **122,** 014107 (2005).

60. Jurečka, P. & Hobza, P. True Stabilization Energies for the Optimal Planar Hydrogen-Bonded and Stacked Structures of Guanine···Cytosine, Adenine···Thymine, and Their 9- and 1-Methyl Derivatives: Complete Basis Set Calculations at the MP2 and CCSD(T) Levels and Comparison with Experiment. *J. Am. Chem. Soc.* **125,** 15608–15613 (2003).

61. Inada, Y. & Orita, H. Efficiency of numerical basis sets for predicting the binding energies of hydrogen bonded complexes: Evidence of small basis set superposition error compared to Gaussian basis sets. *J. Comput. Chem.* **29,** 225–232 (2008).

62. Boys, S. F. & Bernardi, F. The calculation of small molecular interactions by the differences of separate total energies. Some procedures with reduced errors. *Mol. Phys.* **19,** 553–566 (1970).

63. Johansson, A., Kollman, P. & Rothenberg, S. An application of the functional Boys-Bernardi counterpoise method to molecular potential surfaces. *Theor. Chim. Acta* **29,** 167–172 (1973).

64. Werner, H., Knowles, P. Manby, F. . & Schutz, M. *MOLPRO.2010.* (2010).

65. Gimmler, G. & Havenith, M. High-Resolution IR Spectroscopy of the N_2O–H_2O and N_2O–D_2O van der Waals Complexes. *J. Mol. Spectrosc.* **216,** 315–321 (2002).

66. Sadlej, J. & Sicinski, M. Investigations of the anesthetic activity of nitrous-oxide by quantum-chemical calculations. *Theochem-J. Mol. Struct.* **63,** 1–14 (1990).

67. Lane, J. R. & Kjaergaard, H. G. Explicitly correlated intermolecular distances and interaction energies of hydrogen bonded complexes. *J. Chem. Phys.* **131,** 034307 (2009).

68. Hu, T. A., Chappell, E. L. & Sharpe, S. W. Infrared, diode laser spectroscopy of the Ar–N_2O complex: Observation of the intermolecular bending mode in combination with the highest frequency intramolecular stretching mode. *J. Chem. Phys.* **98,** 6162 (1993).

69. Gimmler, G. & Havenith, M. Free-jet infrared diode laser spectroscopy of the v_2-band of the Ar–N_2O van der Waals complex. *J. Mol. Struct.* **599,** 117–123 (2001).

70. Ngari, M. & Jäger, W. Ground State Average and Partial Substitution Structures of the Ar-N_2O van der Waals Dimer. *J. Mol. Spectrosc.* **192,** 452–454 (1998).

71. Randall, R. W., Dyke, T. R. & Howard, B. J. Infrared spectroscopy of the N_2-N_2O van der Waals complex. *Faraday Discuss. Chem. Soc.* **86,** 21 (1988).

72. Venayagamoorthy, M. & Ford, T. A. Ab initio molecular orbital studies of the vibrational spectra of some van der Waals complexes. Part 1. Complexes of molecular nitrogen with carbon dioxide, nitrous oxide, carbonyl sulphide and carbon disulphide. *J. Mol. Struct.* **565-566,** 399–409 (2001).

73. Zheng, R., Zhu, Y., Li, S., Fang, M. & Duan, C. Rovibrational spectrum and potential energy surface of the N_2–N_2O van der Waals complex. *J. Mol. Spectrosc.* **265,** 102–105 (2011).

74. Sennikov, P. G., Ignatov, S. K. & Schrems, O. Complexes and Clusters of Water Relevant to Atmospheric Chemistry: H_2O Complexes with Oxidants. *ChemPhysChem* **6,** 392–412 (2005).

75. Qian, H.-B., Seccombe, D. & Howard, B. J. Spectroscopy and structure of the open-shell complex O_2–N_2O. *J. Chem. Phys.* **107,** 7658–7666 (1997).

76. Anderson, T. R. & Slotkin, T. A. Maturation of the adrenal medulla--IV. Effects of morphine. *Biochem. Pharmacol.* **24,** 1469–1474 (1975).

77. Vaida, V., Daniel, J. S., Kjaergaard, H. G., Goss, L. M. & Tuck, A. F. Atmospheric absorption of near infrared and visible solar radiation by the hydrogen bonded water dimer. *Q. J. R. Meteorol. Soc.* **127,** 1627–1643 (2001).

78. Morokuma, K. & Muguruma, C. Ab initio Molecular Orbital Study of the Mechanism of the Gas Phase Reaction SO_3 + H_2O: Importance of the Second Water Molecule. *J. Am. Chem. Soc.* **116,** 10316–10317 (1994).

79. *Chemistry: the central science*. (Prentice Hall, 2002).

80. Suzuki, T., Katayanagi, H., Nanbu, S. & Aoyagi, M. Nonadiabatic bending dissociation in 16 valence electron system OCS. *J. Chem. Phys.* **109,** 5778 (1998).

81. McQuarrie, D. A. *Statistical mechanics*. (University Science Books, 2000).

82. Pidwirny, M. in *Fundamentals of Physical Geography (2nd Edition)* (PhysicalGeography.net 2008).

Appendices:

Table A.1: Comparison of the optimized geometrical parameters of the H_2O-N_2O complex obtained with the CCSD(T)-F12a and CCSD(T)-F12b methods

	cc-pVDZ-F12			cc-pVTZ-F12			cc-pVQZ-F12		
	F12a	F12b	Difference	F12a	F12b	Difference	F12a	F12b	Difference
$R_{(H1O2)}$	0.9588	0.9584	-0.0003	0.9585	0.9584	-0.0001	0.9582	0.9581	-0.0001
$R_{(H2O2)}$	0.9596	0.9593	-0.0004	0.9595	0.9593	-0.0002	0.9591	0.9591	-0.0001
$R_{(N1O1)}$	1.1903	1.1895	-0.0008	1.1893	1.1890	-0.0003	1.1888	1.1887	-0.0001
$R_{(N1N2)}$	1.1270	1.1266	-0.0003	1.1261	1.1259	-0.0001	1.1255	1.1255	0.0000
$A_{(H1O2H2)}$	104.91	104.89	-0.02	104.99	104.99	0.00	105.05	105.04	0.00
$R_{(N1O2)}$	2.8514	2.8578	0.0064	2.8498	2.8518	0.0020	2.8494	2.8503	0.0009
$A_{(N2N1O2)}$	100.20	100.24	0.05	100.61	100.66	0.04	100.69	100.73	0.04
$A_{(H1O2N1)}$	168.20	167.94	-0.26	169.95	169.98	0.03	170.04	170.19	0.15
$A_{(O1N1O2)}$	80.18	80.15	-0.03	79.79	79.76	-0.04	79.73	79.69	-0.04

Table A.2: Comparison of the optimized geometrical parameters of the Ar-N_2O complex obtained with the CCSD(T)-F12a and CCSD(T)-F12b methods

	cc-pVDZ-F12			cc-pVTZ-F12			cc-pVQZ-F12		
	F12a	F12b	Difference	F12a	F12b	Difference	F12a	F12b	Difference
$R_{(O1N1)}$	1.1881	1.1875	-0.0006	1.1870	1.1867	-0.0003	1.1864	1.1863	-0.0001
$R_{(N1N2)}$	1.1291	1.1285	-0.0006	1.1282	1.1281	-0.0001	1.1277	1.1277	-0.0000
$R_{(N1Ar)}$	3.3817	3.4024	+0.0207	3.3917	3.3976	+0.0059	3.3935	3.3950	0.0015
$A_{(N2N1Ar)}$	94.03	94.08	+0.05	93.77	93.84	+0.07	93.69	93.71	0.02
$A_{(O1N1Ar)}$	85.79	85.76	-0.03	86.07	86.01	-0.06	86.16	86.15	0.01

Table A.3: Comparison of the optimized geometrical parameters of the N_2-N_2O complex obtained with the CCSD(T)-F12a and CCSD(T)-F12b methods

	cc-pVDZ-F12			cc-pVTZ-F12			cc-pVQZ-F12		
	F12a	F12b	Difference	F12a	F12b	Difference	F12a	F12b	Difference
$R_{(O1N1)}$	1.1882	1.1874	-0.0008	1.1870	1.1867	-0.0003	1.1864	1.1862	-0.0002
$R_{(N1N2)}$	1.1288	1.1284	-0.0004	1.1279	1.1278	-0.0001	1.1274	1.1273	-0.0001
$R_{(N3N4)}$	1.1002	1.0997	-0.0005	1.0994	1.0992	-0.0002	1.0989	1.0988	-0.0001
$R_{(N1N3)}$	3.1203	3.1317	+0.0114	3.1147	3.1178	+0.0031	3.1104	3.1110	+0.0006
$A_{(N2N1N3)}$	95.73	95.67	-0.06	95.61	95.61	0.00	95.43	95.43	0.00
$A_{(O1N1N3)}$	84.16	84.24	+0.08	84.30	84.30	0.00	84.47	84.47	0.00
$A_{(N4N3N1)}$	165.46	166.10	+0.64	166.15	166.33	+0.18	167.20	167.26	+0.06

Table A.4: Comparison of the optimized geometrical parameters of the global minimum O_2-N_2O complex obtained with the UCCSD(T)-F12a and UCCSD(T)-F12b methods

	cc-pVDZ-F12			cc-pVTZ-F12			cc-pVQZ-F12		
	F12a	F12b	Difference	F12a	F12b	Difference	F12a	F12b	Difference
$R_{(N2N1)}$	1.1289	1.1286	-0.0003	1.1281	1.1280	-0.0001	1.1275	1.1275	0.0000
$R_{(O1N1)}$	1.1884	1.1876	-0.0008	1.1873	1.1869	-0.0004	1.1867	1.1865	-0.0002
$R_{(O2O3)}$	1.2082	1.2077	-0.0005	1.2070	1.2068	-0.0002	1.2063	1.2062	-0.0001
$R_{(O2N1)}$	3.0607	3.0740	+0.0133	3.0627	3.0658	+0.0031	3.0591	3.0601	+0.0010
$A_{(O1N1O2)}$	84.20	84.08	-0.12	84.61	84.57	-0.04	84.59	84.58	-0.01
$A_{2(N2N1O2)}$	95.61	95.75	+0.14	95.22	95.28	+0.06	95.25	95.27	+0.02
$A_{(O3O2N1)}$	111.87	112.54	+0.67	113.04	113.21	+0.17	114.20	114.26	+0.06

Table A.5: The UCCSD(T)-F12b optimised geometrical parameters of the local minimum O_2-N_2O complex obtained with and without counterpoise correction

	UCCSD(T)-F12b					
	cc-pVDZ-F12			cc-pVTZ-F12		
	Standard	Counterpoise	Difference	Standard	Counterpoise	Difference
$R_{(N1O2)}$	3.0738	3.1003	0.0266	3.0652	3.0802	0.0150
$R_{(N1N2)}$	1.1288	1.1288	0.0000	1.1282	1.1282	0.0000
$R_{(N1O1)}$	1.1871	1.1871	0.0000	1.1864	1.1864	0.0000
$R_{(O2O3)}$	1.2079	1.2078	-0.0001	1.2070	1.2070	0.0000
$A_{(N2N1O2)}$	92.93	93.08	0.15	92.86	92.99	0.13
$A_{(N1\text{-}O2O3)}$	116.75	117.39	0.64	117.34	118.59	1.25
$A_{(N2N1O1)}$	179.83	179.86	0.03	179.85	179.86	0.01
	UCCSD(T)					
	aug-cc-pVDZ			aug-cc-pVTZ		
	Standard	Counterpoise	Difference	Standard	Counterpoise	Difference
$R_{(N1O2)}$	3.0185	3.0600	0.0415	3.0516	3.0743	0.0227
$R_{(N1N2)}$	1.1283	1.1282	-0.0001	1.1282	1.1282	0.0000
$R_{(N1O1)}$	1.1856	1.1857	0.0000	1.1861	1.1862	0.0000
$R_{(O2O3)}$	1.2071	1.2068	-0.0003	1.2069	1.2069	-0.0001
$A_{(N2N1O2)}$	92.92	92.80	-0.12	92.61	92.89	0.28
$A_{(N1\text{-}O2O3)}$	109.86	116.39	6.53	115.58	117.55	1.97
$A_{(N2N1O1)}$	179.78	179.83	0.05	179.85	179.86	0.01

Table A.6: Equilibrium constants at standard pressure for H_2O-N_2O, Ar-N_2O, N_2-N_2O and O_2-N_2O, raw data for Figure 7.6

	H_2O-N_2O	Ar-N_2O	N_2-N_2O	O_2-N_2O
0	0.0025	0.0044	0.0030	0.0030
5	0.0037	0.0049	0.0033	0.0030
10	0.0062	0.0057	0.0037	0.0031
15	0.0070	0.0059	0.0038	0.0032
20	0.0070	0.0059	0.0038	0.0032
25	0.0064	0.0058	0.0037	0.0031
30	0.0058	0.0056	0.0036	0.0031
35	0.0049	0.0054	0.0035	0.0031
40	0.0040	0.0050	0.0033	0.0030
45	0.0033	0.0048	0.0032	0.0030
50	0.0031	0.0047	0.0031	0.0030

Table A.7: Calculated enthalpy values (kJ) for H_2O-N_2O, Ar-N_2O, N_2-N_2O and O_2-N_2O, raw data for Figure 7.3

Altitude (km)	H_2O-N_2O	Ar-N_2O	N_2-N_2O	O_2-N_2O
0	-7.13	-2.21	-1.28	-0.12
5	-7.31	-2.21	-1.54	-0.38
10	-7.64	-2.20	-1.79	-0.64
15	-7.70	-2.20	-1.84	-0.69
20	-7.70	-2.20	-1.84	-0.69
25	-7.65	-2.20	-1.80	-0.65
30	-7.60	-2.20	-1.76	-0.61
35	-7.51	-2.21	-1.68	-0.53
40	-7.36	-2.21	-1.58	-0.42
45	-7.22	-2.21	-1.47	-0.31
50	-7.15	-2.21	-1.42	-0.26

Table A.8: Calculated TΔS values (J/K) for H_2O-N_2O, Ar-N_2O, N_2-N_2O and O_2-N_2O, raw data for Figure 7.4

Altitude (km)	H_2O-N_2O	Ar-N_2O	N_2-N_2O	O_2-N_2O
0	-20.32	-14.43	-15.18	-14.06
5	-19.20	-13.51	-13.71	-12.72
10	-17.06	-11.78	-12.20	-11.34
15	-16.63	-11.44	-11.90	-11.06
20	-16.63	-11.44	-11.90	-11.06
25	-16.96	-11.70	-12.13	-11.27
30	-17.29	-11.96	-12.36	-11.49
35	-17.95	-12.49	-12.83	-11.91
40	-18.86	-13.2	-13.47	-12.50
45	-19.77	-13.97	-14.11	-13.09
50	-20.16	-14.30	-14.39	-13.34

Table A.9: Calculated Gibbs free energy values (kJ/mol) for H_2O-N_2O, Ar-N_2O, N_2-N_2O and O_2-N_2O, raw data for Figure 7.5

Altitude (km)	H_2O-N_2O	Ar-N_2O	N_2-N_2O	O_2-N_2O
0	14.31	13.01	13.90	13.94
5	11.89	11.29	12.17	12.34
10	9.43	9.58	10.41	10.70
15	8.93	9.23	10.06	10.37
20	8.93	9.23	10.06	10.37
25	9.30	9.49	10.33	10.62
30	9.69	9.76	10.60	10.88
35	10.44	10.28	11.14	11.38
40	11.50	11.02	11.90	12.08
45	12.55	11.76	12.65	12.78
50	13.01	12.09	12.97	13.08

Table A.10: Abundance[6] of monomer species with altitude (ppmv) , raw data for Figure 7.7

Altitude (km)	H_2O	N_2O	O_2	N_2	Ar
0	7.75E+03	3.20E-01	2.09E+05	7.81E+05	9.30E+03
5	1.40E+03	3.20E-01	2.09E+05	7.81E+05	9.30E+03
10	7.00E+01	3.18E-01	2.09E+05	7.81E+05	9.30E+03
15	5.00E+00	2.94E-01	2.09E+05	7.81E+05	9.30E+03
20	3.90E+00	2.37E-01	2.09E+05	7.81E+05	9.30E+03
25	4.43E+00	1.76E-01	2.09E+05	7.81E+05	9.30E+03
30	4.73E+00	1.42E-01	2.09E+05	7.81E+05	9.30E+03
35	4.90E+00	9.28E-02	2.09E+05	7.81E+05	9.30E+03
40	5.03E+00	4.51E-02	2.09E+05	7.81E+05	9.30E+03
45	5.23E+00	1.59E-02	2.09E+05	7.81E+05	9.30E+03
50	5.23E+00	4.75E-03	2.09E+05	7.81E+05	9.30E+03

[6] Values for H2O, N2O, O2 and N2 are from Anderson *et al*[76], (ref here???) whereas the values for Ar are from Pidwirny[82]

Table A.11: Calculated abundances (atm) for H_2O-N_2O, Ar-N_2O, N_2-N_2O and O_2-N_2O, raw data for Figure 7.7

Altitude (km)	H_2O-N_2O	Ar-N_2O	N_2-N_2O	O_2-N_2O
0	6.32E-12	1.30E-11	7.55E-10	1.99E-10
5	1.67E-12	1.47E-11	8.14E-10	2.01E-10
10	1.38E-13	1.69E-11	9.07E-10	2.07E-10
15	1.03E-14	1.62E-11	8.63E-10	1.94E-10
20	6.50E-15	1.31E-11	6.96E-10	1.56E-10
25	4.99E-15	9.46E-12	5.05E-10	1.15E-10
30	3.93E-15	7.43E-12	3.99E-10	9.22E-11
35	2.25E-15	4.62E-12	2.51E-10	5.95E-11
40	9.07E-16	2.11E-12	1.16E-10	2.85E-11
45	2.76E-16	7.04E-13	3.95E-11	9.96E-12
50	7.66E-17	2.05E-13	1.16E-11	2.97E-12

Table A.12: Calculated statistical parameters for the O_2-N_2O complex at the 50 km altitude, using different step-sizes for the numerical Hessian

	step size = 0.003		step size = 0.001	
	Global minimum	Local minimum	Global minimum	Local minimum
Enthalpy ($kJmol^{-1}$)	3.07	3.03	3.26	3.04
Entropy ($T\Delta S$) ($kJ\ mol^{-1}$)	-13.87	-12.59	-14.57	-14.36
Interaction energy ($kJ\ mol^{-1}$)	-3.38	-3.03	-3.38	-3.03
Gibbs free energy ($kJ\ mol^{-1}$)	13.56	12.59	14.44	14.38
Kp	2.42E-03	3.71E-03	1.63E-03	1.68E-03
Abundance (Atm)	2.40E-12	3.69E-12	1.62E-12	1.67E-12